Remote Sensing Information for Urban Planning of Satkhira Town and Surroundings

Hannover, July 2021

BGR Bundesanstalt für Geowissenschaften und Rohstoffe

german cooperation
DEUTSCHE ZUSAMMENARBEIT

Authors:	Lukas Wimmer (BGR), Chapter 2.1-2.3 Nicolas Wagener (BGR), Chapter 1, Chapter 2.4

Commissioned by:	Federal Ministry for Economic Cooperation and Development (Bundesministerium für wirtschaftliche Zusammenarbeit und Entwicklung, BMZ)
Project:	Geo-Information for Urban Planning and Adaptation to Climate Change (GPAC)
Project Number:	2016.2062.4
BGR Number:	05-2394
ELVIS Number:	B80136-01_06 05-2394 TZ Bangladesch-III
Project Partner:	Geological Survey of Bangladesh (GSB)

Pages:	103
Place and date of issuance:	Hannover, 13. July 2021

To be cited as:

Wimmer, L. and Wagener, N. (2021): Remote Sensing Information for Urban Planning of Satkhira Town and Surroundings, BGR Project Number: 05-2394.

Summary

Authors: Lukas Wimmer, Nicolas Wagener

Title: *Remote Sensing Information for Urban Planning of Satkhira Town and Surroundings*

Keywords: Land-Use Classification; River Change Detection; Inundation Mapping; Interferometric Synthetic Aperture Radar (InSAR); Ground Motion

The products of this report aim to provide support for urban planning for the city of Satkhira and its surrounding areas. Based on optical and radar satellite data, maps on recent land use and urban development, river course changes, rainy season inundation and ground motion are created.

Land-use in the Satkhira study area is characterized by a relatively small urban area surrounded by large agricultural areas and polders that are seasonally inundated or waterlogged throughout the year. Significant anthropogenic overprints of former river parts by agricultural land-use are identified using the river shifting change detection in the surroundings of Satkhira. Frequent inundation is showing up in the polder areas around Satkhira; the city centre does not experience seasonal inundation.

Ground motion maps are created using two different multi-temporal Interferometric SAR (InSAR) approaches, Persistent Scatterer Interferometry (PSI) and Small Baseline Subset (SBAS) and two different types of SAR data: medium-resolution Sentinel-1 data and high-resolution TerraSAR-X data. In total, three different InSAR datasets (two PSI and one SBAS) are created.

There are great differences in the spatial coverage of the three datasets. The Sentinel-1 based SBAS dataset and the TerraSAR-X based PSI dataset achieve a significantly higher spatial coverage than the Sentinel-1 based PSI dataset. Nonetheless, the results are mostly coherent with each other and reveal that most of the city centre can be considered stable or moving only slightly over the observation period. Points of strong subsidence are mostly found on or around newly built structures and are likely related to the building load of these structures.

Table of Contents

List of Figures

Annexure A

List of Tables

List of Abbreviations

ASF	Alaska Satellite Facility
BBD	Bodenbewegungsdienst Deutschland (German Ground Motion Service)
BGR	Bundesanstalt für Geowissenschaften und Rohstoffe (Federal Institute for Geosciences and Natural Resources)
BWDB	Bangladesh Water Development Board
dB	Decibel (unit)
DEM	Digital Elevation Model
DOS	Dark Object Subtraction
ESA	European Space Agency
GNSS	Global Navigation Satellite System
GPAC	Geo-Information for Urban Planning and Adaptation to Climate Change
GPS	Global Positioning System
GSB	Geological Survey of Bangladesh
InSAR	Interferometric Synthetic Aperture Radar
Landsat MSS	Landsat Multispectral Scanner System
Landsat OLI	Landsat Operational Land Imager
Landsat TM	Landsat Thematic Mapper
LEDAPS	Landsat Ecosystem Disturbance Adaptive Processing System
NASA	National Aeronautics and Space Administration
NIR	Near Infrared
NDWI	Normalized Difference Water Index
PSI	Persistent Scatterer Interferometry
RADAR	Radio Detection and Ranging
SAR	Synthetic Aperture Radar
SBAS	Small Baseline Subset
SRTM	Shuttle Radar Topography Mission
SWIR	Shortwave Infrared
TIR	Thermal Infrared
UAV	Unmanned aerial vehicle
USGS	United States Geological Survey

1 Introduction to Remote Sensing

Remote sensing has been variously defined, but basically is the science that describes the collection of physical information, interpretation and extraction 3f information acquired over an object or area of interest without having physical contact, by the use of remote sensing instruments. The term information refers to a wide range of observable quantities, such as reflected solar radiation across the electromagnetic spectrum and emitted thermal radiation measured from handheld, unmanned aerial vehicle (UAV), airborne or spaceborne imaging sensors and received back-scattered microwave radiation equipment. Availability and effective exploitation of such data has facilitated advances in many applied fields (CHAMBELL, 1996; USTIN, 2004)

The availability and capacity of remote sensing data is comprehensive and huge, therefore the application of remote sensing data to identify and monitor land surfaces and environmental conditions has expanded enormously and remotely sensed data are an essential tool in natural resource management. Climatic changes, desertification processes, forest fires, glaciers melting, water pollution, land cover and vegetation status can be observed thanks to remote sensors onboard of aircraft or satellites orbiting around the earth. Remote sensors onboard of aircraft and satellites allow for a synoptic view of the earth surface at different wavelengths of the electromagnetic radiation at the same time (multi-spectral, -frequency), with (high-) frequent time interval and scale (multi-resolution).

Sensors can be divided into two groups: Passive sensors depend on an external source of energy, usually the sun. Sun radiation is reflected and emitted from the earth surface and collected by a wide variety of optical sensors. Active sensors have their own source of energy. These sensors send out a signal and measure the amount reflected back, and do not depend upon varying illumination conditions (PRASAD ET AL., 2011) (see Fig. 1).

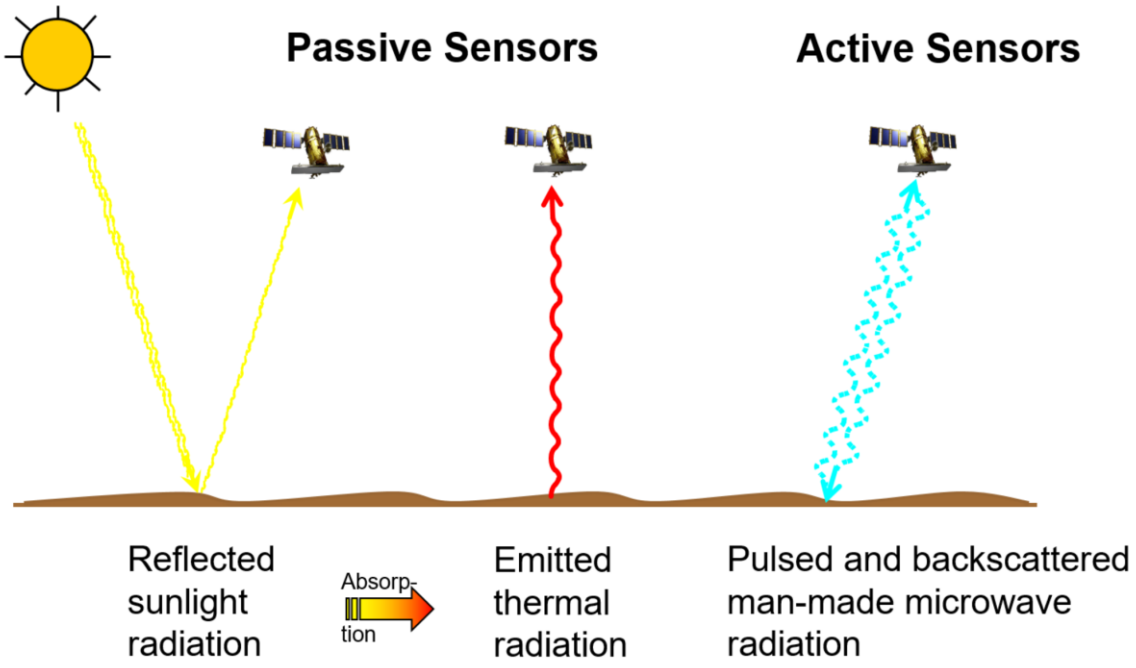

Figure 1: *Passive and active sensors (Source: BGR).*

1.1 Fundamentals of Optical Remote Sensing

Optical remote sensing involves acquisition and analysis of optical data, based on solar illumination and the detection of electromagnetic radiation reflected from targets on the ground. Optical Remote Sensing deals with those part of electromagnetic spectrum characterized by the wavelengths from the visible (from 0.4 µm) to the near infrared (NIR) and short wave infrared (SWIR) up to thermal infrared (TIR, 15 µm), collecting radiation reflected and emitted from the observed surfaces (see Fig. 1).

Optical remote sensing is a passive technique for earth observation, which is exposed to a strong interaction of the electromagnetic radiation within the atmosphere at its operating frequencies and to the presence of clouds. Both factors constitute important limitations on the potential observation of the earth's surface.

Analysis is based on the spectral differences of materials, as materials reflect and absorb differently at different wavelengths, resulting in a specific and unique "spectral footprint". Thus, the targets can be differentiated by their spectral reflectance signatures in the remotely sensed images (SABINS, 1996; RENCZ, 1999).

Optical remote sensing systems are classified depending mainly on the number of spectral bands used in the imaging process. Advances in imaging hardware enabled availability of high spatial, spectral and temporal resolution (PRASAD ET AL., 2011).

A wide range of applications is still based on multispectral imaging systems e.g. Sentinel-2, Landsat-OLI, even so hyperspectral sensors show rapid development on all platforms from UAV to spaceborne carriers.

1.2 Fundamentals of RADAR Remote Sensing

RADAR is an acronym for *RA*dio *D*etection *A*nd *R*anging and describes an object-detection and active imaging system using radio waves (see Fig. 1). The electromagnetic waves used for imaging radars have wavelengths in the order of several centimeters up to roughly one meter. Since earth's atmosphere has a high penetrability in this part of the electromagnetic spectrum, radar-imaging systems are highly independent from weather conditions in the atmosphere.

The accuracy of an imaging radar is defined by two measures: the resolution along the line-of-sight (range resolution) and the resolution along the flight path of the carrier platform (azimuth resolution). The azimuth resolution depends on the antenna aperture: the larger the distance to the area of interest, the larger the antenna must be. For space-borne missions this leads to unrealistic demands on the size of the antenna mounted on the satellite (WOODHOUSE, 2006). To overcome this obstacle, Synthetic Aperture Radar (SAR) exploits the Doppler Effect to synthesize a larger virtual antenna through the combination of several return signals (echoes).

The signal received at the sensor has a frequency variation induced as a result of the platform motion. This effect is known as Doppler shift, a well-known phenomenon in physics. Since the resolution depends on the time, a particular object on the ground is illuminated by the radar beam, making use of the Doppler shift to combine several backscattered echoes effectively results in increasing the duration of irradiation. As this is in effect equal to increasing the antenna aperture size of which the illumination time is a direct function, the term Synthetic Aperture Radar (SAR) is used to describe such an imaging system (RICHARDS, 2009).

SAR sensors are usually mounted on an airborne or space-borne platform and have a side-looking imaging geometry. While the carrier platform moves forward, the SAR system continuously emits and receives electromagnetic pulses. The emitted radiation interacts with objects on the surface that will then backscatter a portion of the signal to the sensor. How big that portion will be, depends on the physical and electrical properties of the objects (FORNANO & PASCAZIO, 2014). At the sensor, both amplitude and phase of the backscattered signal are received (MOREIRA ET AL., 2013).

While the amplitude is related to the object properties (material, roughness, dielectric properties, etc.), the phase is a function of the sensor-target distance.

Synthetic aperture radar (SAR) remote sensing is used today in a wide range of applications and offers a number of complementary and additional capabilities with regard to optical remote sensing. For instance, it can be used to acquire images at night and almost weather independent, to determine soil moisture, biomass or to measure terrain deformations. The ranging capabilities of SAR are used in various ways. Radar interferometry (InSAR) is one such application and allows the estimation of ground deformation and / or topography from (at least) two SAR acquisitions making use of the phase information contained in both images. Multi-temporal InSAR approaches such as Persistent Scatterer Interferometry (PSI) allow the precise estimation (with millimeter accuracy) of surface deformation for specific point targets over long time periods.

2 Products

2.1 Land-use Map

The fast growing population and the trend to move to urban areas leads to a dynamic change in land use. New urban areas are developed by filling agricultural land with river sand to make the building ground more resilient to flooding (see Fig. 2).

The overall goal of this analysis is the comprehensive mapping of the 2019 land-use in Satkhira to derive information on existing and newly established filled areas. The resulting maps will be used in further analyses together with a geomorphological map as a basis for the regionalization of drilling points. Freely available optical satellite data and a supervised classification method allow for the mapping of the land-use.

Figure 2: *Filling of agricultural land with river sand in Faridpur. Photo: L. Wimmer, 11/2019.*

Land-use maps using the classes “Water”, “Bare Soil”, “Urban”, “Rural Settlements” and “Agriculture” are provided for November 2019. An overview map shows the land-use of the study area as well as the surrounding rural areas (Fig. A2). A map, focusing on the study area presents the land-use within the city of Satkhira (Fig. A3).

The main focus of this analysis is the distribution of filled and non-filled areas from the land-use map by reclassification of the five above-mentioned classes. A third map presents these areas within the study area of Satkhira (Fig. A4).

To process the land-use maps, a supervised classification method based on interactively selected training areas is used. These areas are interactively chosen from the original satellite image and represent the spectral properties of a certain land-use class. The supervised classification classifies the satellite image by comparing all the image values with the selected training areas.

Data

The land use classification is based on a cloud-free image from the Copernicus Sentinel-2 mission for the period of the Bangladesh dry season between October and April and the transition times before and after it. To be able to receive results on the most recent land-use and in order to map water areas comprehensively, a satellite image from the early dry season 2019/2020 is required. Different atmospheric conditions during the sensing times of the images can result in different image features of the same ground objects. Therefore, atmospheric corrected images are mandatory, to allow comparison with future land use maps based on Sentinel-2 data. An atmospheric correction eliminates the atmospheric effects in an image and results in a surface reflectance image that characterizes the spectral surface properties. The atmospherically corrected image, showing the overview area cloud-free, from the 16. November 2019 is used for further processing (see Annexure C: Data).

As input for the land use mapping, all bands with the resolution of 10m and 20m of the image are used (Tab. 1). This selection enables the classification method to accurately characterize the land-use classes by using all available spectral properties of the ground objects.

Table 1: *Overview of the Copernicus Sentinel-2 satellite image used for the classification. Blue color represents the spectral band subset used in the analysis.*

Sensing Date	Bands		Wavelengths	Spatial Resolution
22.09.2019	1	Coastal Aerosol	417nm – 471nm	60m
	2	Blue	399nm – 595nm	10m
	3	Green	515nm – 605 nm	10m
	4	Red	627nm – 703nm	10m
	5	Near Infrared	685nm – 723nm	20m
	6		722nm – 758nm	20m
	7		754nm – 810nm	20m
	8		690nm – 980nm	20m
	8A		832nm – 898nm	20m
	9	Water Vapor	919nm – 971nm	60m
	10	Cirrus	1299nm – 1449nm	60m
	11	Shortwave Infrared	1471nm – 1757nm	20m
	12		1960nm – 2444nm	20m

Methods

The workflow of the classification is visualized in Fig. 3.

Preprocessing

To prepare the image for the classification, a spatial subset and a spectral subset are created. The spatial subset shows an overview of the study area of Satkhira as well as the surrounding rural areas (Fig. A1). The spectral subset includes the above-mentioned (Tab. 1) Sentinel-2 bands (Band 2, 3, 4, 5, 6, 7, 8, 8A, 11, 12). Subsequent, all image bands with 20m resolution are resampled to a 10m spatial resolution to keep the information of the higher resolution 10m bands.

Classes and Training Areas

The purpose of the land-use classification is to derive information on urban settlement structures. Accordingly, the two classes “Urban" and "Rural Settlements" are used for the description of these structures. “Agriculture" and "Bare Soil" are chosen to describe the undeveloped areas in general. Water areas are represented by the class "Water".

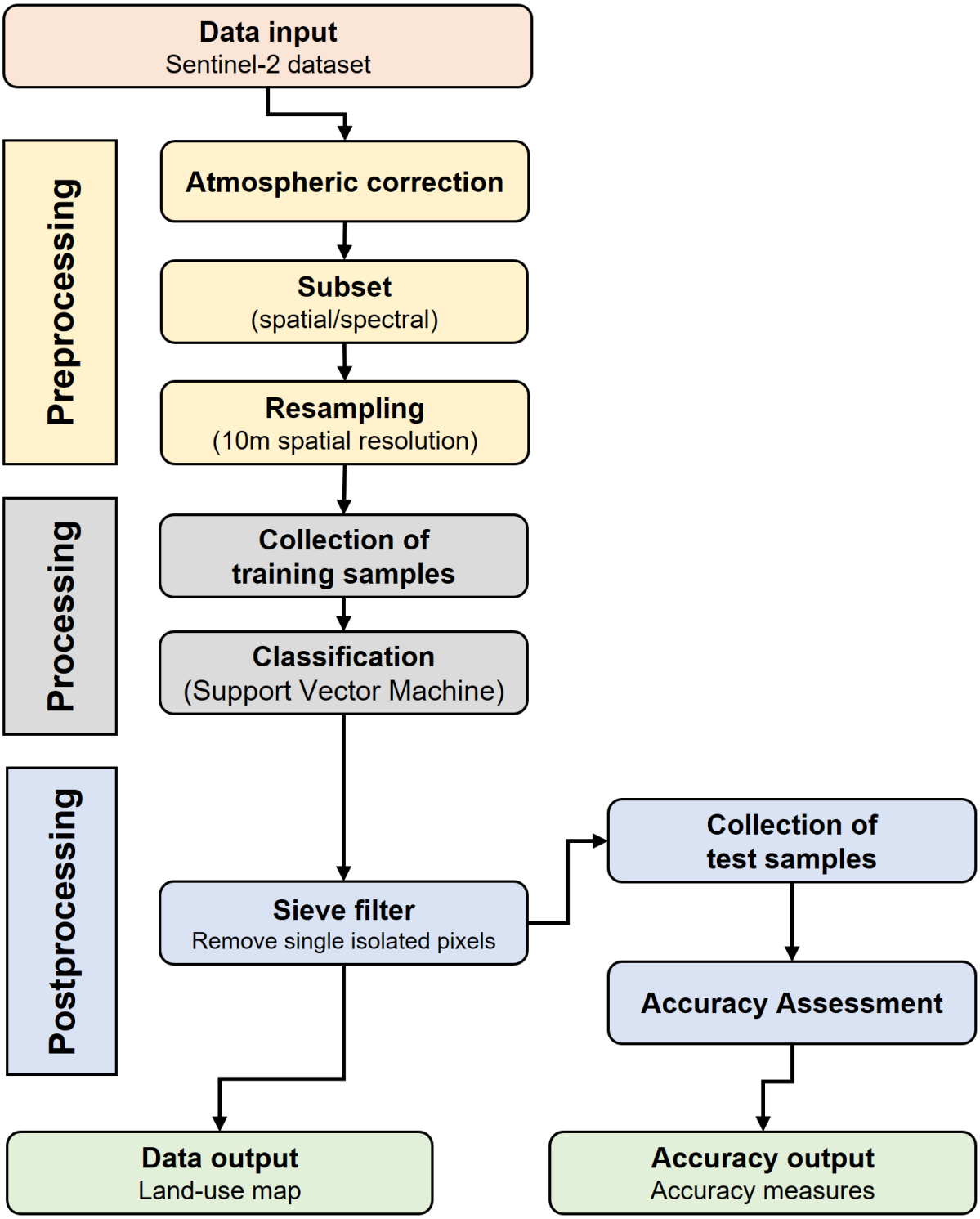

Figure 3: *Workflows of the Land-use classification.*

These classes are based on the CORINE Landcover (CLC) program (EUROPEAN ENVIRONMENT AGENCY, 2019). CORINE Landcover is a program of the European Commission to standardize the most important forms of land cover for environmental policy development. The standardized classes are based on biophysical characteristics of the Earth's surface (EUROPEAN ENVIRONMENT AGENCY, 2017).

"Water" includes all open water bodies, such as river, canals, channels, lakes and ponds. "Bare Soil" includes all surfaces of bright bare soil, such as riverbanks, pointbars and filled areas for urban development. "Urban" includes residential and industrial buildings without tree cover. Furthermore, it includes streets, railway lines and sealed surfaces. "Rural Settlements" include the city suburbs and rural villages that have tree coverage. "Agriculture" are all areas of farmland, such as cropland (rice, vegetables, etc.) or pasture land (for cattle, goats, etc.).

Training areas for all classes are selected from the Sentinel-2 dataset (see Tab. 2). To receive an acceptable classification result, the training areas must be both representative and complete for their land-use classes (LILLESAND ET AL., 2015).

All land-use classes have non-uniform spectral characteristics in common. For example, in the "Urban" class, the spectral characteristics of tin shacks and high-rise buildings differ. The "Agriculture" class includes spectral characteristics of different crops and in the "Water" class, different water qualities also differ spectrally. Different soil types in the "Bare Soil" class also have different spectral characteristics. The "Rural Settlements" class contains areas with different tree species, which result in different spectral characteristics.

The training areas of the land-use classes are required to represent these different spectral characteristics. The number of training areas therefore depends on the spectral variability within a land-use class (see Tab. 2).

The training areas are dispersed throughout the Sentinel-2 dataset to increase the representation of all variations in the land-use classes (LILLESAND ET AL., 2015).

Table 2: *Overview of the number of training areas per class.*

Class	Number of Training Areas
Agriculture	20
Bare Soil	5
Rural Settlements	15
Urban	10
Water	15

To show the spectral variabilities of the individual classes, the spectral profiles of the classes are shown in Fig. 4. Each curve represents the averaged spectral signatures of all training areas per class, based on the Sentinel-2 data set of 14.10.2019. Fig. 4 shows the spectral separability of the classes over the whole band range (see Tab. 1).

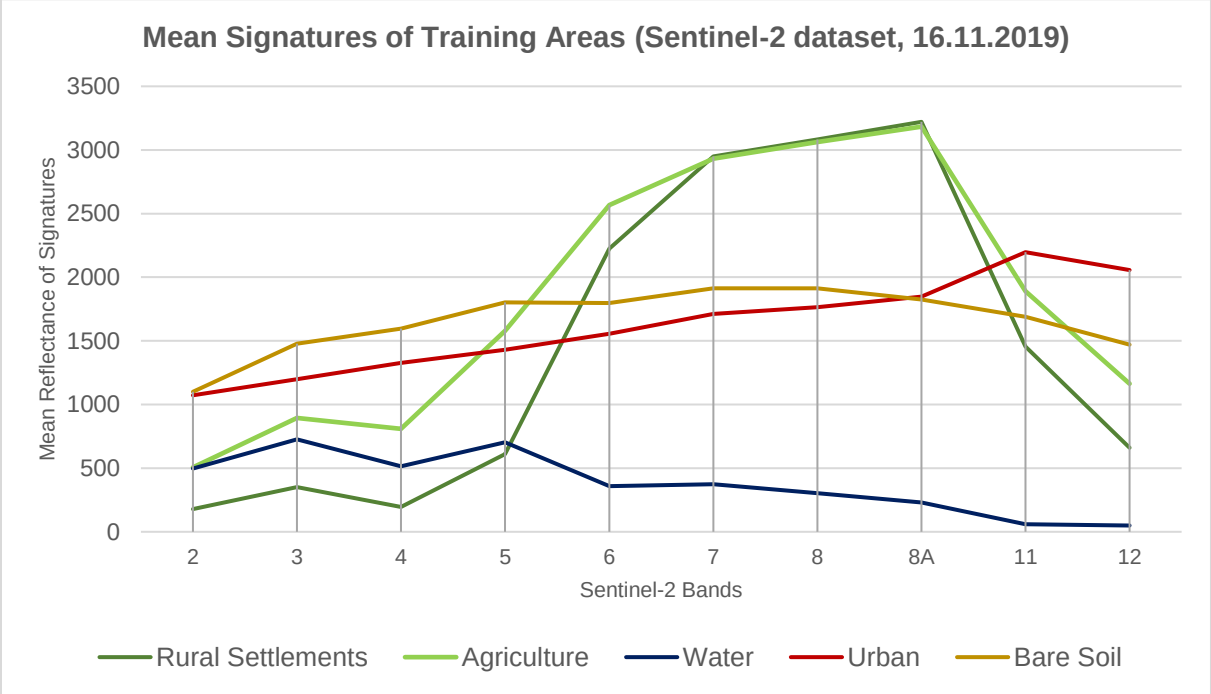

Figure 4: *Mean signatures of the merged training areas.*

The spectral curves of the classes “Agriculture” and “Rural Settlements” have similar spectral signatures. The reason for these similarities is that the class “Rural Settlements” is dominated by tree coverage and therefore represents a strong vegetation signal.

Both classes show vegetation-typical characteristics, such as the "red edge" (a significant increase of reflection in the near infrared bands 5 and 6 compared to the visible bands 2 to 4). The main differences are a higher reflectance of the class “Agriculture” in bands 2 to 6/11 and 12 and a slightly higher reflectance of the class “Rural Settlements” in bands 7 to 8A.

The spectral signature of “Water” shows higher reflection values around band 7 and 8 leading to the interpretation that the water class/signature contains impurities, such as sediments. Pure water would have zero reflectance in these longer wavelengths.

The spectral curve of the class “Urban” shows a relatively continuous increase. The spectral curve can be compared to the signature of “Bare Soil”, as both signatures show corresponding characteristics. The main difference between both signatures is a higher “Urban” reflectance in the shortwave-infrared compared to a lower reflectance of “Bare Soil” in these wavelengths.

Classification

To perform the supervised classification, the Support Vector Machine (SVM) classifier is selected, a method based on statistical learning theory. Support Vector Machines are supervised learning models with associated learning algorithms that analyze data used for classification.

The classifier looks at spectral boundaries between individual classes in the multidimensional feature space. It aims to find an optimal margin (known as “hyperplane”) to separate the classes. The data values that constrain the width of the margin are known as “support vectors” (JONES & VAUGHAN, 2010).

In its simplest form, a SVM separates two classes (a binary classifier). Nevertheless, a classification with multiple classes is possible. Based on the training areas, several binary classifiers are calculated which separate the properties of each class from those of every other class (known as “one-versus-one” approach). The number of binary classifiers depends on the number of classes to be separated:

$$n_{classifier} = \frac{n_{class} * (n_{class} - 1)}{2}$$

The variable $n_{classifier}$ represents the number of classifiers; the variable n_{class} represents the number of classes.

Therefore, the properties of the five classes of this investigation are separated using 10 binary classifiers (Tab. 3 shows an example of possible connections of classes), as a result the classes are differentiated spectrally. Each classifier designates a class name to every pixel, the most frequent class name assigns the pixel to the final class (RICHARDS, 2013).

Table 3: *The table shows all possible connections of classes (cf. RICHARDS, 2013).*

Number of binary classifiers	Class name 1	Class name 2
1	Agriculture	Bare Soil
2	Agriculture	Rural Settlements
3	Agriculture	Urban
4	Agriculture	Water
5	Bare Soil	Rural Settlements
6	Bare Soil	Urban
7	Bare Soil	Water
8	Rural Settlements	Urban
9	Rural Settlements	Water
10	Urban	Water

Post-Processing

The same object feature may be classified in different classes due to spectral variabilities. The classification result might show single isolated pixels of one class in the area of another class (LILLESAND ET AL., 2015).

To remove the single isolated pixels in the classification image, a sieve filter is applied. This filter replaces all pixel patches that are smaller than twelve pixels by the value of the surrounding neighbor class. A pixel patch is a group of pixels that share their sides or have connected angles. The final classification result is shown in Fig. A2 and A3.

Calculation of filled and non-filled areas

Based on the knowledge of the GSB colleagues and the experience gained during fieldwork, all urbanized areas and settlement structures in Satkhira are developed on filled areas. Therefore, those areas are considered as filled areas, the classes “Urban” and “Rural Settlements” are reclassified to “Filled” and the classes “Water”, “Bare Soil” and “Agriculture” are reclassified to “Non-filled” (see Fig. A4).

Accuracy Assessment

During the accuracy assessment, randomly distributed test samples are used to compare the classification result with an independent high-resolution reference dataset. As a high-resolution reference dataset, free accessible Google Earth satellite images are used. Thus, details for a more precise interpretation of the actual land use become visible and the classification result can be assessed visually without having the necessity to collect ground truth information during fieldwork.

LILLESAND ET AL. (2015) recommends using at least 50 test samples per class for accuracy assessment. Following this recommendation, 250 test samples are randomly distributed in the image, using 50 samples for each class (Tab. 4).

Table 4: *Accuracy Assessment, Sentinel-2 dataset (16.11.2019).*

Sentinel-2, 16.11.2019		Reference						
		Agriculture	Bare Soil	Rural Settlements	Urban	Water	Row Total	**User's Accuracy (%)**
Classification	Agriculture	41	0	8	1	0	50	82.0
	Bare Soil	12	34	0	4	0	50	68.0
	Rural Settlements	3	2	39	6	0	50	78.0
	Urban	3	9	8	26	4	50	52.0
	Water	3	0	0	0	47	50	94.0
	Column Total	62	45	55	37	51	250	
	Producer's Accuracy (%)	66.1	75.5	70.9	70.2	92.1		
	Cohen's Kappa per Class	0.75	0.66	0.72	0.48	0.9		
	Overall Accuracy (%)	**84.6**						
	Overall Kappa	**0.78**						

Since the images from Google Earth represent a compilation of different points in time, the Sentinel-2 dataset is used as an auxiliary dataset. Both data sets were acquired at different stages of flooding. Therefore, the visual impression of the Sentinel-2 dataset is given priority over the data from Google Earth when assigning water areas. Based on these datasets, land-use classes are interactively assigned to the test sample classes. Following this, the test areas are compared with the classification results to receive the accuracy measures (Tab. 4).

The overall accuracy of the classification is 84.6 %. The Kappa coefficient, a measure for the agreement between classification result and reference shows a good result of 0.78. The User's Accuracy shows how reliable the classified pixels represent actual land use, while Producer's Accuracy shows how well an object class has been correctly classified. In addition, the Kappa coefficients of each class are displayed in order to individually evaluate the reliability of the classification result.
The “Water” class is the most reliably classified with a User’s Accuracy of 94.0 %, reflected in the high Kappa coefficient of 0.9. The “Agriculture” (82.0 %) and the “Rural Settlements” (78.0 %) also show a high User’s Accuracy, compared to the classes “Bare Soil” and “Urban” with the lowest accuracies of 68.0 % (“Bare Soil”) and 52.0 % (“Urban”). This is also visible in the Kappa coefficients, thus the agreement between the classification result and the reference data is 0.75 (“Agriculture”) and 0.72 (“Rural Settlements”) compared to 0.66 (“Bare Soil”) and 0.48 (“Urban”).

The large connected water areas outside of Satkhira (Fig. A2) are polders built as part of the Costal Embankment Project (FENTON ET AL., 2017). Nowadays, these polders are almost permanently inundated and are used agriculturally for shrimp farming.
The reason for lower accuracy values of the classes “Bare Soil”, “Rural Settlements” and “Urban” (see Tab. 4) may be related to different circumstances:
For example, Tab. 4 shows that a notable number of “Bare Soil” samples were classified as “Agriculture”, which may be related to the different vegetation stages of the crops. Ripe grain plants, shortly before harvest, show a yellowish color. In this state of growth, plants contain a lower level of chlorophyll, which is related to a lower spectral reflection in the near infrared. Thus, these fields show a similar spectral signature as “Bare Soil” and may therefore be misclassified.
The spectral signature of the class “Rural Settlements” shows similarities to the spectral signature of the class “Agriculture” (Fig. 4). Therefore, rural settlement areas may be classified incorrectly and lead to a lower User’s Accuracy.
The relatively low accuracy value (52.0 % User’s Accuracy) of the “Urban” class may be related to a mixed-pixel problem in the Sentinel-2 dataset. Individual residential or industrial buildings may be smaller than the resolution of the Sentinel-2 dataset (10m x 10m). As a result, a pixel represents a mixture of urban buildings and other surfaces (e.g. soil or trees). This mixture can lead to misclassification. Due to the high-resolution reference image, it is possible to interactively determine the main content of a pixel

(e.g. urban buildings) and to assign it to the test sample classes. The mixed pixels of the Sentinel-2 dataset can thus lead to a lower accuracy in the "Urban" class.

The overall visual impression of the classification result (Fig. A2), as well as the overall accuracy and the overall Kappa coefficient (Tab. 4) show a good result and representation of the actual land-use.

2.2 River Shifting Change Detection Map

Rivers in Bangladesh are highly dynamic and underlie severe changes in location and intensity during a few years. During a few decades, rivers may change whole landscapes. The overall goal of this analysis is to provide information on the changes of the river courses and the directions of shifting in the region of Satkhira. The rivers includes the water bodies and pointbars. A regional map covers these changes from the area of Patkelghata in the northwest to the area of Paikgachha in the southeast (Fig. A5). River course maps are provided for six time slices (1973, 1980, 1990, 2000, 2010 and 2019) (Fig. A10-A15). The change detection map shows data of the time slices with the highest difference in river system areas (1973, 1990 and 2019) (Fig. A17; A10, A12, A15).

The river course maps and the change detection map are only showing the changes in the eastern part of the regional map (Fig. A5) where the rivers have a width that can be mapped using the spatial resolutions of the satellite data. Rivers in the western part and in Satkhira (e.g. Morrichap River, see Fig. A5) are often smaller in width than the spatial resolution of the satellite images available (10m to 60m, see A6, A7, A8). Additionally, these rivers are also often vegetation overgrown or tree canopied. Inundated agricultural land, immediately adjacent to rivers, also prevents a differentiation between rivers and surrounding landscape.

Data

To carry out the analysis, cloud-free optical images from Landsat Multispectral Scanner System MSS, Landsat Thematic Mapper TM and Copernicus Sentinel-2 missions are used. These are available during the period of the Bangladesh dry season between October and April, and images from January and February are used in the analysis. A comparison between images of different years is only possible when the target features (e.g. water) can be identified in all the images by similar response

signal. This can be ensured by using images of the same month in every year of the analysis.

Starting 1973, one image per decade is used (1973, 1980, 1990, 2000, 2010 and 2019). To enable comparability between the final river shifting products, only bands from the Landsat and Copernicus Sensors with similar wavelengths positions have been chosen for processing (see Tab. 5 and Annexure C: Data).

Table 5: *Overview of the satellite images and their bands used for the analysis (EUROPEAN SPACE AGENCY 2017; UNITED STATES GEOLOGICAL SURVEY n.d.).*

Mission	**Sensing Date**	**Bands (B), Spatial Resolution/ Wavelengths**	
		Green	**NIR**
Landsat MSS	21.02.1973	B4, 60m 0.5-0.6 µm	B7, 60m 0.8-1.1 µm
	21.02.1980		
Landsat TM	14.01.1990	B2, 30m 0.52-0.6 µm	B4, 30m 0.76-0.90 µm
	11.02.2000		
	06.02.2010		
Sentinel-2	14.02.2019	B3, 10m 0.538-0.583 µm	B8, 20m 0.76-0.97 µm

Methods

The workflow of the analysis is visualized in Fig. 5.

Atmospheric Correction

Different atmospheric conditions during the sensing times of the images can result in a different image feature of the physically same ground objects. Therefore, to enable the comparison between all the images, an atmospheric correction is mandatory. An atmospheric correction eliminates the atmospheric effects in an image and results in a surface reflectance image that characterizes the surface properties.

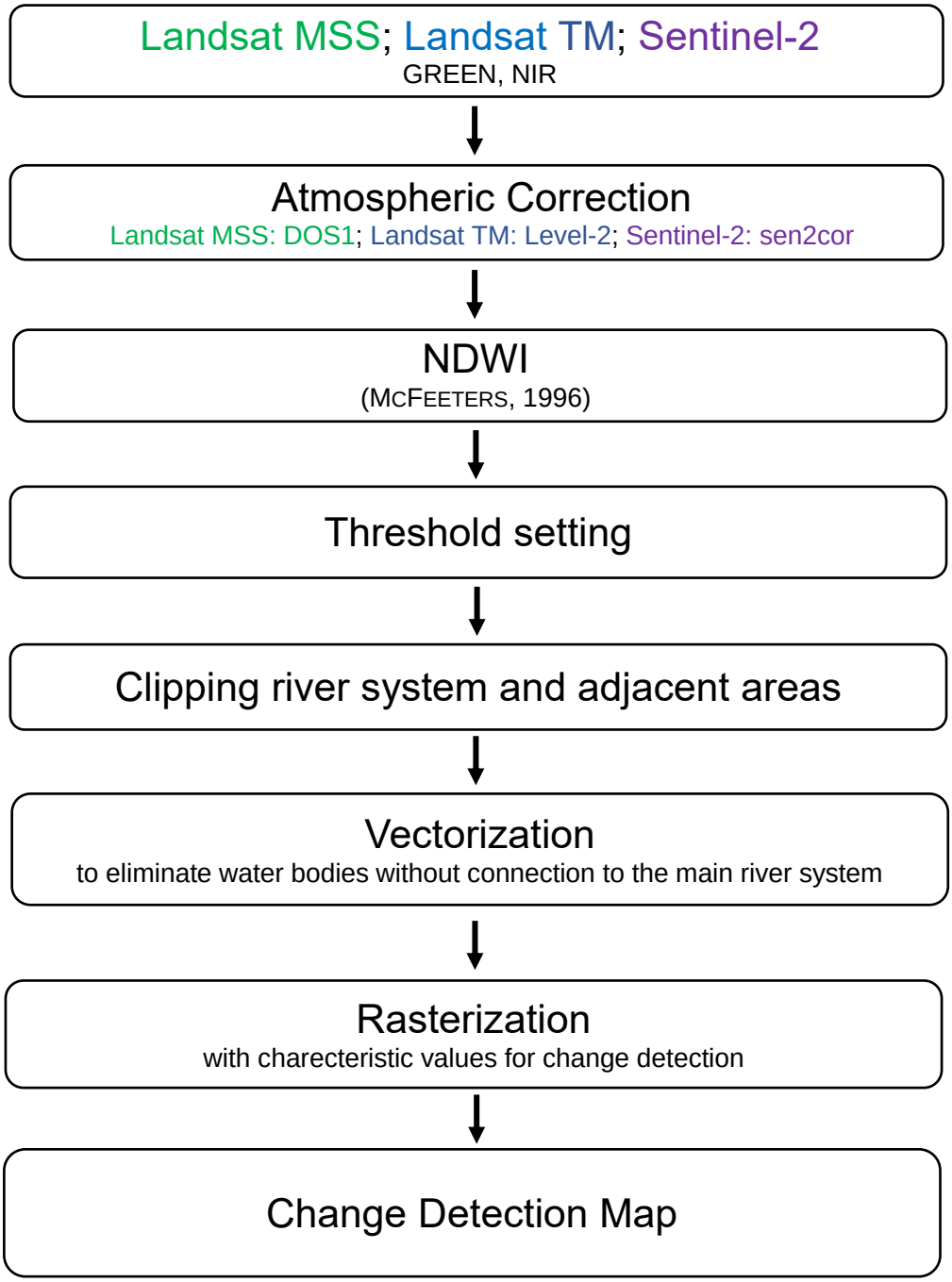

Figure 5: *Workflows of the River Shifting Change Detection analysis.*

Sentinel-2 and Landsat TM images are already atmospherically corrected and surface reflectance data are available for download (free Sentinel-2 download from Copernicus Open Access Hub and free Landsat TM download from USGS EarthExplorer).

The Sentinel-2 atmospheric correction is based on physical principals, physical-based algorithms use radiative transfer methods, which are simplified models of the radiation pathway from source to sensor, to model atmospheric scattering and absorption (LILLESAND ET AL., 2015). Auxiliary data such as water vapor data, atmospheric pressure or a digital elevation model are added to receive more precise information for the correction. The effects in the atmosphere are quantified by the model and used to calculate the surface reflectance values.

The Landsat TM surface reflectance "products are generated by a specialized software called Landsat Ecosystem Disturbance Adaptive Processing System (LEDAPS)" (LEDAPS PRODUCT GUIDE, 2020). Similar to the Sentinel-2 atmospheric correction, LEDAPS is also a physical-based algorithm that fits a radiative transfer model and includes auxiliary data to receive the atmospherically corrected surface reflectance product.

The Landsat MSS image is corrected by using the DOS1 (Dark Objects Subtraction) method. CHAVEZ (1996) describes that the methods "[…] basic assumption is that within the image some pixels are in complete shadow and their radiances [if above zero] received at the satellite are due to atmospheric scattering (path radiance). This assumption is combined with the fact that very few targets on the Earth's surface are absolute black, so an assumed one-percent minimum reflectance is better than zero percent." (CHAVEZ, 1996). The calculated radiance-value based on this assumption is used for the correction of the whole Landsat MSS image (image –based correction).

It is important to mention that the accuracy of an image-based correction technique is lower than a physically based correction (e.g. as applied for Sentinel-2) (CONGEDO, 2016). Nevertheless, CONGEDO (2016) states that image-based corrections "are very useful when no atmospheric measurements are available as they can improve the estimation of land surface reflectance" (CONGEDO, 2016).

Calculation of Normalized Difference Water Index (NDWI)

Using the respective bands of the images (Tab. 4), the NDWI is calculated (see Fig. A7). The Normalized Difference Water Index (NDWI) (MCFEETERS, 1996) uses the green and near-infrared bands to delineate open-water features.

Water surfaces show high reflections in the green and low reflections in the near-infrared wavelength region (see Fig. 6).

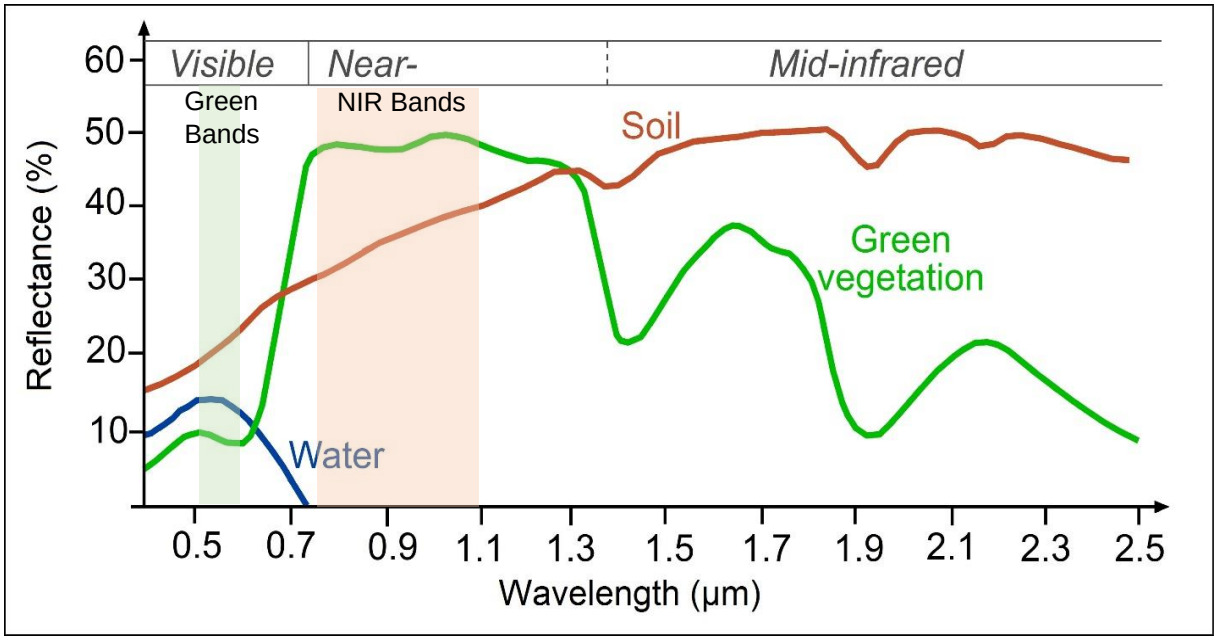

Figure 6: *Reflectance of water, soil and vegetation at different wavelengths; the wavelength areas used by the NDWI are highlighted in green (green bands) and red (NIR bands), modified after SEOS-PROJECT.EU, 2020.*

These differences are used to calculate an index that enhances the presence of open water features and suppresses the presence of soil and vegetation (McFeeters, 1996). The Waterindex is calculated as follows, using the respective bands of the satellite image:

$$NDWI = \frac{GREEN - NIR}{GREEN + NIR}$$

The generated index map contains values in the range of -1 to +1 (see Fig. A6), while excluding zero. Positive values are interpreted as water features. Soil and vegetation features have negative values (McFeeters, 1996).

Processing steps

At first, a threshold value is applied to discriminate between values that belong to the river system (water-bodies and pointbars) and all other values. This threshold value is defined manually by inspecting the pixels of the different NDWI images (see Tab. 6).

Table 6: *Thresholds to discriminate between river system and other values.*

NDWI image of the year	Threshold
1973	-0.28
1980	0
1990	-0.03
2000	-0.03
2010	0
2019	0

The application of the thresholds results in maps that only show water-body and pointbar areas differentiated from other areas (see Fig. A9 as an example).

Based on these threshold maps, an area is clipped interactively (due to computing limitations of QGIS regarding data quantity) that covers mainly the river system (including water bodies and pointbars) and adjacent areas. In the next step, all remaining pixels of the river system in the clipped images are assigned the value “1”, whereas the areas below the threshold (see Tab. 6) are assigned NA.

The resulting image still includes many small objects that lie outside of the main riversystem (e.g. small ponds, agricultural canals). To eliminate these water bodies having no connection to the main river system, the raster data are vectorized and single isolated polygons are automatically eliminated, based on the assumption that the main river area shows in one connected polygon.

The results of all processed years are overlain to visualize the different extents (Fig. A8-A13). The three results with the greatest differences in extent are selected interactively and then processed for the change detection map: years 1973, 1990 and 2019 (Fig. A15).

Change Detection Map

The goal of the change detection map is to provide information on the changes of the Padma river system course and the direction of shifting. The changes are visualized in a single map. The conversion of the vector map (polygons) back to a raster map enables to present different river areas with characteristic values in a single map.

A unique year-dependent characteristic value is assigned to the cells of each new raster image (see Tab. 7). The raster cell size is set to 20 m, as this is the pixel size, needed by the successive project analyses.
The yearly products are joined to receive the change detection map of the area of the Padma river system for the different years (see Tab. 8).

Table 7: *Overview of the characteristic values per year.*

	1973	**1990**	**2019**
Characteristic value	1	10	100

Table 8: *Legend of the raster values in the change detection map.*

Raster value	**Area of the Padma river system in**
1	1973
10	1990
11	1973, 1990
100	2019
101	1973, 2019
110	1990, 2019
111	1973, 1990, 2019

Results and Discussion

The resulting maps are added in Annexure A (A5-A15) and described in this section. For better orientation, topographical information and some in Bangladesh well-known cities are included in the final map visualization of the remote sensing based products.

Extent of river system and its water body

As already mentioned, the NDWI values greater than the threshold lead to the classification of a larger area than just the water bodies as it includes water bodies and pointbars. All together is interpreted as full extent (maximum water coverage) of the Padma river system based on discussions with the GSB colleagues. As an example, Figure A16 shows the NDWI result for 2019 with a threshold greater than 0 overlain on the Sentinel-2 RGB 432 image from 2019. It is visible that the NDWI result represents the water body areas of the Sentinel-2 image.

Figure A10 to A15 show in blue the extents of the Padma river system (based on NDWI) in the years of 1973, 1980, 1990, 2000, 2010 and 2019.
The different levels of details between the final maps are caused by the different spatial resolutions of the images. Due to the higher spatial resolution, Sentinel-2 shows more details than Landsat TM and Landsat MSS (Tab. 5).
It can be summarized, that the general shape of river system for the different years is visible in all decades.

Change Detection Map

Based on the NDWI evaluations, the change detection map is calculated (Fig. A17). This map includes information on the shifting direction of the river system, together with the locations of land-loss and possible land-gain. Furthermore, it shows which regions were part of the river system for the period between 1973 and 2019 (Fig. A15, dark blue).
In several regions of the river areas, changes in time are observable (Fig. A17): In Section A, an anthropogenic conversion of a river segment is visible. Turquoise color indicates the location of the river system in 1973, orange color indicates the location in 1990; light green shows the location in both years (1973 and 1990). In the time-slices/years of 1973 and 1990, it is visible that both the eastern and the western part of the Harihar river have been part of the river system. In contrast, the time slice of 2019 indicates that only the western part of the river is still part of the whole river system. The Sentinel-2 image of 2019 (see Fig. A5) shows that the area of the river was mostly converted to agricultural land, crossed by a small channel at the place of the former river.
Section B shows a meander cut-off. The red color indicates the location of the river system in the year of 2019. In the years of 1973 to 1990 (also see Figs. A10-A12) the river course shows an eastward meandering bow in turquoise (1973), orange (1990) and light green (1973, 1990). The meander bow was cut off after 1990 and in 2019 the river course is visible in red color west of the meander bow. Comparing the position of the former meander bow to the Sentinel-2 image of 2019 (see Fig. A5), it can be shown that the former river area is used agriculturally. The agricultural overprinting of this area is so strong that the structure of the former meander bow is no longer recognizable in the landscape.

In section C, a developing river course is visible. Dark blue color indicates the river location in the years 1973, 1990 and 2019. Orange color shows the river location in 1990 and 2019; red color indicates the year 2019. The center of section C shows the river channel in dark blue. The adjacent orange and red areas to the north describe a northward river course development between 1973 and 2019. This development also indicates a continuous river erosion into this direction.
Section D shows another anthropogenic overprint of the river system. Dark blue color indicates the river location in 1973, 1990 and 2019. Light green color shows the river location in 1973 and 1990, while orange color indicates the river location in 1990. Directly in the center of the section a former riverbed is visible. Light green and orange colors indicate that this riverbed is not a part of the river system in 2019. A comparison with the Sentinel-2 image of 2019 (see Fig. A5) shows that the area of the former riverbed is nowadays used for agriculture. In contrast to the overprinting in Section B, the structure of the former riverbed is still recognizable in the landscape. Nevertheless, in comparison to the conversion in Section A the former riverbed is completely cut off from the present river system.

In conclusion, the Change Detection Map in Figure A17 shows significant changes of the river system between the years 1973 and 2019. Of particular note are the anthropogenic overprints of former parts of the river system by agricultural land-use. The cut-off meander bow in section B is no longer recognizable in single satellite images of today's landscape (Fig. A5) and could only be identified by comparing satellite images of different years (Fig. A17). In this context , the change detection map should be considered as a planning basis when identifying and developing urban areas as it provides an insight into the formation of today's land use areas.

2.3 Inundation Map

Due to climate change, Bangladesh is experiencing an increase in rural-urban migration movements. Therefore, the demand for safe building ground is very high. One result is an increasing lateral growth of urban areas. However, urban growth is limited to suitable building ground and eligible areas are often low-lying and therefore prone to flooding during the yearly monsoon season between May and October. Planning agencies may benefit from geodata on inundation-prone areas that are

reliable, available frequently and sustainable, easy to process and easily understandable.

The overall objective of this analysis is to receive a map that gives an overall impression on the frequency of inundation in areas that are at risk of flooding (Fig. A17) for the years 2015 to 2020. The analysis is carried out using 20 Sentinel-1 radar images from 2015 to 2020 and a threshold approach to differentiate between inundated and non-inundated areas. To ensure an easy processing of the large amount of multi-temporal radar data, the analysis is carried out using the online processing tool Google Earth Engine (see the programming code in Annex B).

The Bangladesh Water Development Board (BWDB) already established inundation mapping using Sentinel-1 datasets. In their annual flood reports, the BWDB is using an inundation map to verify the output of a flood-forecasting model (BANGLADESH WATER DEVELOPMENT BOARD 2018, pp. 92-93).

Data

The analysis is based on Copernicus Sentinel-1 images starting 2015, with operation of the Sentinel-1 sensor.

Google Earth Engine states to preprocess the images using the Sentinel-1 Toolbox to receive radiometrically calibrated images, terrain corrected and thermal noise removed (GOOGLE EARTH ENGINE DATA CATALOG, 2020).

A data selection from the rainy season in Bangladesh is required to map the maximum inundation. The selected images are acquired in “IW” (interferometric wide swath), the default acquisition mode of Sentinel-1 (EUROPEAN SPACE AGENCY, 2020). To differentiate between water and non-water pixels, the VH polarization is selected. Preliminary works in the study areas have shown that VH is the most suitable polarization for the detection of water. The respective spatial resolution of the VH polarization images is 10 meter.

The Bangladesh rainy season is roughly between May and October of each year. The time of maximum inundation for the study area of Satkhira is set to the months of June and July of each year. This assumption is based on the experience and knowledge of colleagues at the Bangladesh Geological Survey (GSB), the flood reporting by the BWDB (see e.g. BANGLADESH WATER DEVELOPMENT BOARD, 2017, 2018, 2019) and by interactively assessing and selecting the images from a period that show the largest

inundated areas. Since the exact dates of maximum inundation of a year are unknown, all available images of June and July of each year are processed in this analysis.
Finally, using the above-mentioned benchmarks, 20 Sentinel-1 images of descending orbits are selected for the processing (Annex B, lines 8-23). Annex C: Data lists the images in a table.

Method

The workflow of the processing in Google Earth Engine is visualized in Fig. 7. The selected images of each year are combined and mean values are calculated. The mean-value images are subsetted to fit the extent of the study area (see Fig. A19; Annex B, lines 24-29).

Thresholding

Water surfaces appear in black and dark gray colors in the averaged amplitude images (see Fig. A19). In order to identify a threshold value, the values of assumed water and non-water image areas are identified interactively. Based on experience in the definition of thresholds discriminating between water and non-water surfaces, the identified threshold values in Bangladesh range from -20 dB to -22 dB. For the Satkhira study area, a threshold value including values smaller than -20 dB is chosen and applied to images from all years (Annex B, lines 109-118). The output image only shows pixels smaller than the threshold, representing the inundated areas of each year (see Fig. A20).
All areas that have been inundated between 2015 and 2020, are compiled by combining the threshold images of all years into one image (see Fig. A17; Annex B, lines 120-123). The result is exported with a 20m spatial resolution, which is a requirement for further analyses in the project (Annex B, lines 129-141).

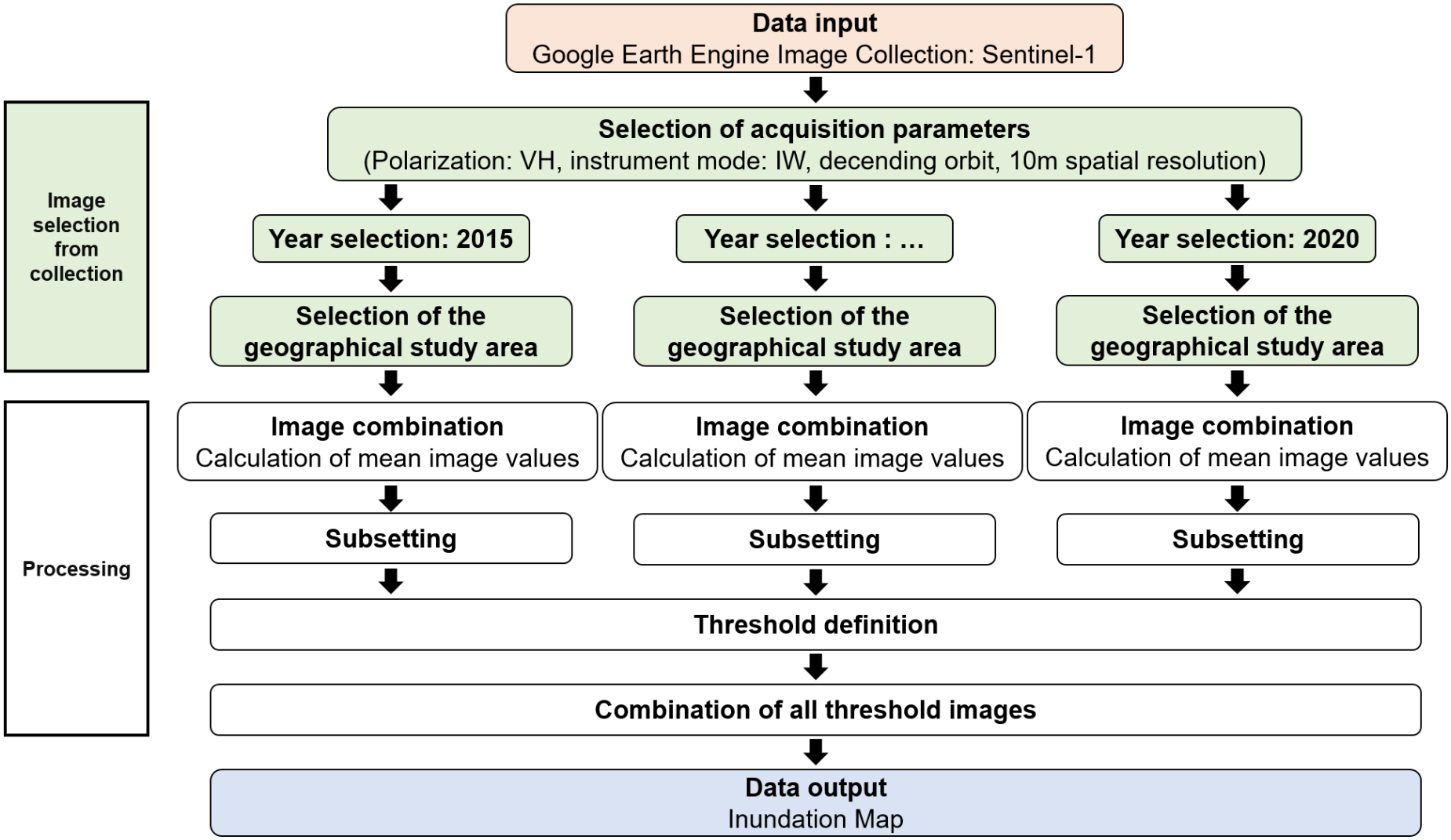

Figure 7: *Workflow of the Google Earth Engine processing of the inundation mapping method.*

Results and Discussion

The resulting map presents the areas and frequencies of inundation between 2015 and 2020 (see Fig. A18).

The map exhibits three major areas: (1) A larger north-south complex in the center of the study area, which shows the city of Satkhira (stretching from the landmark of Taltala in the north to the landmark of Miasaheberdanga in the south) with rarely inundated areas in the years from 2015-2020. (2) West of the city of Satkhira a large connected and frequently inundated area. The southern part is inundated every year of the six-year period, while the northern part includes areas that are less frequently inundated. (3) A north to south orientated area east of the city of Satkhira showing areas that were five to six times inundated during the study period. In this eastern part, it is visible that the number of areas frequently inundated decreases with shorter distance to the city. Many small areas in the Satkhira city area are inundated yearly, representing ponts and lakes as they partially overlap with the water bodies in the topographic base map (data of the Survey of Bangladesh and OpenStreetMap). Nevertheless, the majority of frequently inundated areas is located in the outskirts of Satkhira.

The area south-west of the town of Satkhira (around the landmark of Agunpur) is part of a polder built as part of the Costal Embankment Project (FENTON ET AL., 2017). Nowadays, these polders are almost permanently inundated and are used for shrimp farming. Therefore, the large connected frequently inundated areas are mainly caused by inundated polders.

It can be concluded that between 2015 and 2020 for the months June and July (rainy season) mainly areas in the rural outskirts of Satkhira were inundated. The frequent inundation occurs in the polder areas in the west used agriculturally and in the areas east of the study area. The urban area of Satkhira city experiences a non-annual inundation.

2.4 Ground Motion Map

2.4.1 Introduction

Within the project Geo-Information for Urban Planning and Adaptation to Climate Change (GPAC), a project of German-Bangladeshi technical cooperation and carried out by the Geological Survey of Bangladesh (GSB) and the German Federal Institute for Geosciences and Natural Resources (BGR), ground motion products based on

Radar Interferometry (InSAR) were created for several study sites in Bangladesh. The goal of these analyses is to establish a workflow for the systematic integration of ground motion data into a climate change adapted urban planning in Bangladesh. The availability of free, medium resolution, radar satellite images through the European Copernicus program and the progress in computing capabilities, open up new opportunities for the wide-scale, multi-temporal and continuous ground motion analysis based on satellite data.

In the context of an advancing urbanisation and the resulting increased demand in suitable building space, in combination with the particular exposure of Bangladesh to climate change related risks, InSAR ground motion products enable the identification and monitoring of potentially stable areas and can be used in the prediction of inundation scenarios. In combination with other relevant geodata, InSAR can hence contribute to the assessment of building ground suitability.

In this section, the results of the InSAR analysis for the city of Satkhira from January 2017 to December 2019 are presented and discussed.

2.4.1.1 SAR Interferometry (InSAR)

SAR interferometry (InSAR) is a technique for the precise measurement of topography and terrain movement in the range of several millimetres from two or more SAR images. The different methods used in this field have in common that they exploit the phase information contained in the images acquired from two or more different sensor positions (spatial baselines) and/or at different acquisition times (temporal baselines). Concretely, the phase difference between the different acquisitions (the so-called interferometric phase) implicitly contains information about the topography of the area of interest and – when data from different points in time is available – on any terrain movements during the observation period.

When terrain deformations are to be observed over a longer period, the issue of increasing loss of coherence - or decorrelation - between the different scenes arises. Coherence is estimated from the amplitude of the complex correlation coefficient of two SAR images. In the context of SAR interferometry, coherence is used as a measure to evaluate the quality of the phase difference and can take on any value between 0 and 1, where high coherence indicates high quality of the phase difference while low coherence indicates a highly noisy phase difference (LÓPEZ-MARTÍNEZ ET AL., 2004).

Decorrelation particularly affects areas with vegetation (forests, parks, farmland …) where the backscatter to the radar sensor is subject to high temporal variations due to quick changes in geometry (e.g. leaves moving with the wind) and dielectric properties (moisture variations). It also affects areas with a low backscatter to the sensor such as smooth surfaces (water, roads, airstrips …) or areas of radar shadow. In these areas, noise dominates the return signal (low signal-to-noise ratio). In essence, decorrelation occurs when the contributions of topography and deformation to the total phase difference are superimposed by random phase contributions and noise, and can no longer be isolated. As a rule of thumb, the longer the time gap between two acquisitions and the larger the spatial distance between the sensor positions (temporal and spatial baseline), the higher the degree of decorrelation (WOODHOUSE, 2006).

Therefore, if the goal is to examine deformation time series, one has to limit the analysis to image pixels that are less affected by decorrelation. That is, pixels that exhibit a strong and stable backscatter to the radar sensor even over long periods of time. These sort of targets are usually abundant in urban areas and correspond to man-made structures. In addition, natural targets such as rocks, gravel fields and even desert surfaces can be sufficiently stable over time to be considered for multi-temporal analyses. There are different approaches in this field of multi-temporal radar interferometry. Two approaches, Persistent Scatterer Interferometry (PSI, see FERRETTI ET AL. 2001) and Small Baseline Subset (SBAS, see BERARDINO ET AL., 2002) are used in the frame of this work and are described briefly in the following section.

2.4.1.2 Multi-temporal InSAR (PSI and SBAS)

Persistent Scatterer Interferometry (PSI) is a technique that relies on point targets, which have a strong backscatter and are stable over time (so-called persistent scatterers, PS). Within an image pixel, a PS has to be dominant while the backscatter contributions of the other objects (scatterers) within that resolution cell can be neglected. These conditions are normally fulfilled by artificial (i.e. man-made) objects which are particularly prevalent in urban areas. Examples include cell phone towers, roofs and edges of houses, bridges, metallic structures, utility poles, etc. These objects are referred to, in the context of radar interferometry, as persistent scatterers and can be identified within the image stack using different methods. Frequently, the amplitude stability over the observation period is considered for this purpose.

PSI is particularly effective in urban areas with a high density of point targets. In rural areas on the other hand, the number of potential PS is considerably less.

The PSI algorithm initially selects a master image from the stack of available radar acquisitions based on a minimisation of the average spatial and temporal baseline with respect to the other images in the stack. Secondly, one interferogram is created between the master image and each of the secondary images. All images in the stack of acquisitions are then zero baseline steered, i.e. the measured interferometric phases are adjusted for the different imaging geometries of the different acquisitions with respect to the master image, using an external DEM like e.g. SRTM and precise orbit information. The next step is the identification of PS candidates. Here, the classical approach is to use the amplitude stability over time. Subsequently, and using an iterative approach, the atmospheric and topographic phase contributions are calculated and removed and the deformation velocity for the PS is calculated. To do so, a deformation model is applied. In the most common case, a linear deformation model is used (see FERRETTI ET AL. 2001).

Small Baseline Subset (SBAS) is another method for multi-temporal radar interferometry that uses a network of interferograms. Instead of choosing a single reference image for all interferograms, groups (subsets) of images are considered that have been acquired with a small temporal and spatial baseline. Subsequently, for each image combination within a subset, an interferogram is calculated respectively (as long as a user-defined maximum temporal and spatial baseline is not violated). For this reason, in SBAS the number of interferograms is usually much higher than the number of available SAR acquisitions. In order to achieve a continuous motion time series, the individual subsets are subsequently linked together (see BERARDINO ET AL., 2002). Since SBAS tries to minimise the temporal and spatial baseline between the images of a particular subset, the resulting interferograms are less affected by decorrelation when compared to PSI. This leads to the detection of more stable points (scatterers) including natural objects such as rocks, gravel fields or desert surfaces. SBAS is also able to deal with disconnected subsets (although this should be avoided) and can interpolate over points that are affected by a temporal loss of coherence.

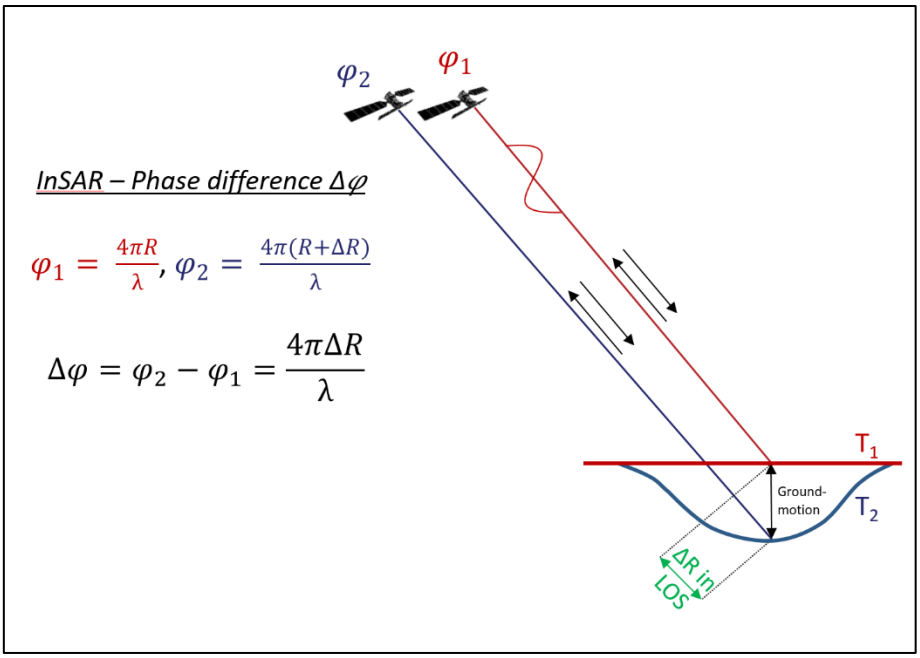

Figure 8: *Schematic representation of InSAR basic principle.*

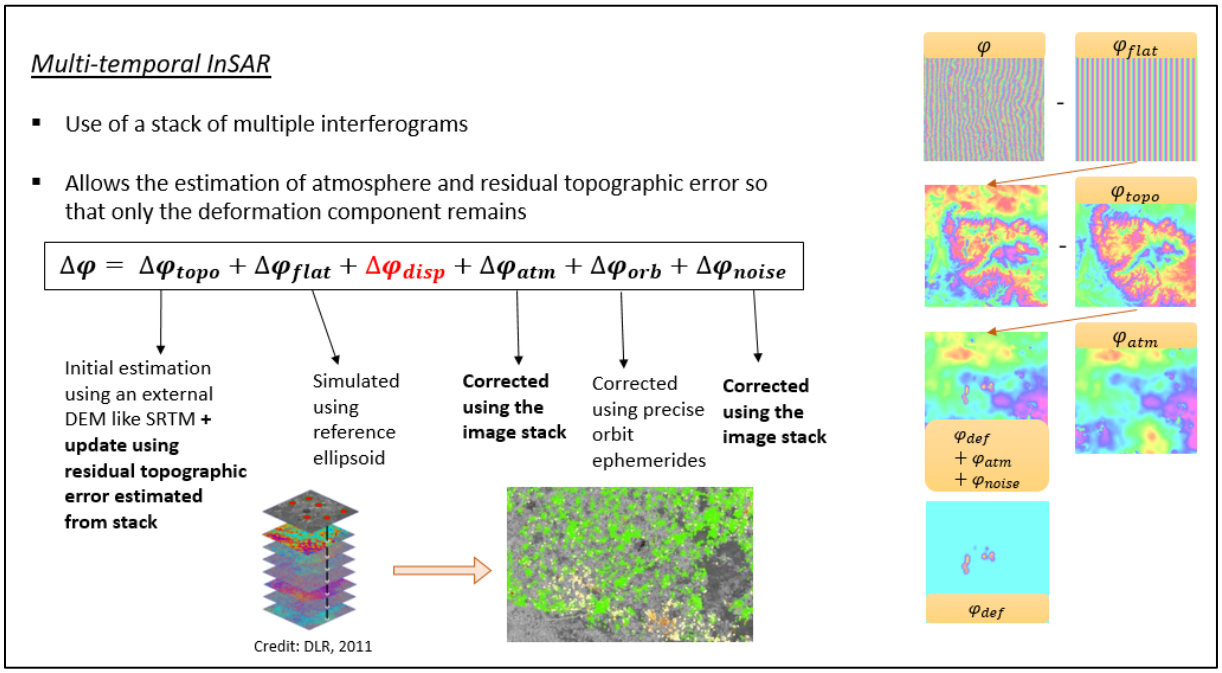

Figure 9*: Schematic representation of an interferometric stacking (multi-temporal InSAR) approach.*

2.4.1.3 Multi-temporal InSAR limitations

The deformation measured in radar interferometry is always along the line-of-sight of the imaging sensor/satellite and not the true vertical deformation. SAR sensors are not nadir looking but instead are looking at the ground obliquely with an incidence angle. For Sentinel-1 this angle is between 20 and 45 degrees with respect to nadir. However, the vertical deformation component can be estimated with a certain probability using

adjustment calculation if acquisitions from both satellite orbit directions (ascending and descending) are available. In this case, two images acquired in different orbits with different look angles are used to estimate the vertical motion component and one horizontal motion component (usually the east-west component is estimated since the north-south component is not well constrained by most satellite imaging geometries). Furthermore, in radar interferometry all the estimated velocities and displacements are relative to one or several reference points. The principal reference point is assumed to be stable over the whole observation period, an assumption that is not always true. In order to get the absolute motion, GNSS or other survey data is required, to which the dataset can be referenced instead. For our analyses within the GPAC project, no external reference data is used, as no adequate GNSS are available.

Another aspect that needs to be considered is the ability to exactly assign a particular deformation measurement to an object on the ground. For the German Ground Motion Service (BBD) a mean geolocation accuracy of 3.5 metres for strong point targets was shown (KALIA ET AL., 2020). In the case of SBAS, assigning a particular object to an observation proves more challenging since SBAS applies spatial averaging of adjacent pixels, merging together signals from numerous individual scatterers.

The ambiguous nature of the phase information contained in SAR images (only displacements corresponding to fractions of a wavelength can be measured) means that InSAR is limited in its ability to measure fast displacements. In fact, the maximum theoretical displacement that can be measured between two scenes corresponds to one fourth of the wavelength. CROSETTO ET AL. (2016) described the maximum differential accumulated deformation rate measurable with Sentinel-1 with 42.6 cm/year. A final limitation that needs to be mentioned is the availability of coherent targets. While SBAS is able to detect a high density of targets even in rural areas, neither technique (PSI or SBAS) can provide information in areas where there are strong changes in ground cover over time (for example seasonally flooded fields).

The BGRs Remote Sensing Working Group is mainly using ENVI SARscape software for InSAR processing. This software is developed by the Swiss company sarmap S.A. and is fully integrated into ENVI. For PSI, SARscape currently only supports linear deformation models while the SBAS implementation in SARscape also supports non-linear models.

2.4.2 Methods

2.4.2.1 Project area

Satkhira (see Figure 10) is a city in the south-west of Bangladesh and capital city of the Satkhira Division. The city is located only around 100 km from the coast in a low-lying area dominated by agriculture and shrimp farming that sees frequent seasonal inundations (see Chapter 2.3 Inundation Map) .Satkhira had a population of around 113,000 people in the 2011 government census. Satkhira has a flat topography without any pronounced features and an average elevation of roughly 5 to 10 meters above sea level. The city is surrounded by large agricultural areas and by large-scale polder areas in the south used for shrimp farming.

As other cities in Bangladesh, Satkhira has seen its population grow over the past decades. In particular the city centre has seen, over the past 20 years, a densification and the construction of several new buildings, including high-rise buildings. Nonetheless, the city remains relatively small in size when compared to other large cities in Bangladesh and is still dominated by low-rise buildings and a high share of vegetation. Compared to other cities in Bangladesh, Satkhira also does not have any large, sprawling suburbs but is instead mostly surrounded by agricultural areas. In the south-west of Satkhira the Satkhira Medical College is currently under construction. The college campus comprises an area of over 20 hectares and includes a hospital and several dormitories.

While the Satkhira project area has a size of 63 km², for the InSAR analyses a larger area of 162 km² is chosen. This area covers the city of Satkhira and its immediate suburbs. Even though the deformation dynamics within the city of Satkhira are the main focus of this work, a larger area was consciously chosen for the InSAR processing, to enable a higher selection of potential reference points in the phase unwrapping part of the processing.

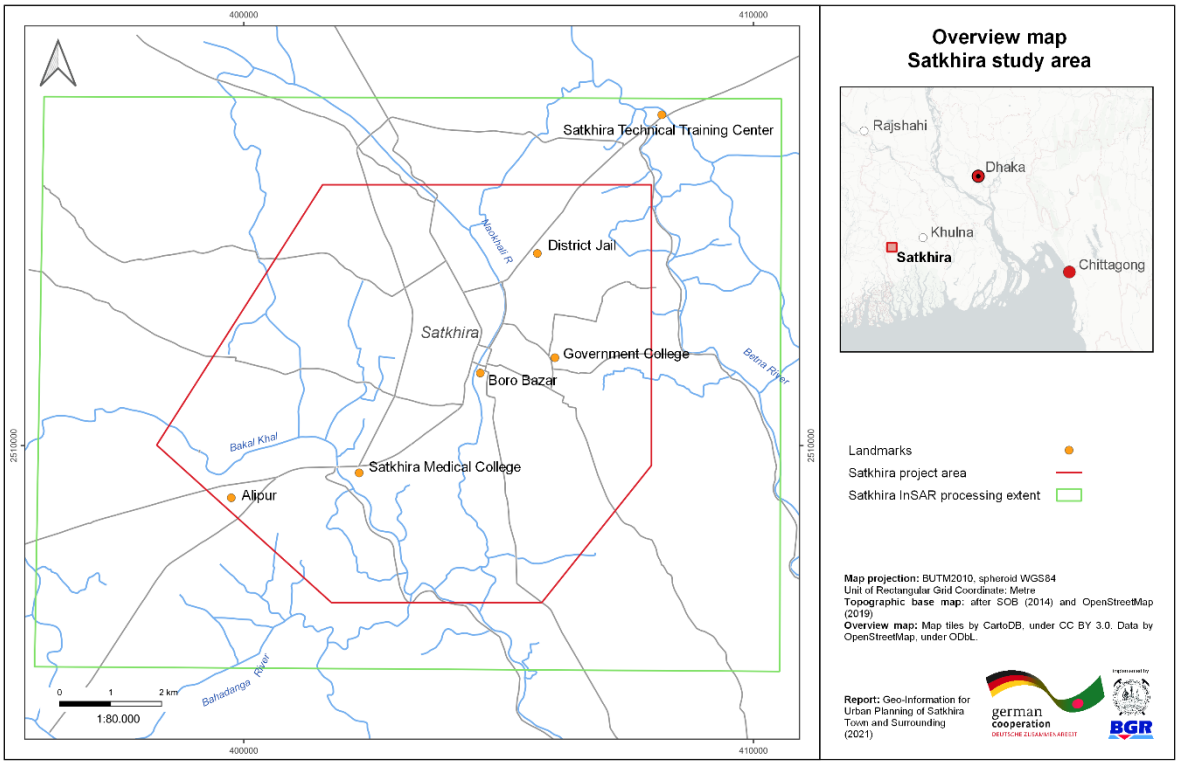

Figure 10: *Satkhira study area.*

2.4.2.2 Data and data download

The radar interferometry analyses carried out within the scope of the GPAC project are based on Sentinel-1 data. Sentinel-1 is a C-band radar satellite constellation operated by the European Space Agency (ESA) consisting of two identical satellites – Sentinel-1a and Sentinel-1b. The data is distributed free of charge by ESA. In addition, for the Satkhira project area, TerraSAR-X/TanDEM-X data is used. These are two high resolution X-band satellites that are flying in a close formation and are operated by the German Aerospace Centre (DLR) and Airbus (see AIRBUS DEFENCE AND SPACE, 2015). For the Satkhira project area, Sentinel-1 data covering the period from January 2017 to December 2019 in the ascending and the descending orbit direction are used. Only data starting from 2017 are used since no earlier data is available in the ascending orbit and both orbit directions are needed to calculate the vertical displacement rates. In total, 167 Sentinel-1 scenes are used for the InSAR analyses (see Annexure C: Data).

Sentinel-1 data are freely available for download from the Copernicus Open Access Hub (https://scihub.copernicus.eu/) and from the Alaska Satellite Facility (ASF) (https://asf.alaska.edu/).

For this project, all Sentinel-1 data are downloaded through the ASF. For more details on the download process, please refer to the *Interferometric Stacking in SARscape Processing Guidelines*.

Additionally, TerraSAR-X and TanDEM-X X-band data covering the period November 2017 to November 2019 and both orbit directions is used. A total of 122 TerraSAR-X/TanDEM-X scenes or roughly 3 scenes per month and orbit direction are used (see Annexure C: Data).

2.4.2.3 Orbit files download

In addition to the image files, it is necessary to download the so-called precise orbit ephemerides files. These are highly precise satellite position vectors, which are available online 20 days after the Sentinel-1 acquisitions are published. These vectors are necessary for InSAR processing, since the exact sensor position at the time of acquisition is needed for high quality InSAR results. The orbit files can be downloaded from the Sentinel-1 Quality Control website (https://qc.sentinel1.eo.esa.int/).

For an InSAR analysis only those Sentinel-1 scenes should be considered, which are older than 20 days at the time of the analysis. The accuracy of the satellite positions after the update using precise orbit information is given by ESA with 5 cm (3D RMS). For more information on the orbit file download, please refer to the Interferometric Stacking in SARscape Processing Guidelines.

The TerraSAR-X data was already delivered with updated precise orbit information.

2.4.2.4 SARscape PSI and SBAS workflow

ENVI SARscape is used in this project for InSAR processing. The PSI workflow within the software consists of five steps: Connection graph, Interferometric process, Inversion: First Step, Inversion: Second Step and Geocoding. Once both orbit directions are processed until the Geocoding step, the tool Shape Combination is used to combine both datasets and estimate the vertical deformation component.

SBAS processing was also done using ENVI SARscape. The SBAS workflow consists of seven iterative steps: Connection Graph, Interferometric Process, Ground Control Point Selection, Refinement and Re-Flattening, Inversion: First Step, Inversion: Second Step and Geocoding. As with PSI, both orbit directions were processed separately and then merged using the Meta Combination tool. In following, the processing steps are briefly explained.

The first step in the PSI and SBAS processing chain is the **Connection Graph** tool. For PSI, this function analyses the stack of SAR images and selects the best master image from the stack (based on temporal and spatial baseline). All differential interferograms are subsequently formed with this master image. For SBAS the tool creates a network of image connections based on a user defined maximal temporal and spatial baseline (see Figure 11). For every image connection, an interferogram is formed in the following step. Not all images in the network need to be directly connected to each other. Ideally, however, all images are connected at least indirectly. The Connection Graph tool also creates a working directory in which the outputs of all the processing chain's steps are stored and creates the auxiliary.sml file in the working directory. This file is needed as an input to all the following steps and it contains information about the data used and the progress of the processing chain.

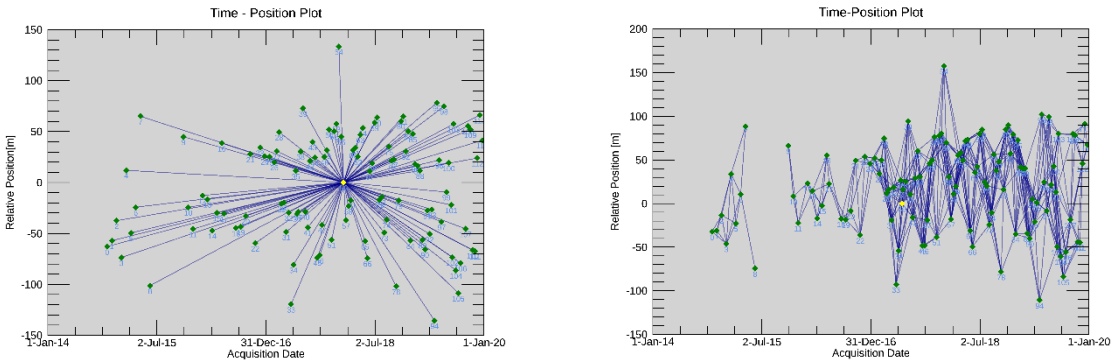

Figure 11: *Right: PSI connection graph with one master image and only one connection between master and each child; Left: SBAS connection graph showing multiple connections for each image and two disconnected blocks.*

In the **Interferometric Process**, the interferograms between all image pairs are generated. To do so, all images are first co-registrated, i.e. they are aligned in such a way that each pixel in the child image represents the corresponding object in the master image. This is achieved by locally matching the image intensity values using a maximisation of local cross-correlation between master and child image.

After co-registration, each master image is multiplied by the complex conjugate of the child image. The phase of the resulting complex interferogram corresponds to the phase difference between master and child image. This phase difference is retained, the so-called interferometric phase. This phase has multiple contributions of which the most important ones are the different atmospheric attenuation between the two acquisitions, the topography, the so-called flat earth contribution and the deformation

that occurred between the two acquisitions. Since we are only interested in the latter contribution, the others need to be cancelled out as best as possible.

The flat earth phase is the phase contribution which comes from the variation of range distance across the image due to the curvature of the earth. This contribution can be removed by using an ellipsoid in a process called interferogram flattening. The topographic phase contribution can be initially estimated using a digital elevation model (DEM) such as SRTM and the satellite orbit information. This estimate is further refined in the following steps of the workflow. Similarly, the atmospheric contribution is estimated in the following steps of the workflow.

For PSI, the Interferometric Process includes the steps coregistration, interferogram generation and interferogram flattening (which includes removal of flat earth component and topographic phase component). Contrary to “standard” InSAR processing, no spatial filtering is applied and point targets (individual objects with a strong backscatter to the sensor) are preserved.

For SBAS, the Interferometric process also includes coregistration, interferogram generation and interferogram flattening but also includes filtering of the flattened interferogram to reduce phase noise and an initial phase unwrapping (transformation of the interferometric phase from multiples of 2π to absolute values using appropriate reference points).

The next step in the SBAS workflow, **Refinement and Re-Flattening**, uses user defined reference points to correct for possible orbit inaccuracies and large-scale atmospheric influences.

In the **Inversion: First Step** an initial estimate of the model parameters (residual height and displacement information) is undertaken. In the case of PSI, the algorithm identifies a number of coherent targets (Persistent Scatterers, PS) and analyses the phase history of these targets only. Initially, only highly coherent targets are considered and their information is used to get a first estimate of the model parameters. In the case of SBAS, the input scenes are processed in whole, the residual height and displacement related information are estimated from the interferometric phases and the phase unwrapping is re-done to generate higher quality products.

In the **Inversion: Second Step** the atmospheric phase components are estimated. This step is identical for both PSI and SBAS. The atmospheric phase contributions are estimated, removed from the interferometric phase and the date-by-date displacements are estimated for all images in the stack.

Finally, in the **Geocoding** step, the calculated displacement information is geocoded from SAR slant range geometry into a geographic coordinate system.

All steps are explained in detail in the document Interferometric Stacking in SARscape Processing Guidelines. The processing parameters are detailed in Annexure D: SARscape processing parameters.

2.4.3 Results

2.4.3.1 PSI processing

Using the SARscape PSI workflow, both datasets (Sentinel-1 and TerraSAR-X/TanDEM-X) were processed in both orbit directions (ascending and descending) respectively. The results for each dataset were combined (decomposed) to obtain the vertical and east-west motion component. Finally, the results were filtered such that only persistent scatterers with a temporal coherence value >= 0.7 were retained.

The decomposed Sentinel-1 PSI dataset contains more than 9,400 points (persistent scatterers) and covers the time period from January 2017 to December 2019. Figure 12 shows the average vertical ground motion velocity for the Satkhira project area obtained by the PSI multi-temporal InSAR approach using the Sentinel-1 dataset. The original dataset, where each measurement location is represented by a point geometry, is converted into raster format for visualisation purposes for this report. A single pixel value in Figure 12 is the mean displacement velocity value of all points within that raster cell. Green and beige colors correspond to points, which are stable, blue tones to points that have experienced an uplift during the observation period, and red points correspond to areas of subsidence. The figure shows the highest point density around Boro Bazar commercial area and in the city's more densely built up areas. As expected, almost no points are found within the large agricultural areas that surround the city, as these areas are mostly free of stable targets.

Figure 12 shows relatively little movement in most of the project area. Most of the city and its surrounding areas are moving only slightly or are stable within the margin of error (+/-2 mm/year). Only a few isolated points of strong subsidence can be found within the city centre. The only larger cluster of strong subsidence is found outside the city centre on the newly built campus of the Satkhira Medical College.

The decomposed TerraSAR-X PSI dataset, covering the period from November 2017 to November 2019, contains more than 74,000 persistent scatterers (Figure 13).

The point density is high in almost all the urbanised areas and higher than in the Sentinel-1 PSI dataset (for an explanation see section 2.4.4). Using TerraSAR-X data, more points are detected in the suburban areas of Satkhira and the rural settlements surrounding the city. However, as with Sentinel-1, the agricultural areas surrounding the city are largely not captured due to a lack of suitable targets.

Figure 13 shows a similar picture to Figure 12. Most of the city centre of Satkhira is moving only slightly (less than +/- 5 mm/year) or is stable within a margin of error of +/- 2 mm/year. As with the Sentinel-1 dataset, a few points of strong subsidence (> -5 mm/year) are found within the city, but no large clusters. Data on the Satkhira Medical College campus is available in the TerraSAR-X descending dataset but not in the ascending dataset, where there are no scatterers available that meet the coherence threshold of 0.7. Since data from both orbit directions is needed for the decomposition of the line-of-sight measurements into vertical measurements, no information on this area is available in the decomposed dataset.

Furthermore, on the TerraSAR-X data several areas of uplift are detected that are not visible on the Sentinel-1 data. In particular, one area in the northeast is noticeable, stretching over 3 km from the District Jail to the Satkhira Technical Training Center. This area is experiencing an uplift of +5 to +10 mm/year over the observation period. In the Sentinel-1 based PSI data, this area only contains a few measurement points. The few points that are available in the Sentinel-1 PSI dataset also indicate a positive deformation trend but with a magnitude of only +2 to +5 mm/year.

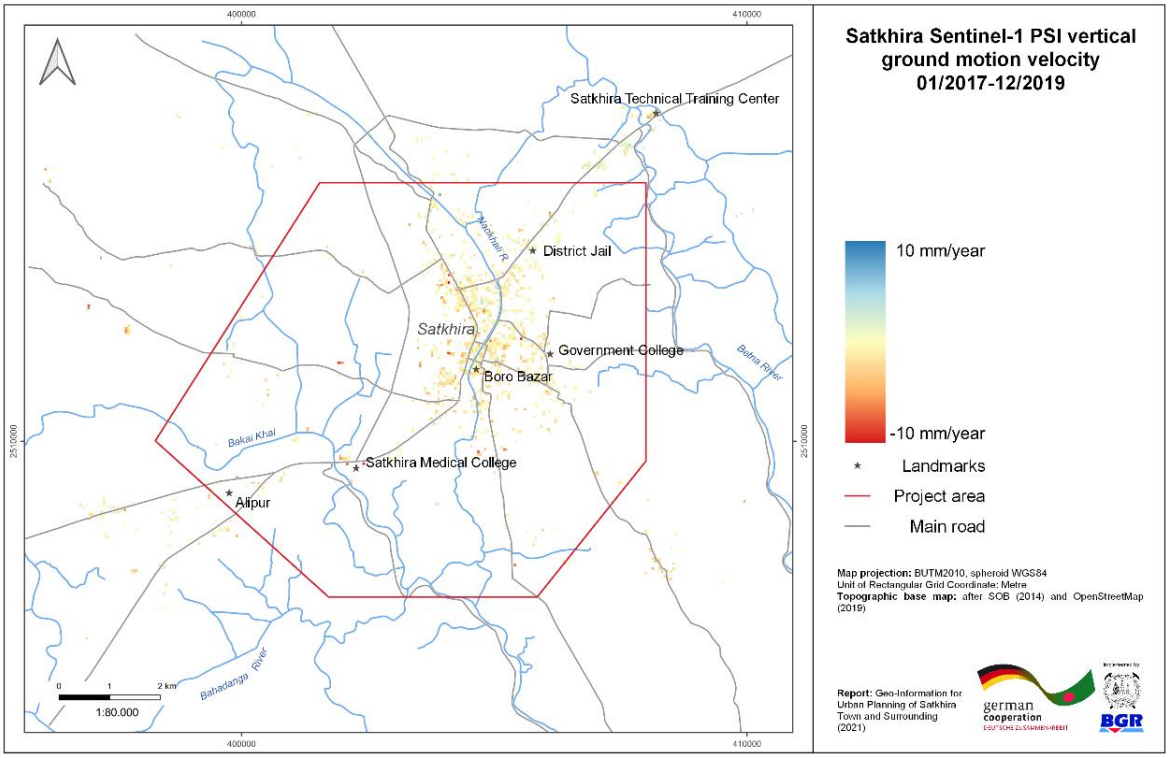

Figure 12: *Sentinel-1 PSI vertical ground motion velocity, Satkhira project area.*

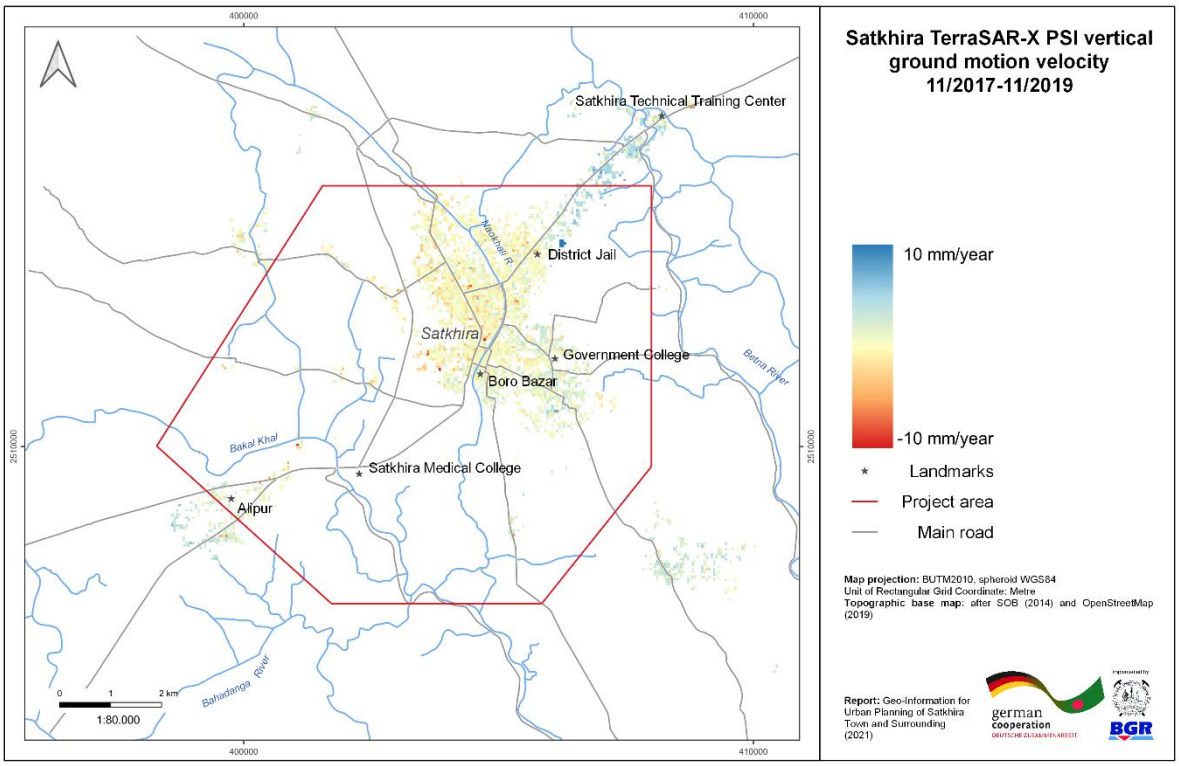

Figure 13: *TerraSAR-X PSI vertical ground motion velocity, Satkhira project area.*

2.4.3.2 SBAS

SBAS results are obtained using the SBAS workflow within the SARscape software. As with PSI, both orbit directions are processed separately and then merged to obtain the vertical motion component.

Figure 14 shows the average SBAS vertical ground motion velocity in Satkhira for the period January 2017 to December 2019 obtained using Sentinel-1 data. The dataset is notably denser than the Sentinel-1 PSI dataset and is also covering a much larger area (comparable to the TerraSAR-X PSI spatial coverage). Within the city centre, and where data from both datasets are available, the results seem to match well within the Sentinel-1 and TerraSAR-X PSI results. Large parts of the city and its surrounding areas fall within the error margin and can be considered stable during the observation period. The data show only punctual strong subsidence within the city centre, affecting for example the stadium and several newly built high rises along the city's main street. Outside of the city centre however, several clusters of strong subsidence are visible in the SBAS data. For example, around the Satkhira Medical College, in the northeast around the Satkhira Technical Training Center, and to the east along the banks of the Betna River (though the latter two are located outside of the project area).

Overall, the SBAS dataset makes it easier to detect large-scale deformation patterns and enables the detection of several clusters of strong subsidence not visible in the PSI data. SBAS provides information in areas where the PSI method delivered no results or PSI point density is low. However, the SBAS dataset is also showing gaps in areas that are subject to strong changes over time, such as agricultural areas. Furthermore, while the coverage outside of the city centre is much larger using SBAS than using PSI, the small-scale motion patterns within the city centre and on individual buildings are lost.

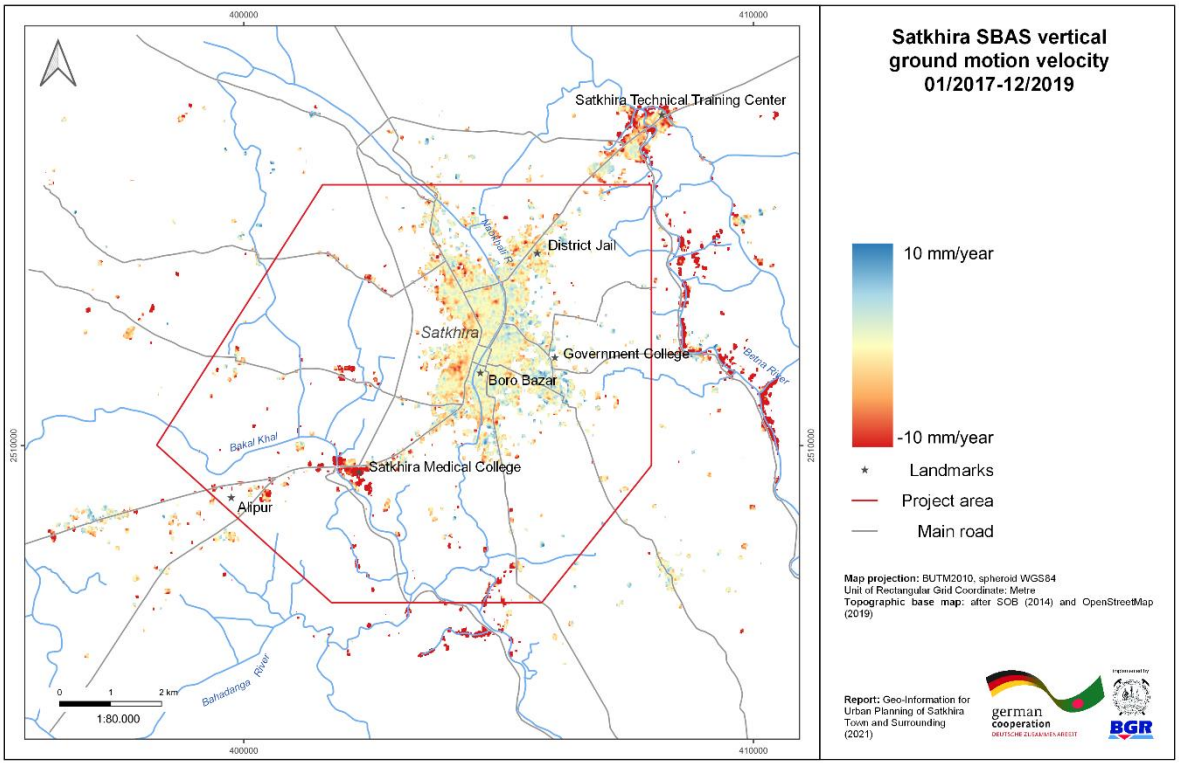

Figure 14: *Sentinel-1 SBAS vertical ground motion velocity, Satkhira project area*

2.4.3.3 Comparison of results

When comparing both Sentinel-1 datasets, it is immediately evident that SBAS achieves a higher spatial coverage than PSI. The difference is particularly striking in areas outside of the city centre. This is due to the ability of the SBAS approach to deal with so-called distributed scatterers (DS) like open fields, rocks and other geometrically not well-defined objects. The SARscape implementation of the SBAS algorithm is also able to handle objects that are affected by low coherence or even coherence loss for some parts of the observation period. When comparing the SBAS results with the TerraSAR-X PSI results, their spatial coverage is similar. The areas where both datasets do not match well are in the north and northeast of the project area, where the SBAS coverage is low while the TerraSAR-X PSI coverage is high and in the hamlet of Alipur in the southwest of the project area, where the TerraSAR-X coverage is higher than the SBAS coverage. On the other hand, SBAS coverage is higher to the south and southwest of the city centre, an area where the Satkhira Medical College and several other newly built structures are located.

Where there is coverage in both the SBAS and PSI data, generally both show similar trends. This is true for the Sentinel-1 and the TerraSAR-X derived PSI datasets. All three datasets reveal, that most of the city centre can be considered stable within the margin of error (+/-2 mm/year) or moving only slightly (+/-5 mm/year) with only punctual strong subsidence. Outside of the city centre, there are significant differences in particular between the two Sentinel-1 datasets, mostly due to the much larger spatial coverage of the SBAS dataset. The biggest difference in coverage is in the rural or suburban settlements, which are areas with a high share of vegetation. Here, PSI delivers only punctual results and in some areas even fails to deliver any results, while SBAS delivers spatially dense and coherent information about these areas.

The largest observed vertical motion rates are -64.66 mm/year and +17.15 mm/year for the SBAS dataset, -17.66 mm/year and +6.82 mm/year for the Sentinel-1 PSI dataset and -20.84 mm/year and +17.83 mm/year for the TerraSAR-X PSI dataset respectively (see Table 9).

Table 9: *Basic statistics for PSI and SBAS Sentinel-1 (S1) and TerraSAR-X (TSX) datasets.*

Dataset	Minimum velocity [mm/year]	Maximum velocity [mm/year]	Mean [mm/year]	Standard Deviation [mm/year]
PSI S1 vertical	-17.66	+6.82	-0.83	1.82
PSI TSX vertical	-20.84	+17.83	+0.90	2.01
SBAS S1 vertical	-64.66	+17.15	-3.29	7.92

In both Sentinel-1 datasets, the Satkhira Medical College campus is the area with the strongest observed subsidence rates within the project area. In the PSI dataset, almost all points with a velocity < -10 mm/year lie in this area. In the SBAS dataset, vertical velocities of up to -40 mm/year are observed here. Even stronger subsidence with vertical velocities of up to -60 mm/year is observed along the bank of the Betna River, east of Satkhira (though this area lies outside the project area). The Satkhira Medical College was only recently established and the campus features a large number of newly erected buildings and from current Sentinel-2 data, it is visible that construction in parts of the campus is still ongoing. The Betna River bank where strong subsidence rates are observed in the SBAS dataset (in the PSI dataset no information about this area is available) is dotted with brick factories, shrimp farms and low-rise residential buildings.

In the TerraSAR-X PSI dataset, the points of strongest observed vertical subsidence are located to the southwest of the city centre. This area shows very heterogeneous deformation patterns with many stable points and a few isolated points of strong subsidence (above -15 mm/year). Other (isolated) points of strong subsidence are found in the city centre on several large buildings. No clusters of points of strong subsidence are found in the decomposed TerraSAR-X dataset. In the TerrraSAR-X descending dataset, on the other hand, the Satkhira Medical College is also visible as a cluster of strong subsidence with line-of-sight displacement velocities of up to -20 mm/year. As mentioned earlier, the lack of data in the decomposed dataset is due to a lack of scatterers in the ascending dataset that meet the coherence threshold of 0.7. A decomposition of line-of-sight measurements into vertical displacements was therefore not possible.

Larger areas of uplift are mainly visible in the TerraSAR-X PSI and the Sentinel-1 SBAS dataset. The Sentinel-1 PSI dataset shows only a few isolated points that are affected by an uplift over the observation period and no large clusters of such points. Within the city, points of uplift tend to be located in the eastern part of the city, where low-density residential areas with a high vegetation component dominate the urban makeup. Most points of strong subsidence are located in densely built-up areas that contain many newly built structures, mostly in the western part of Satkhira. This is true for both the SBAS dataset as well as the TerraSAR-X PSI dataset. In particular, the area south of the Satkhira Government College contains many points with a positive vertical displacement in both these datasets. Outside of the city centre, a large area of uplift is visible in the northeast along the Khulna-Satkhira highway in the TerraSAR-X PSI dataset. In this area, the spatial coverage of both Sentinel-1 datasets is low, which makes a comparison difficult.

In the following, a few points of interest are presented to illustrate the strengths and limitations of both methods (PSI and SBAS) and the different data used (Sentinel-1 and TerraSAR-X). Figure 16 shows the vertical velocity for both Sentinel-1 datasets as well as the line-of-sight velocity for the TerraSAR-X descending dataset over the campus of the Satkhira Medical College, Figure 15 shows the respective displacement time series over the Medical College's main building. In the case of TerraSAR-X the vertical displacement velocity was not available since the campus is not well covered in the TerraSAR-X ascending dataset and not enough points were available for the decomposition of the data. All three datasets show strong negative ground motion over

the campus. Their respective time series (Figure 15) also show an identical negative trend but with different magnitude. The building has subsided by roughly 18 millimetres over the observation period in the SBAS dataset, by roughly 27 millimetres in the TerraSAR-X PSI dataset and by more than 40 millimetres in the Sentinel-1 PSI dataset. The different displacement values for PSI and SBAS could be due to the spatial averaging that is part of the SBAS workflow. The resulting deformation values are mixed signals from a number of adjacent targets, which may lead to an attenuation of strong punctual displacements. The difference between the two PSI datasets is probably in large part due to the different observation periods (S1: January 2017 – December 2019; TSX: November 2017 – November 2019). The Sentinel-1 dataset contains 10 months more displacement.

Figure 17 is a comparison of the three datasets over the city centre of Satkhira. Here the strengths of the PSI algorithm are clearly visible: While SBAS achieves a denser spatial coverage, the PSI results give a much more detailed picture. It is possible to identify individual buildings and on larger buildings and structures, often several points are available, allowing the detection of different displacement rates for different parts of a building. From the PSI data it also becomes clear that the motion patterns within the city centre are much more heterogeneous than suggested by the SBAS data. Between the two PSI datasets however, there are significant differences in spatial coverage. The TerraSAR-X dataset has an extremely high spatial coverage and is much denser than the Sentinel-1 PSI dataset. Figure 17 also illustrates how PSI can be used to detect uncorrelated deformations while SBAS assumes a spatial correlation of the observed deformation phenomena.

Figure 18 shows the northeastern part of Satkhira in the three datasets. This area is rather well covered in the TerraSAR-X dataset but not in both Sentinel-1 datasets. This part of the city is characterised by low-rise residential housing with a high share of vegetation. In general we can observe that TerraSAR-X performs better in these kind of environments and delivers more data than Sentinel-1 (compare also Figure 12 and Figure 13). The reason is probably the higher spatial resolution of TerraSAR-X (~5x5 m^2 for TSX; ~20x20 m^2 for S1). The larger pixels of Sentinel-1 are more likely to contain mixed signals with a contribution from a potentially coherent object (like a building) and a large vegetation contribution and are therefore more strongly affected by decorrelation.

The larger coverage of TerraSAR-X allows us to detect a large-scale uplift in this part of the project area that is not visible in neither of the two Sentinel-1 datasets.

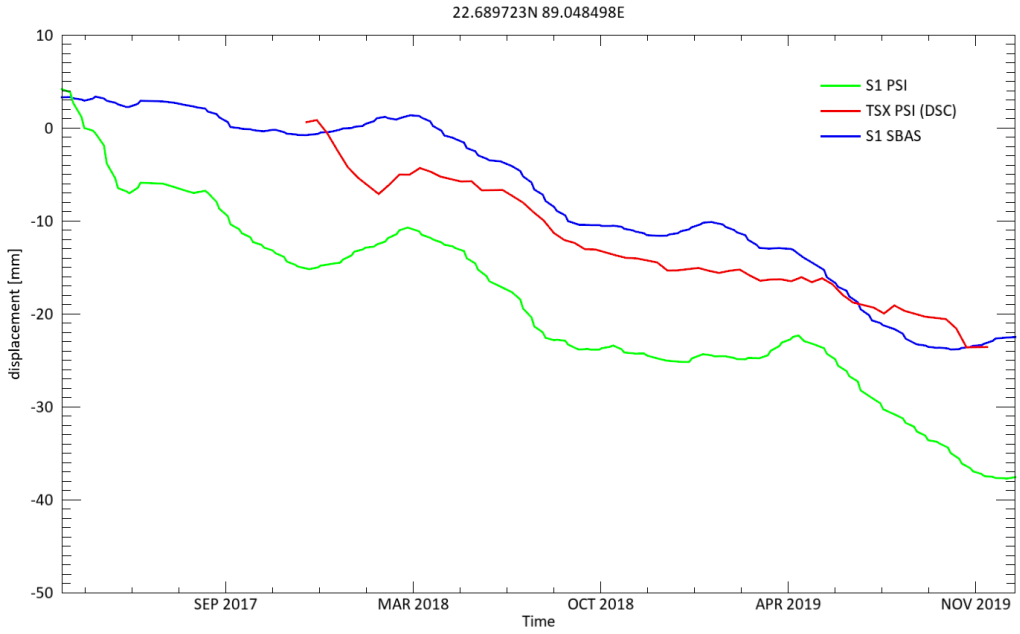

Figure 15: *Deformation time series for Sentinel-1 SBAS and PSI vertical datasets (January 2017 – December 2019) and TerraSAR-X descending dataset (November 2017 – November 2019) over Satkhira Medical College.*

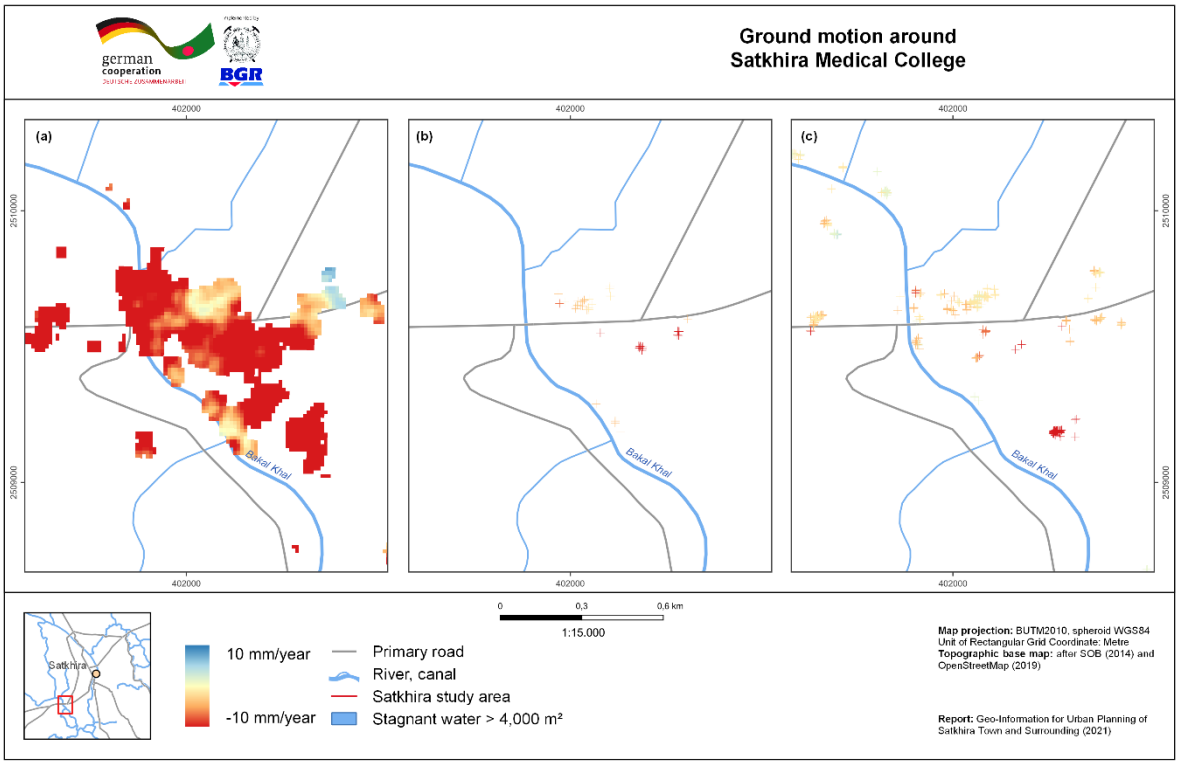

Figure 16: *Satkhira Medical College comparison of a) Sentinel-1 SBAS vertical velocity; b) Sentinel-1 PSI vertical velocity; c) TerraSAR-X PSI line-of-sight (dsc) velocity.*

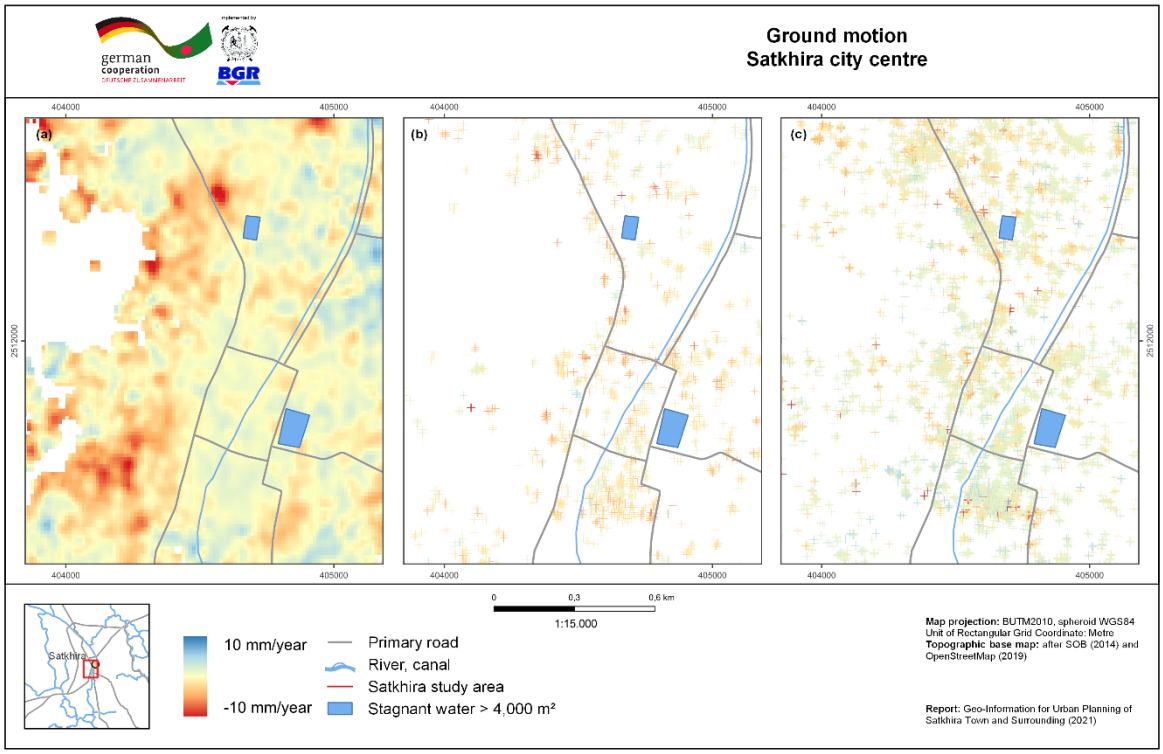

Figure 17: *Satkhira city centre comparison of a) Sentinel-1 SBAS vertical velocity; b) Sentinel-1 PSI vertical velocity; c) TerraSAR-X vertical velocity.*

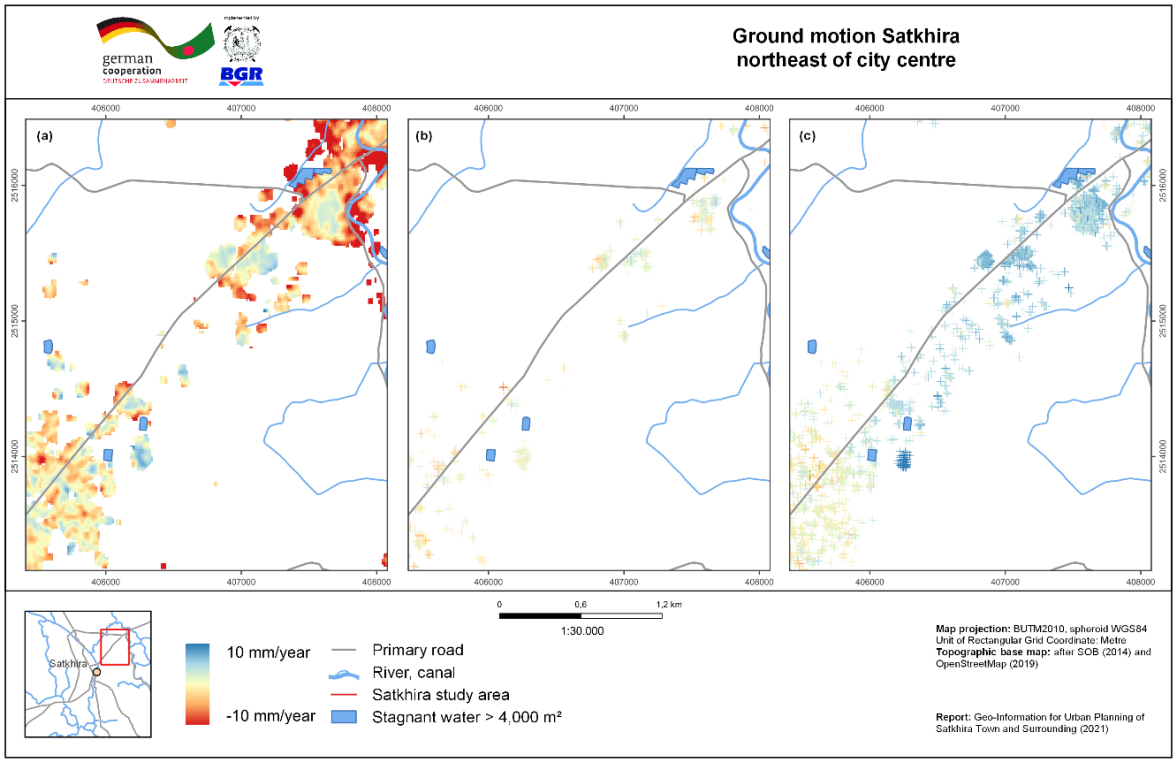

Figure 18: *Satkhira northeast of city centre comparison of a) Sentinel-1 SBAS vertical velocity; b) Sentinel-1 PSI vertical velocity; c) TerraSAR-X PSI vertical velocity.*

2.4.4 Conclusions

Three different ground motion datasets are calculated in the context of this study. A PSI dataset based on Sentinel-1 data, a PSI dataset based on TerraSAR-X data and an SBAS dataset based on Sentinel-1 data. The Satkhira project area with its relatively small urban core, high share of agricultural areas and low-density residential areas is a rather difficult area for ground motion analyses due to the lack of a large number of suitable targets. In spite of these difficulties, both SBAS (Sentinel-1) and PSI using high-resolution radar data (TerraSAR-X) achieve a high spatial coverage. PSI using Sentinel-1 however did not yield satisfactory results. SBAS achieves a higher spatial coverage at the cost of spatial resolution, whereas PSI delivers only punctual information but with high accuracy and spatial resolution. Within the urban core of the project area however, both methods and data sets lead to a similar spatial coverage.

Overall, where data from all three datasets is available the vertical ground motion patterns are similar, which is an indicator to the validity of the results. All three datasets show, that the city centre of Satkhira was mostly stable over the observation period with only isolated points of strong subsidence. Outside of the city centre, the only larger cluster of points of strong subsidence is found on the campus of the Satkhira Medical College. On top of that, from the TerraSAR-X PSI data and the SBAS data, several areas of uplift could be detected.

It is expected that a number of factors contribute to the observed ground motion patterns and trends. Many of the observed subsidence clusters seem to be related to structures that were recently built or recently enlarged. Here, the building load of these structures seems to play a role. From other project areas, it is also known that there is a link between the local geomorphology and ground motion. In particular, it could be shown in other project areas that constructions in floodplains are more likely to be affected by strong subsidence while constructions on natural levees tend to be more stable. The role of changes in groundwater levels and seasonal weather patterns on local ground motion is beyond the scope of this report. A link seems likely but more work needs to be done to confirm this suspicion.

Both methods used (PSI and SBAS) provide huge amounts of measurement points that are spatially and temporarily dense and can be acquired extremely fast and cost-efficiently when compared to other geodetic methods such as levelling or GPS/GNSS (though permanent GPS stations achieve a higher accuracy and temporal density, they provide only punctual measurements).

Both methods work particularly well in urban environments where there is a large amount of high coherent targets, while SBAS also performs well in more suburban or even rural environments. These two facts highlight the immense value of multi-temporal InSAR for urban planning.

Each of the two methods used within this work has its unique strengths and possible areas of application within urban planning. While SBAS enables a denser spatial coverage and the detection of large-scale motion trends related to large infrastructure, PSI enables a more detailed analysis of singular buildings, bridges and roads. On large buildings, we can often find several persistent scatterers, thus PSI can be used to detect different displacement rates for different parts of a building. PSI is also expected to be slightly more accurate than SBAS (PASQUALI ET AL. 2014, p. 236).

Both PSI and SBAS allow the extraction of ground motion information from satellite data with millimetre accuracy and at a high temporal resolution using freely available Sentinel-1 data. Due to the unique characteristics of each method, both methods complement each other well. For absolute ground motion data, external data needs to be used as reference (e.g. GPS/GNSS data from fixed stations).

Regarding the data used, significant differences could be observed between the Sentinel-1 and TerraSAR-X PSI datasets. TerraSAR-X leads to much denser results and a larger spatial coverage both within and outside of the city centre. Particularly striking was the good performance of TerraSAR-X based PSI in rural and suburban areas with a high vegetation component, where both Sentinel-1 datasets show significant gaps. Sentinel-1 was expected to have an advantage in these areas due to its longer wavelength and higher vegetation penetration capabilities. As mentioned previously, the reason is likely the higher spatial coverage of TerraSAR-X over Sentinel-1. This leads to a larger number of targets that tend to be more coherent since their backscatter signals are more likely to be dominated by a single scatterer and less affected by clutter. The different observation periods make direct comparisons of the time series of both datasets difficult.

2.4.5 Recommendations

Multi-temporal InSAR can be used in urban planning to detect stable areas that are potentially suited as building ground. The combined analysis of InSAR and ancillary data (in particular geological, geomorphological, hydrological and land use data) possibly enables the detection of links and causalities for observed ground motion

patterns. Furthermore, multi-temporal InSAR can also serve as a tool for the monitoring of existing infrastructure and buildings.

Two of the most commonly used methods in this field are Persistent Scatterer Interferometry (PSI) and Small Baseline Subset (SBAS). Overall, both methods have their unique strengths and complement each other well. SBAS provides an overview over the large-scale motion patterns within a study area while PSI enables a more detailed analysis of specific points of interest.

A possible constraint to be considered is the computational effort required. While both methods have high computational demands, SBAS is much more computationally intensive for the same data since the number of interferograms created is usually significantly larger than the number of input images. For PSI, the number of interferograms is N-1. Finally, a precondition for the use of any InSAR technique is the existence of enough coherent targets within the area of interest and over the observation period. In areas with seasonal flooding, the use of artificial targets such as corner reflectors or active transponders should be considered.

Where other ground motion data for example from GPS fixed stations or continuous levelling campaigns is available, this data can and should be used as reference for the InSAR results. While different studies have shown that both PSI and SBAS deliver high quality results much depends on the number of acquisitions used. To properly isolate phase influences due to atmosphere and topography from the actual deformation a large number of acqusitions should be used. In general, the more acquisitions are used, the better the results.

The Satkhira project area is a difficult area for ground motion analysis because of the absence in many parts of the project area of coherent targets. While the TerraSAR-X based PSI dataset is dense and covers even the more rural/suburban parts of Satkhira quite well, the Sentinel-1 based PSI dataset is much less dense both in the city centre and in the suburban / rural settlements surrounding the city. The temporal coherence threshold applied to both datasets was set to 0.7, which proved to be too high for the Sentinel-1 dataset. Lowering the coherence threshold will lead to an increase in measurement points (though this will also lead to the inclusion of more measurement points with low quality). When working in areas like Satkhira, with a high degree of agricultural lands and rural settlements, and using medium resolution radar data like Sentinel-1, it could therefore make sense to apply a lower coherence threshold (e.g. 0.6 instead of 0.7).

References

AIRBUS DEFENCE AND SPACE (2015): TerraSAR-X Image Product Guide. <https://www.intelligence-airbusds.com/files/pmedia/public/r459_9_20171004_tsxx-airbusds-ma-0009_tsx-productguide_i2.01.pdf>.

BANGLADESH WATER DEVELOPMENT BOARD (2017): Annual Flood Report 2017. – <http://www.ffwc.gov.bd/images/annual17.pdf>. (Last access: 19.02.2021).

BANGLADESH WATER DEVELOPMENT BOARD (2018): Annual Flood Report 2018. – <http://www.ffwc.gov.bd/images/annual18.pdf>. (Last access: 16.12.2020).

BANGLADESH WATER DEVELOPMENT BOARD (2019): Annual Flood Report 2019. – <http://www.ffwc.gov.bd/images/annual19.pdf>. (Last access: 19.02.2021).

BERARDINO, P., FORNARO, G., LANARI, R., SANSOSTI, E. (2002): A New Algorithm for Surface Deformation Monitoring Based on Small Baseline Differential SAR Interferograms, IEEE Transactions on Geoscience and Remote Sensing, vol. 40, no. 11, pp. 2375- 2383.

CHAMBELL J. B. (1996): Introduction to Remote Sensing. 2nd edition. Taylor & Francis. London.

CHAVEZ, P. S. (1996): Image-Based Atmospheric Corrections - Revisited and Improved. Photogrammetric Engineering and Remote Sensing. Vol. 62. No. 9. 1025-1036.

CONGEDO, L. (2016): Semi-Automatic Classification Plugin Documentation. – <http://dx.doi.org/10.13140/RG.2.2.29474.02242/1>. (Last change: n.d.). (Last access: 08.08.2019).

CROSETTO, M., MONSERRAT, O., CUEVAS-GONZÁLEZ, M., DEVANTHÉRY, N., CRIPPA, B. (2016): Persistent Scatterer Interferometry: A review, ISPRS Journal of Photogrammetry and Remote Sensing, vol. 115, pp. 78-89.

EUROPEAN ENVIRONMENT AGENCY (2017): Copernicus Land Service – Pan-European Component: CORINE Land Cover. <https://land.copernicus.eu/user-corner/publications/clc-flyer/at_download/file>. (Last change: n.d.). (Last access: 22.01.2021).

EUROPEAN ENVIRONMENT AGENCY (2019): Updated CLC illustrated nomenclature guidelines. - <https://land.copernicus.eu/user-corner/technical-library/corine-land-cover-nomenclature-guidelines/docs/pdf/CLC2018_Nomenclature_illustrated_guide_20190510.pdf>. (Last change: n.d.). (Last access: 22.01.2021).

EUROPEAN SPACE AGENCY (2017): Sentinel-2 Spectral Response Functions (S2-SRF). – <https://earth.esa.int/web/sentinel/user-guides/sentinel-2-msi/document-library/-/asset_publisher/Wk0TKajiISaR/content/sentinel-2a-spectral-responses>. (Last change: 19.12.2017). (Last access: 13.06.2019).

EUROPEAN SPACE AGENCY (2019): Sen2Cor Configuration and User Manual V2.8. – <http://step.esa.int/thirdparties/sen2cor/2.8.0/docs/S2-PDGS-MPC-L2A-SUM-V2.8.pdf>. (Last change: 05.02.2019). (Last access: 22.08.2019).

EUROPEAN SPACE AGENCY (2020): Sentinel-1 User Guide: Interferometric Wide Swath. <https://sentinel.esa.int/web/sentinel/user-guides/sentinel-1-sar/acquisition-modes/interferometric-wide-swath>. (Last change: n.d.). (Last access: 16.12.2020).

FERRETTI, A., PRATI, C., ROCCA, F. (2001): Permanent Scatterers in SAR Interferometry, IEEE Transactions on Geoscience and Remote Sensing, vol. 39, no. 1, pp. 8-20.

FENTON, A., PAAVOLA, J., TALLONTIRE, A. (2017): Autonomous adaption of riverine flooding in Satkhira District, Bangladesh: implications for adapting planning. Regional Environmental Change 17, 2387-2396 (2017). https://doi.org/10.1007/s10113-017-1159-8

FORNARO, G., PASCAZIO, V. (2014): Chapter 20 - SAR Interferometry and Tomography: Theory and Applications. Academic Press Library in Signal Processing. Vol. 2. 1043-1117. doi: 10.1016/B978-0-12-396500-4.00020-X.

GOOGLE EARTH ENGINE DATA CATALOG (2020): Sentinel-1 SAR GRD: C-band Synthetic Aperture Radar Ground Range Detected, log scaling. – <https://developers.google.com/earth-engine/datasets/catalog/COPERNICUS_S1_GRD>. (Last change: n.d.). (Last Access: 16.12.2020).

JONES, H. G. AND VAUGHAN, R. A. (2010): Remote Sensing of Vegetation – Principles, Techniques, and Applications. Oxford University Press.

KALIA, A., C., FREI, M., LEGE, T., (2020): BodenBewegungsdienst Deutschland - BBD, Projektbericht, Version 1, 133 S., Bundesanstalt für Geowissenschaften und Rohstoffe (BGR), Hannover, unpublished.

LILLESAND, T. M., KIEFER, W., CHIPMAN, J. W. (2015): Remote Sensing and Image Interpretation. Seventh Edition. Wiley.

LÓPEZ-MARTÍNEZ, C., FÀBREGAS, X. AND POTTIER, E. (2004): A new alternative for SAR imagery coherence estimation. Proc. EUSAR Conf., Ulm, Germany.

McFeeters, S. K. (1996): The use of the Normalized Difference Water Index (NDWI) in the delineation of open water features. International Journal of Remote Sensing. Vol. 17. No. 7. 1425-1432.

Moreira, A., Prats-Iraola, P., Younis, M., Krieger, G., Hajnsek, I., and Papathanassiou, K. P. (2013): A tutorial on synthetic aperture radar. In: IEEE Geoscience and Remote Sensing Magazine. Vol. 1, No. 1. 6-43. doi: 10.1109/MGRS.2013.2248301.

Mueller-Wilm, U., Devignot, O., Pessiot, L. (2018): Level 2A Input Output Data Definition (IODD) v2.5.5. – <https://step.esa.int/thirdparties/sen2cor/2.5.5/docs/S2-PDGS-MPC-L2A-IODD-V2.5.5.pdf>. (Last change: 23.03.2018) (Last access: 20.05.2019).

Pasquali, P., Cantone, A., Riccardi, P., Defilippi, M., Ogushi, F., Gagliano, S. and Tamura, M. (2014): Mapping of Ground Deformations with Interferometric Stacking Techniques, in Land Applications of Radar Remote Sensing, InTech.

Prasad S., Bruce L. M., Chanussot J. (2011): Introduction. Optical Remote Sensing. Augmented Vision and Reality, Vol. 3. Springer. Berlin, Heidelberg.

Rencz A. N. (1999): Manual of Remote Sensing. 3rd edition, Vol. 3. Remote Sensing for the Earth Sciences. John Wiley & Sons.

Richards, J. A. (2009): Remote Sensing with Imaging Radar. Springer-Verlag. Berlin, Heidelberg.

Richards, J. A. (2013): Remote Sensing Digital Image Analysis – An Introduction. 5th edition. Springer. Heidelberg. New York. Dordrecht. London.

Sabins F. F. (1996): Remote Sensing. 3rd edition. Freemann and Company. New York.

United States Geological Survey (n.d.): What are the band designations for the Landsat satellites? – <https://www.usgs.gov/faqs/what-are-band-designations-landsat-satellites>. (Last change: n.d.). (Last access: 13.06.2019).

United States Geological Survey (2020): Landsat 4-7 Surface Reflectance (LEDAPS) Product Guide. Version 3.0. August 2020. – <https://prd-wret.s3.us-west-2.amazonaws.com/assets/palladium/production/atoms/files/LSDS-1370_L4-7_C1-SurfaceReflectance-LEDAPS_ProductGuide-v3.pdf>. (Last change: August 2020). (Last access: 02.11.2020).

Ustin S. L. (2004): Manual of Remote Sensing. 3rd edition, Vol. 4. Remote Sensing for Natural Resource Management and Environmental Monitoring. John Wiley & Sons.

WOODHOUSE, I. H. (2006): Introduction to Microwave Remote Sensing. 1st edition. CRC Press. Boca Raton.

Annexure A: Maps

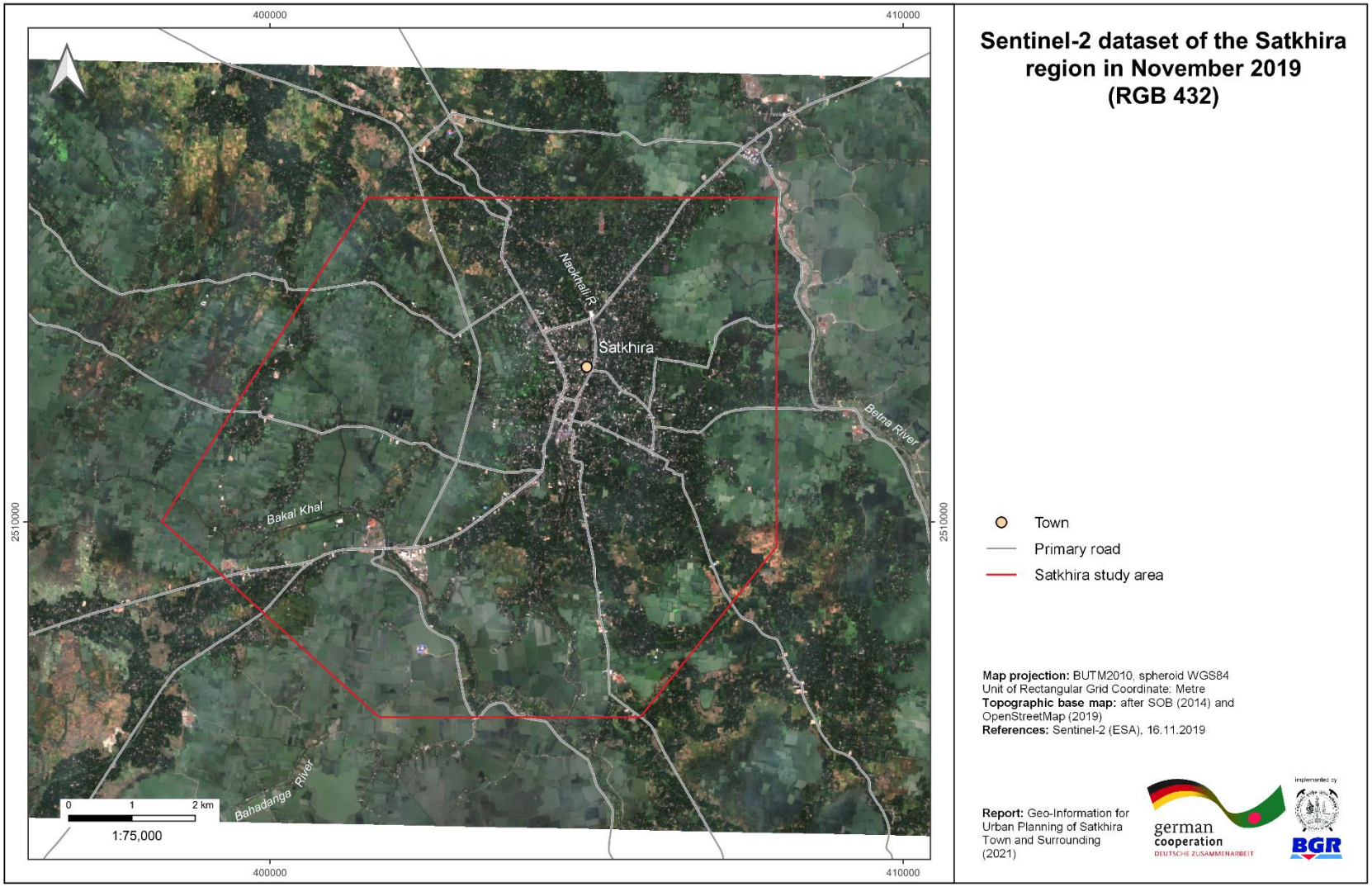

Figure A1: *Sentinel-2 Dataset of the Satkhira Region, 16.11.2019 (RGB 4-3-2).*

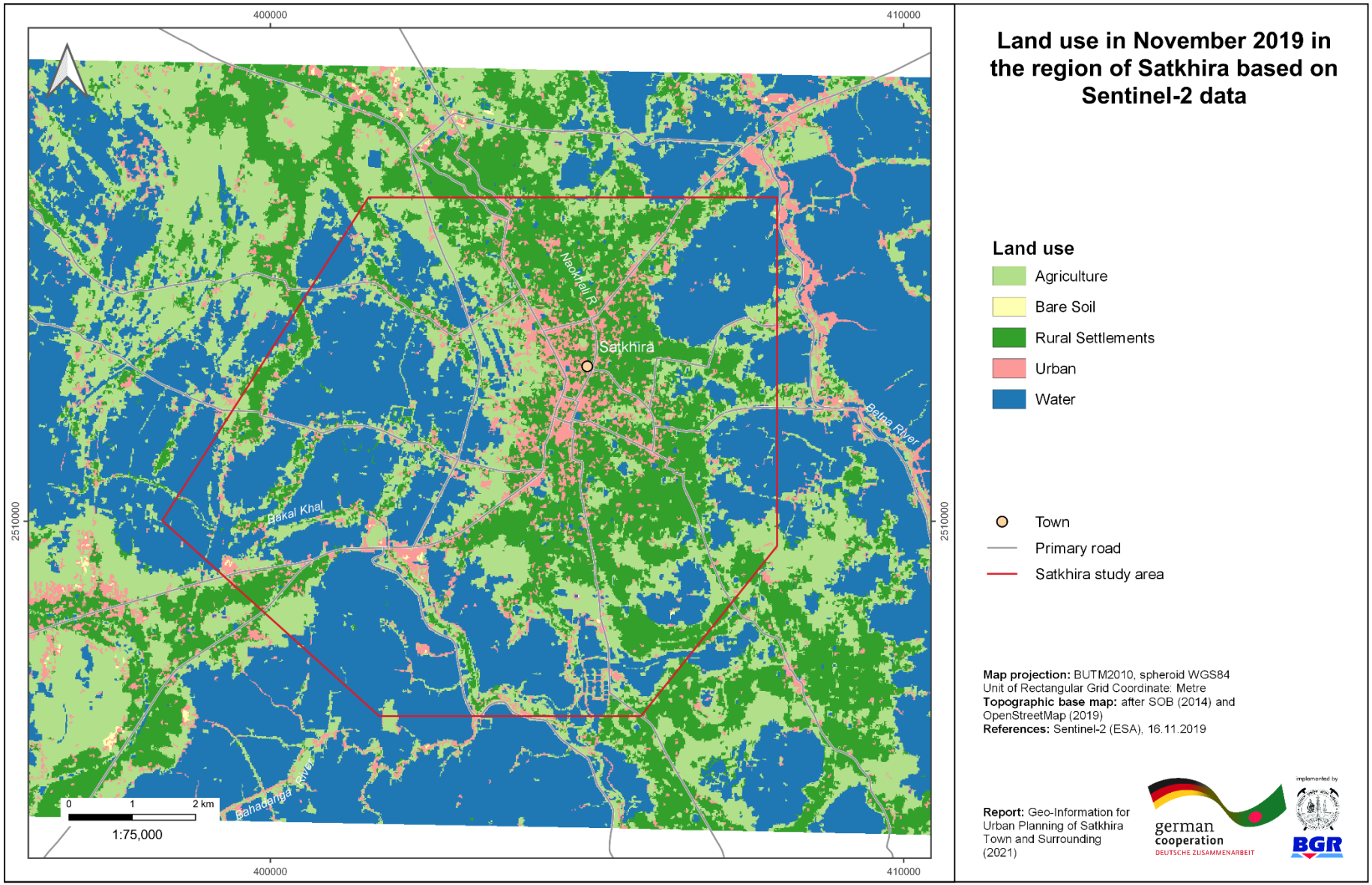

Figure A2: *Land use in November 2019 in region of Satkhira based on Sentinel-2 data.*

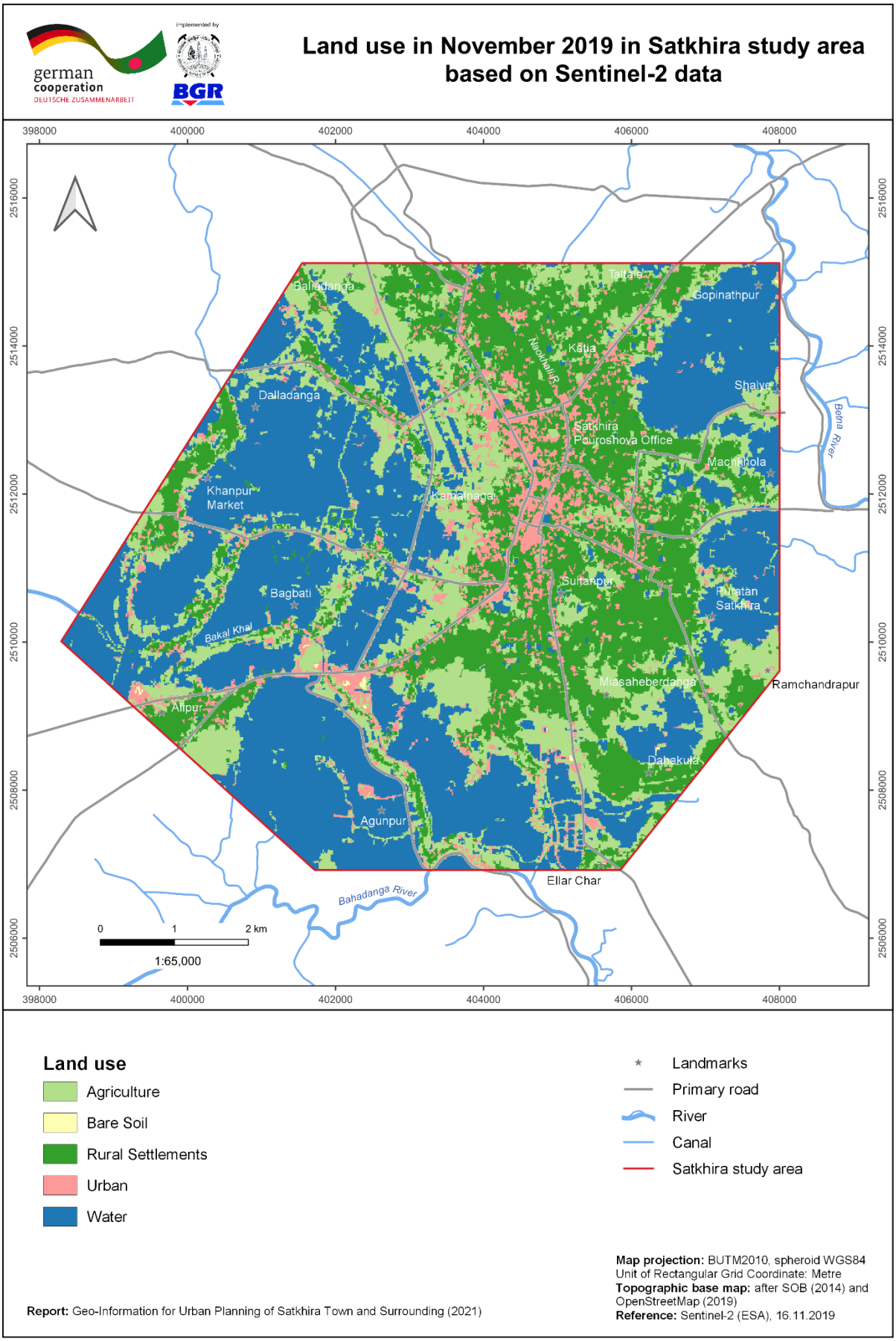

Figure A3: *Land use in November 2019 in Satkhira study area based on Sentinel-2 data.*

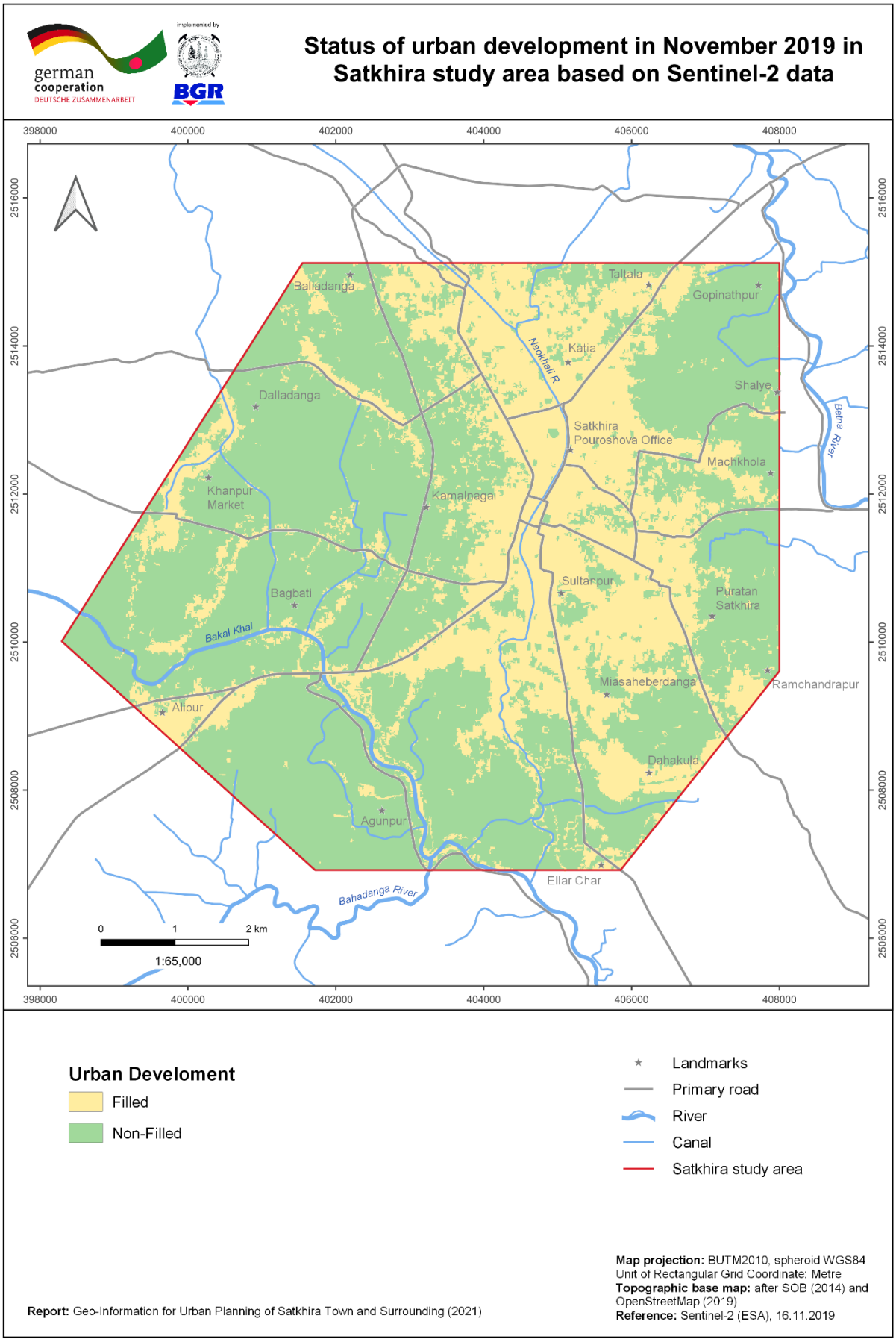

Figure A4: *Status of urban development in November 2019 in Satkhira study area based on Sentinel-2 data.*

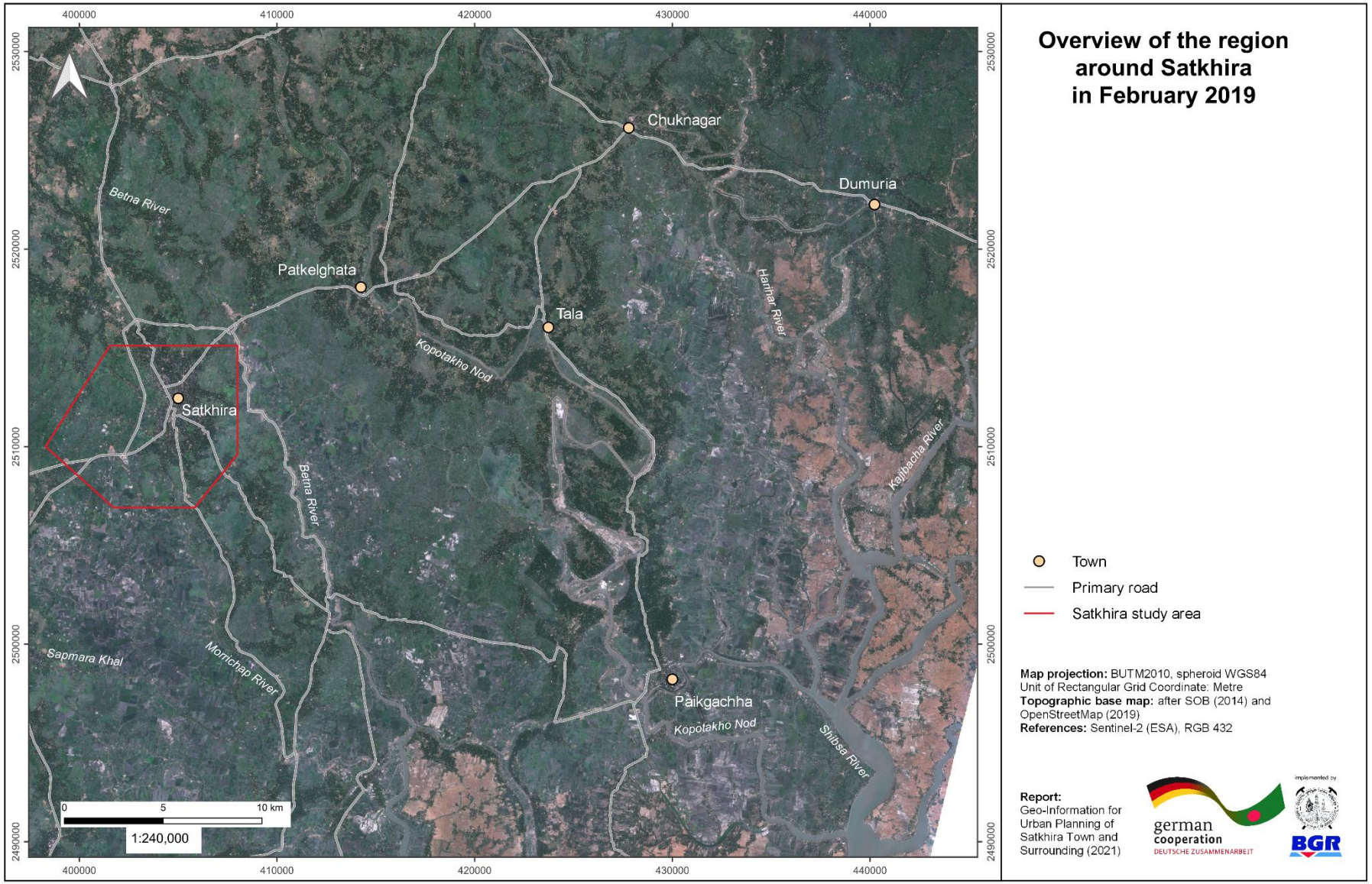

Figure A5: *Overview of the region around Satkhira (Sentinel-2, RGB 432, 14.02.2019).*

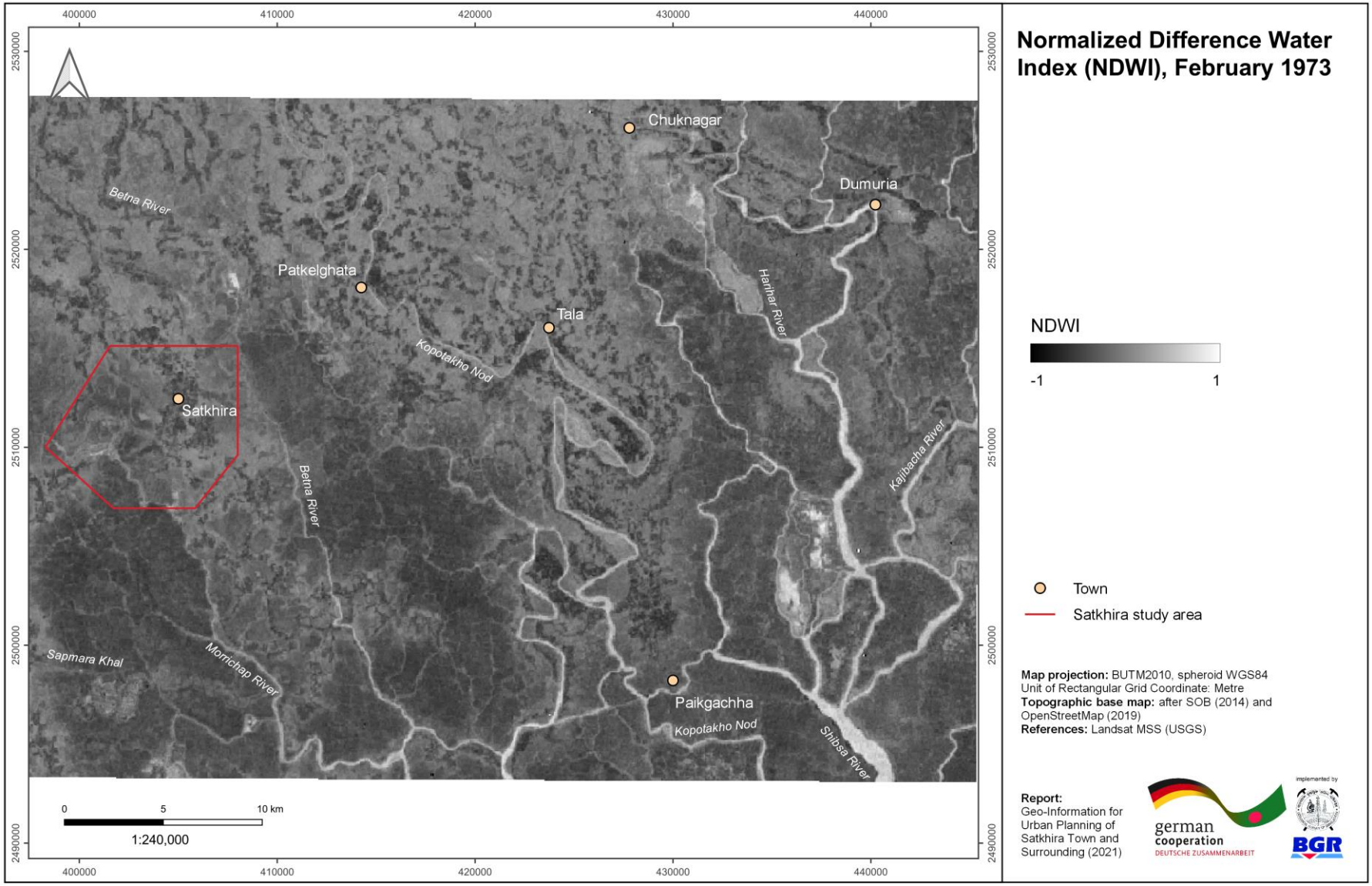

Figure A6: *Normalized Difference Water Index (NDWI), based on Landsat MSS imagery (21.02.1973).*

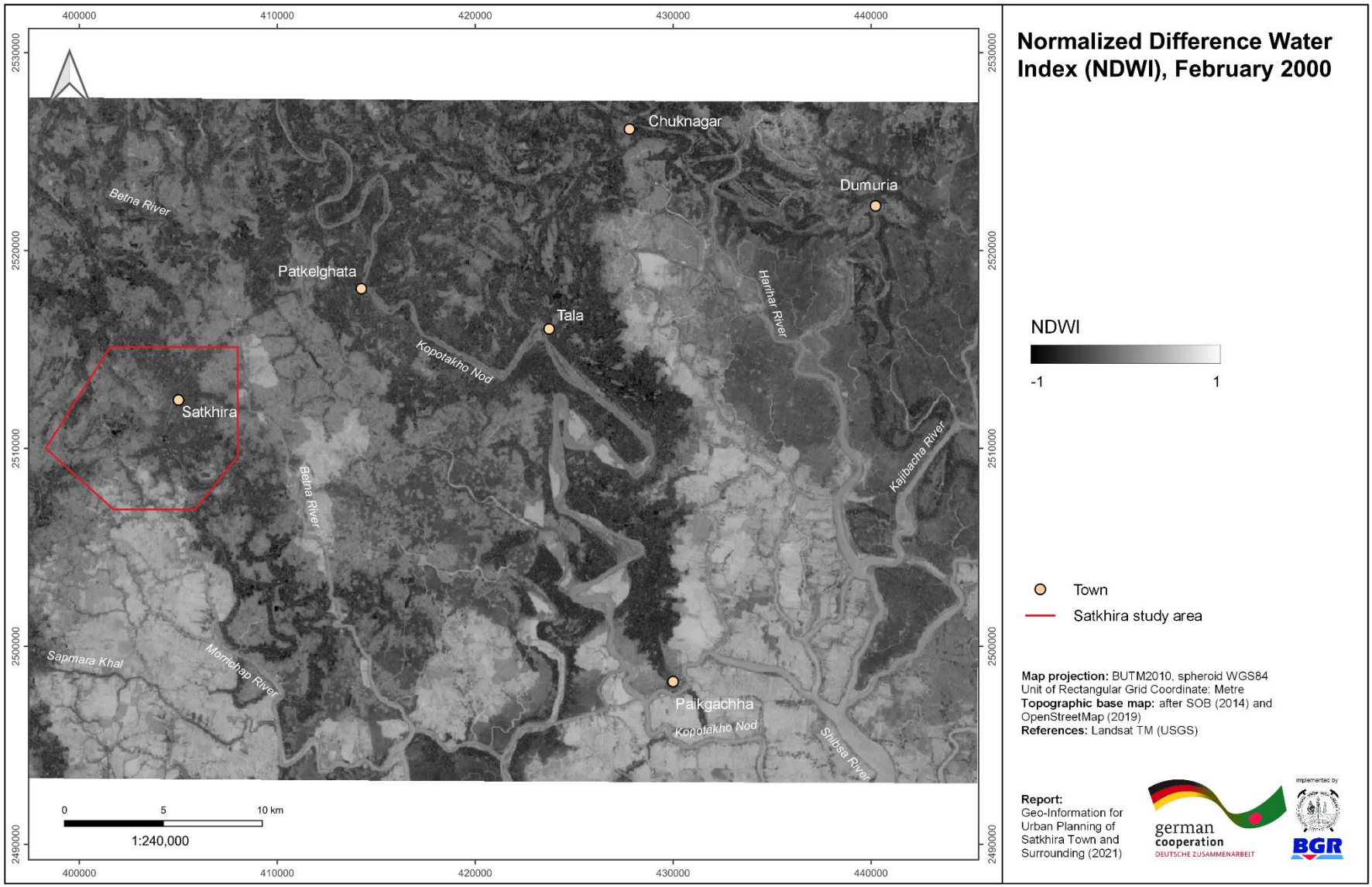

Figure A7: *Normalized Difference Water Index (NDWI), based on Landsat TM imagery (11.02.2000).*

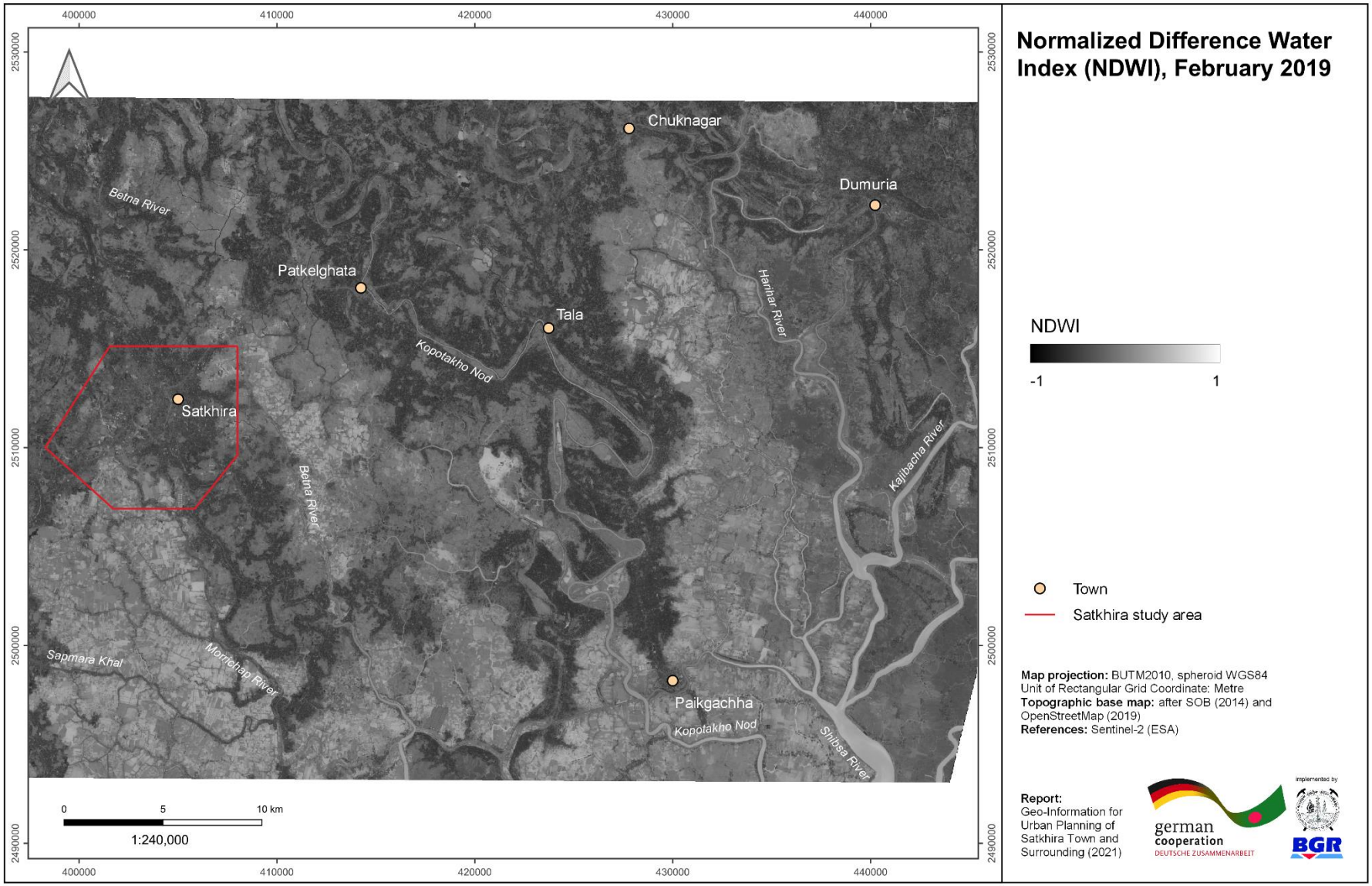

Figure A8: *Normalized Difference Water Index (NDWI), based on Sentinel-2 imagery (14.02.2019).*

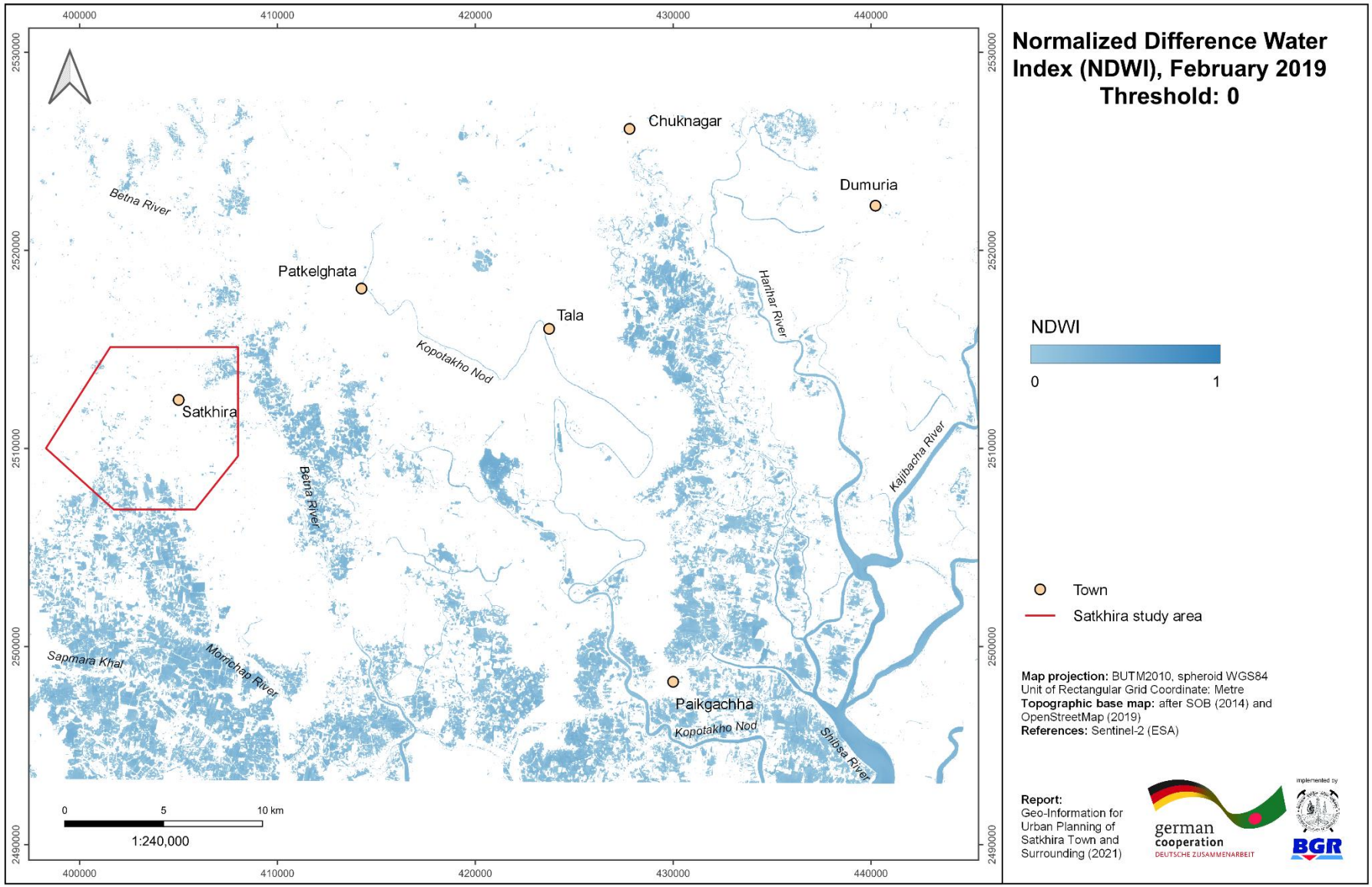

Figure A9: *Normalized Difference Water Index (NDWI), based on Sentinel-2 imagery (14.02.2019), threshold of 0.*

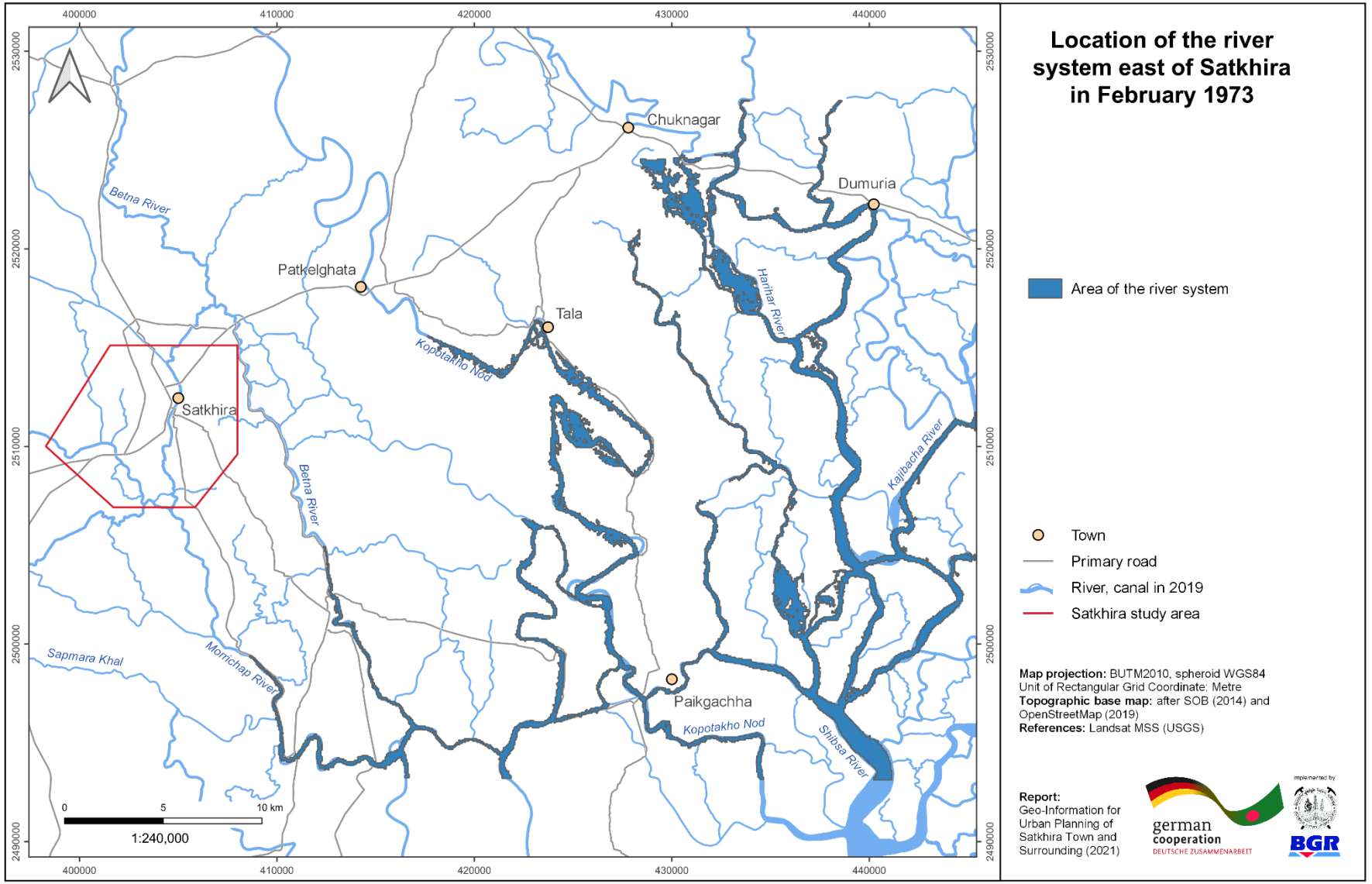

Figure A10: *Location of the river system east of Satkhira based on NDWI from 1973.*

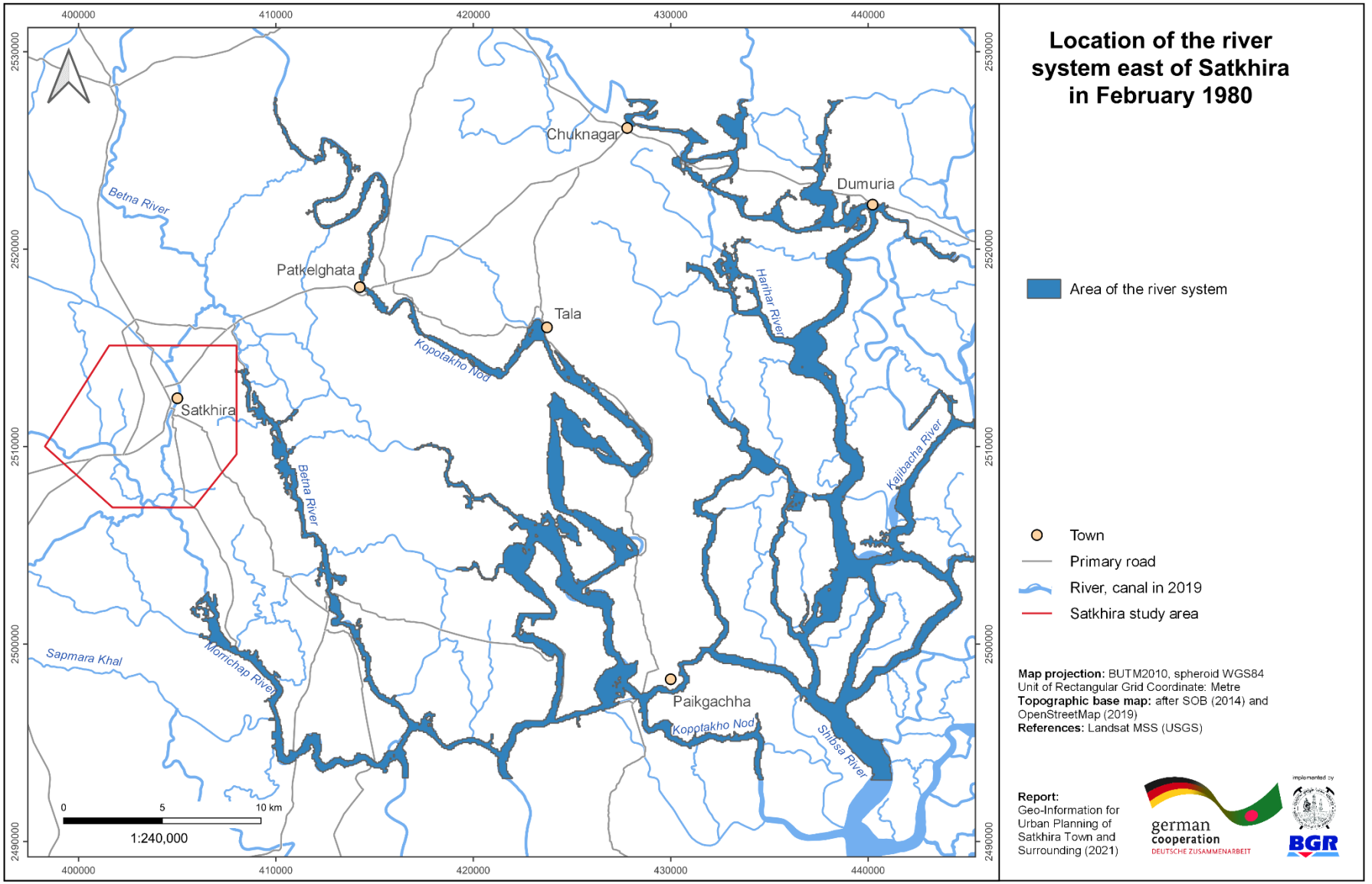

Figure A11: *Location of the river system east of Satkhira based on NDWI from 1980.*

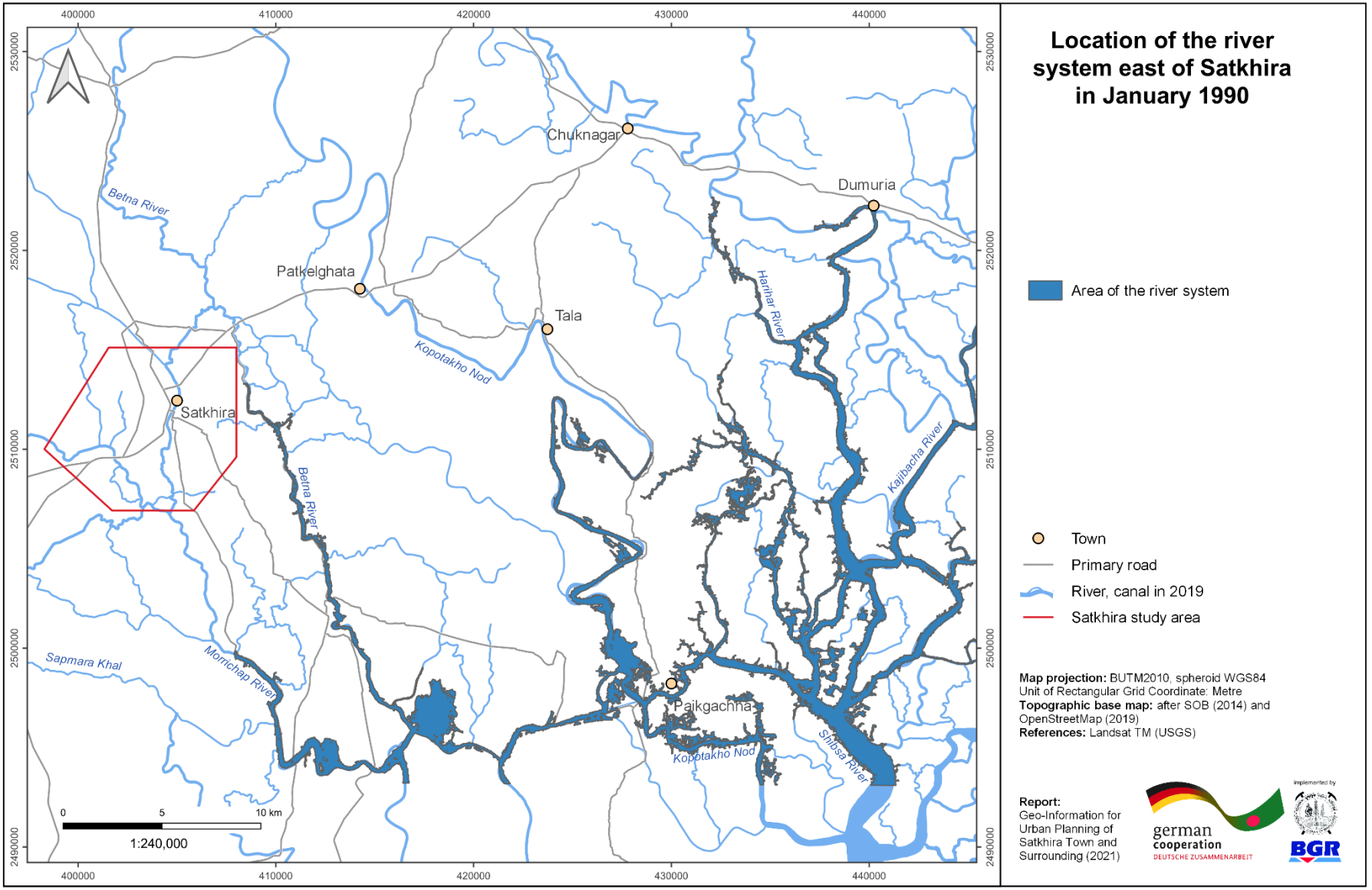

Figure A12: *Location of the river system east of Satkhira based on NDWI from 1990.*

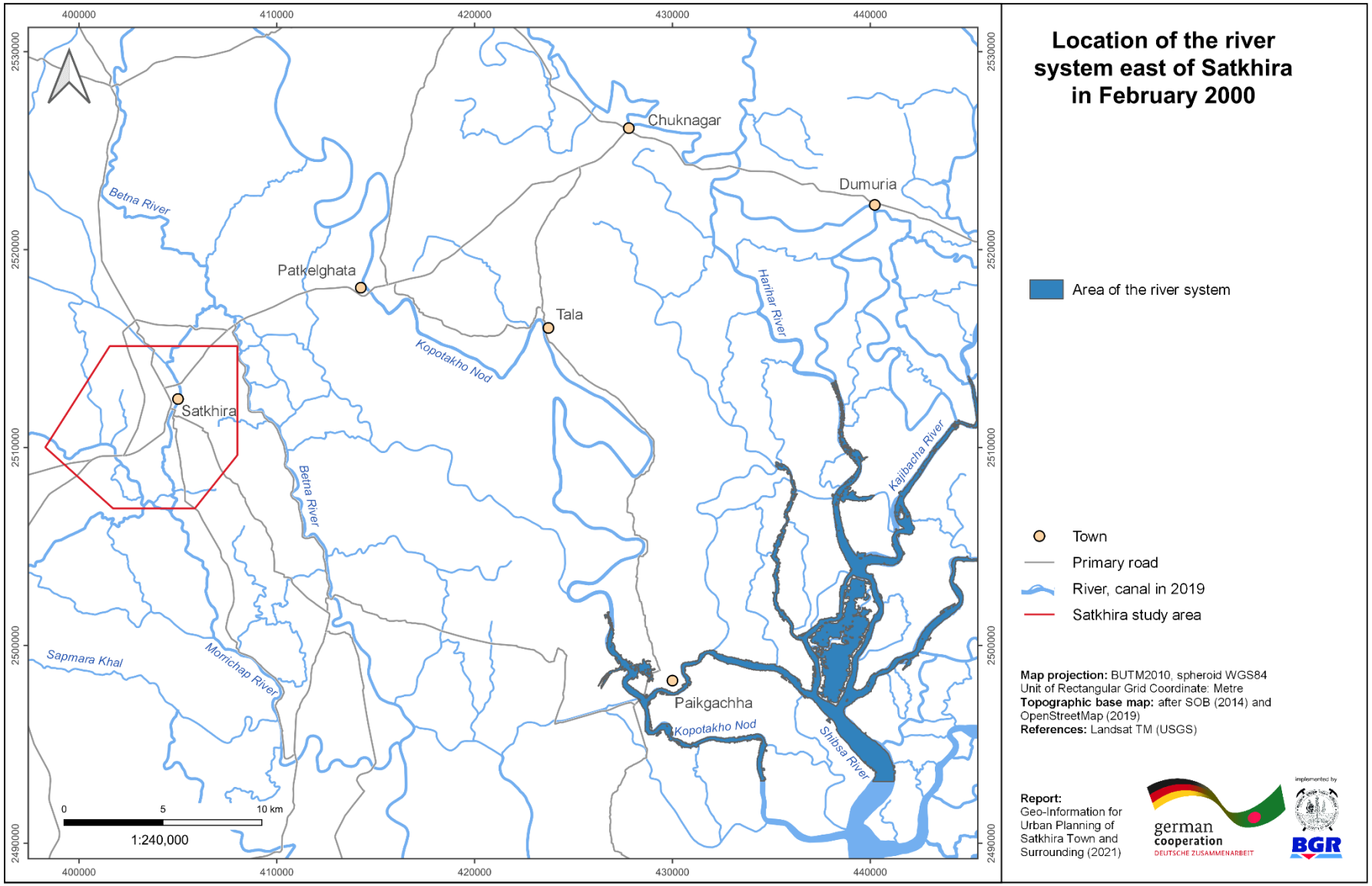

Figure A13: *Location of the river system east of Satkhira based on NDWI from 2000.*

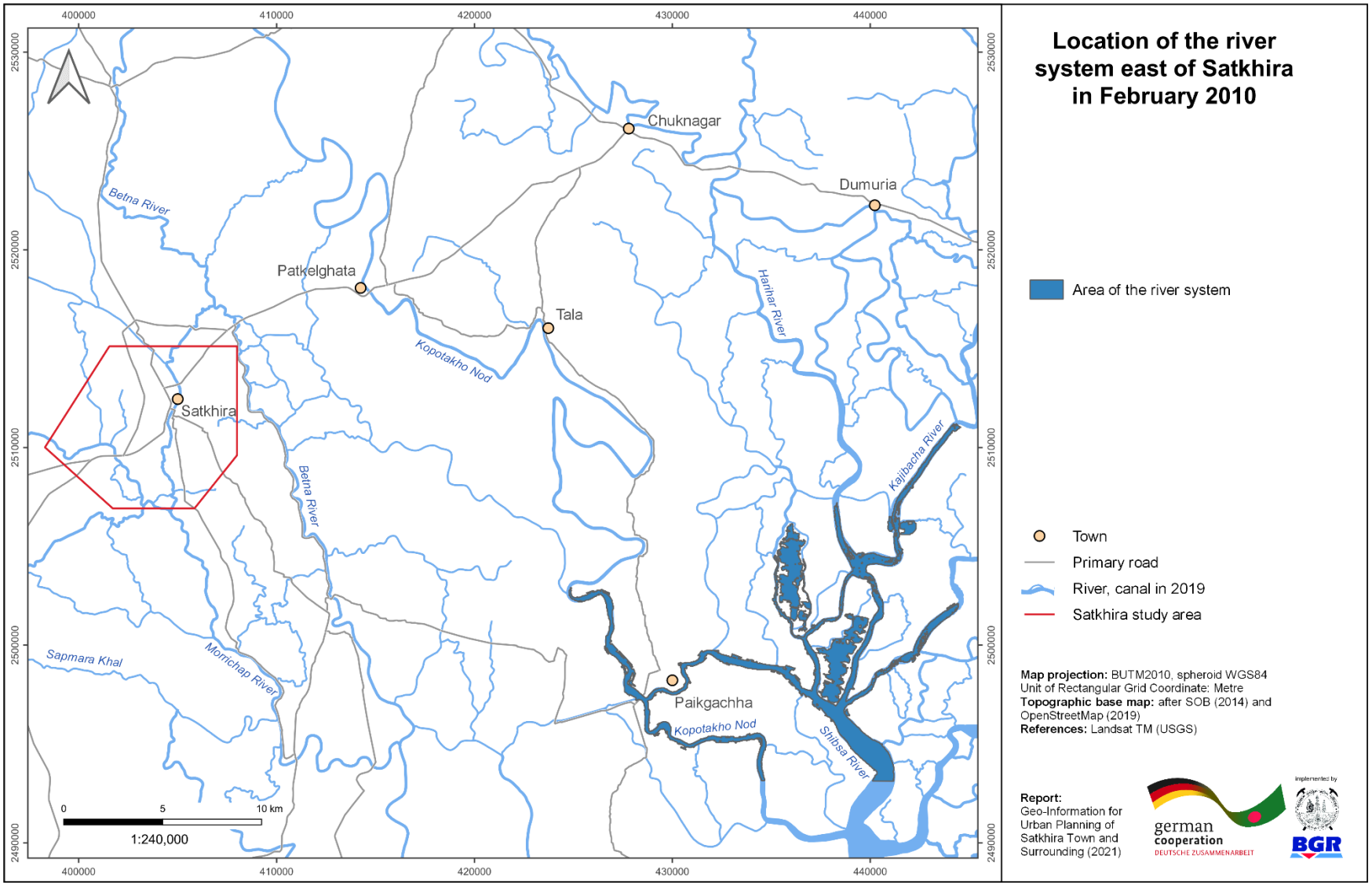

Figure A14: *Location of the river system east of Satkhira based on NDWI from 2010.*

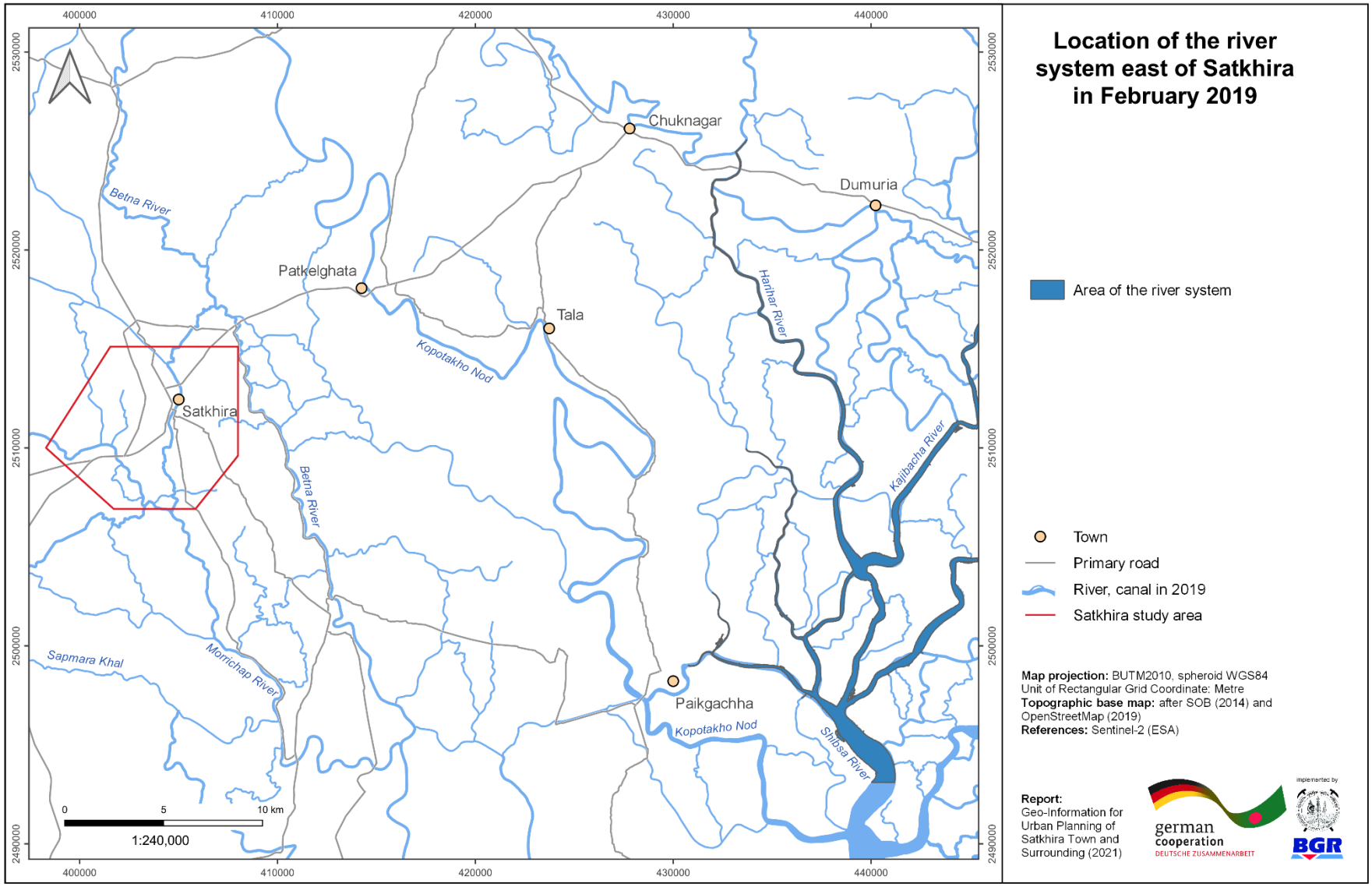

Figure A15: *Location of the river system east of Satkhira based on NDWI from 2019.*

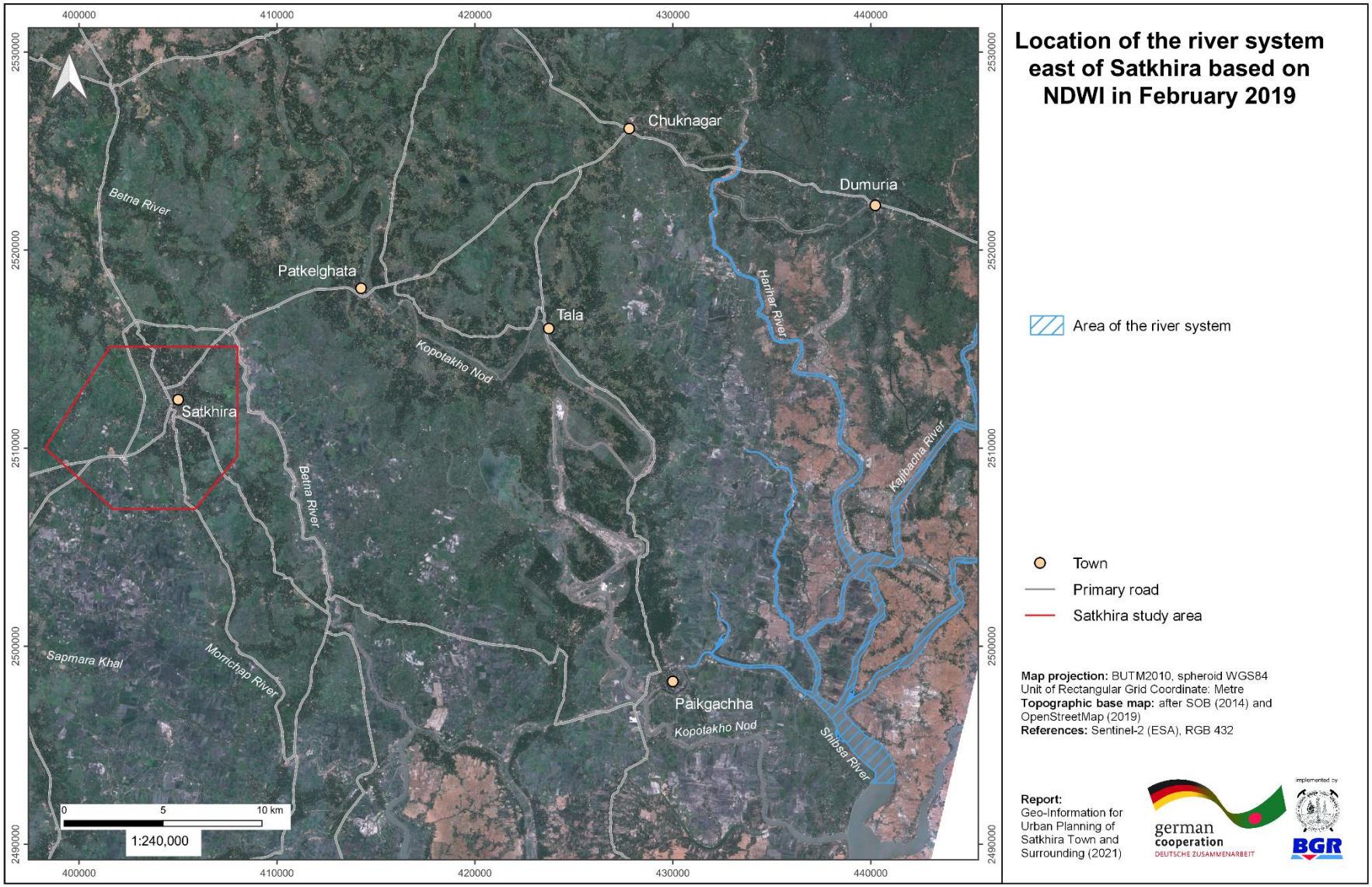

Figure A16: *Location of the river system east of Satkhira based on NDWI from 2019.*

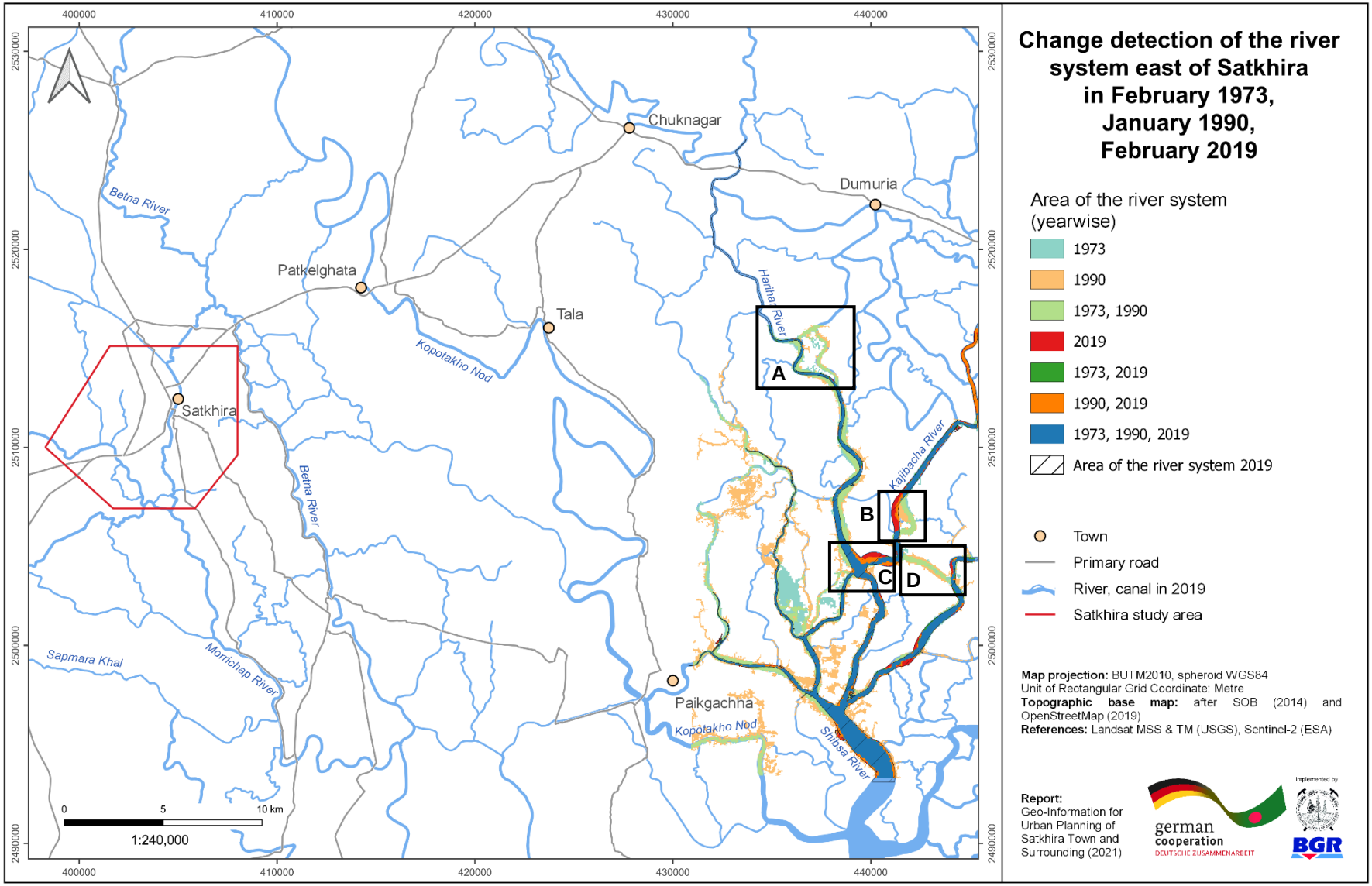

Figure A17: *Change Detection of the river system east of Satkhira of February 1973, January 1990 and February 2019.*

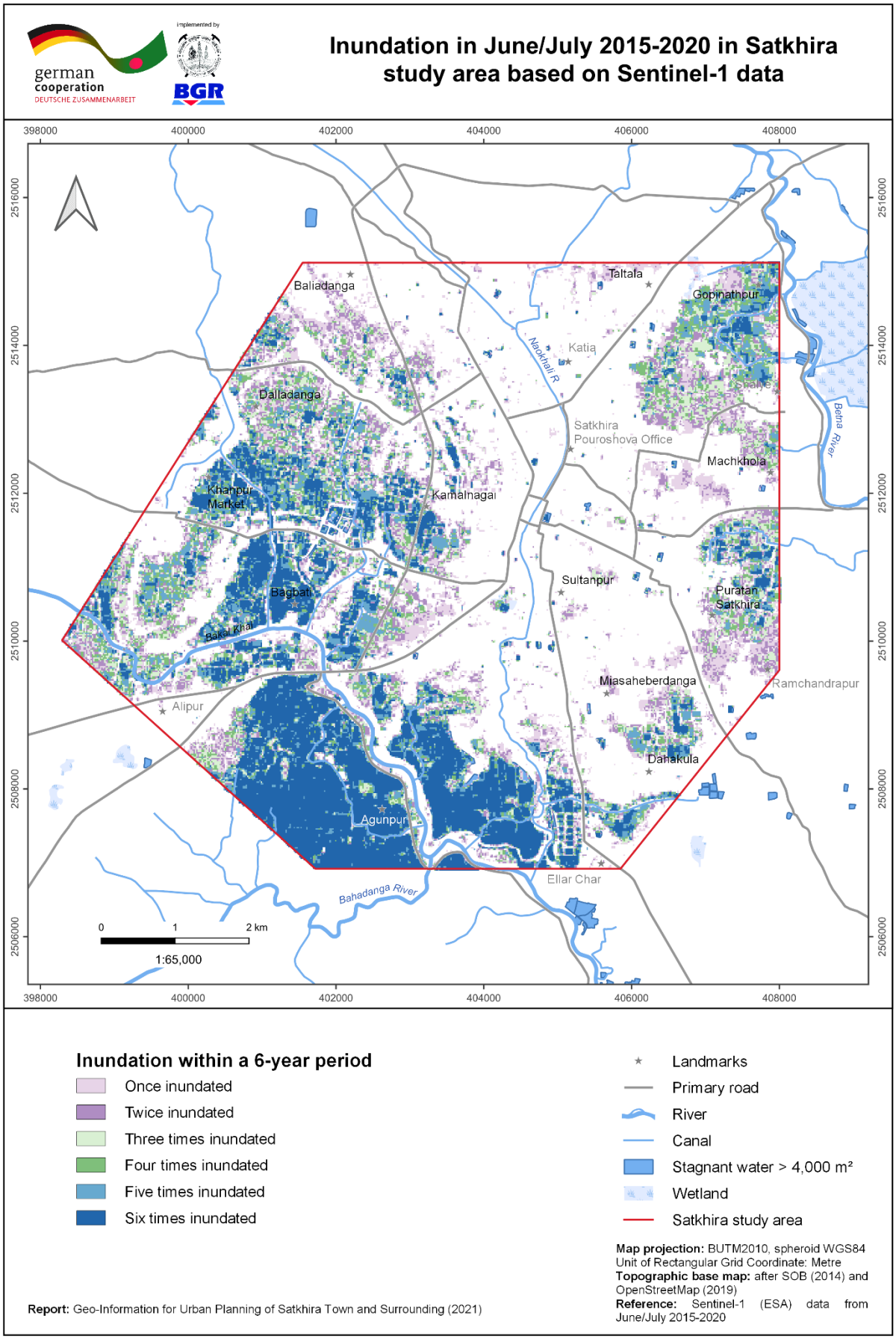

Figure A18: *Inundation in June/July 2015-2020 in Satkhira study area..*

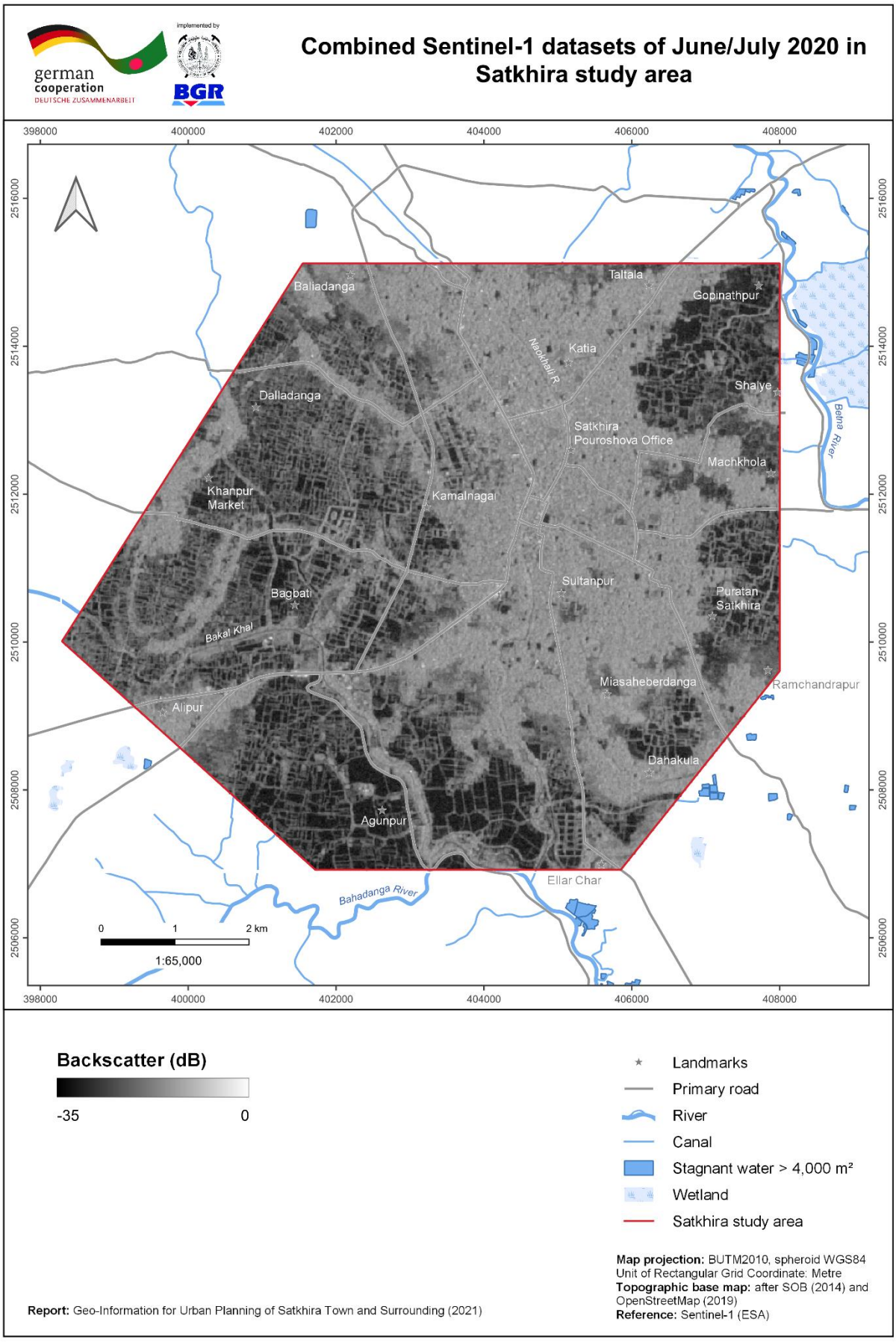

Figure A19: *Combined Sentinel-1 image of June/July 2020 in Satkhira study area.*

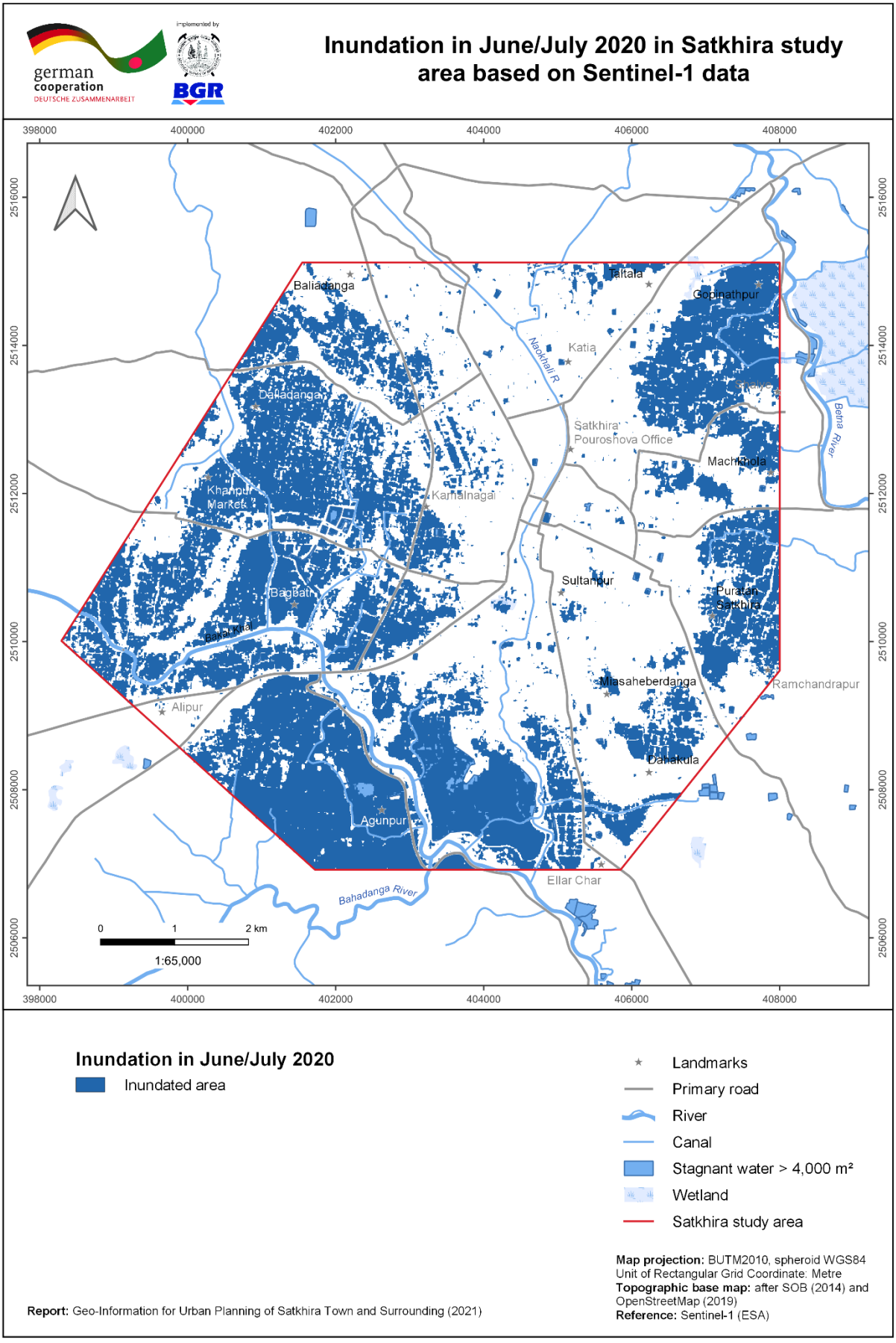

Figure A20: *Inundation in June/July 2020 in Satkhira study area.*

Annexure B: Google Earth Engine Code

```
// Select Area of Interest (pa = uploaded SHP of Satkhira study area)
pa = pa.geometry();
// Center the map with focus on the study area
Map.centerObject(pa);


// 2015
// Define start and end date of the study period
var start_wet = '2015-06-01';
var end_wet = '2015-07-31';

// Load the Sentinel-1 image collection
var S1_wet15 = ee.ImageCollection('COPERNICUS/S1_GRD')
// Filter: Return only Vertical-Horizontal (VH) polarization images
.filter(ee.Filter.listContains('transmitterReceiverPolarisation', 'VH'))
// Filter: Return only images with the main acquisition mode IW
.filter(ee.Filter.eq('instrumentMode', 'IW'))
// Filter: Return only descending orbit images
.filter(ee.Filter.eq('orbitProperties_pass', 'DESCENDING'))
// Filter: Return only images with a 10 m resolution
.filterMetadata('resolution_meters','equals',10)
// Filter: Return only images within the study period
.filterDate(start_wet, end_wet)
// Filter: Return only images within the study area
.filterBounds(pa)
// Calculate the mean of all remaining images
.reduce(ee.Reducer.mean())
// Clip the mean-image to the study area
.clip(pa);
// Print the image information to the console
print(S1_wet15)


// 2016
var start_wet = '2016-06-01';
var end_wet = '2016-07-31';

var S1_wet16 = ee.ImageCollection('COPERNICUS/S1_GRD')
.filter(ee.Filter.listContains('transmitterReceiverPolarisation', 'VH'))
```

```
.filter(ee.Filter.eq('instrumentMode', 'IW'))
.filter(ee.Filter.eq('orbitProperties_pass', 'DESCENDING'))
.filterMetadata('resolution_meters','equals',10)
.filterDate(start_wet, end_wet)
.filterBounds(pa)
.reduce(ee.Reducer.mean())
.clip(pa);
print(S1_wet16)

// 2017
var start_wet = '2017-06-01';
var end_wet = '2017-07-31';

var S1_wet17 = ee.ImageCollection('COPERNICUS/S1_GRD')
.filter(ee.Filter.listContains('transmitterReceiverPolarisation', 'VH'))
.filter(ee.Filter.eq('instrumentMode', 'IW'))
.filter(ee.Filter.eq('orbitProperties_pass', 'DESCENDING'))
.filterMetadata('resolution_meters','equals',10)
.filterDate(start_wet, end_wet)
.filterBounds(pa)
.reduce(ee.Reducer.mean())
.clip(pa);
print(S1_wet17)

//2018
var start_wet = '2018-06-01';
var end_wet = '2018-07-31';

var S1_wet18 = ee.ImageCollection('COPERNICUS/S1_GRD')
.filter(ee.Filter.listContains('transmitterReceiverPolarisation', 'VH'))
.filter(ee.Filter.eq('instrumentMode', 'IW'))
.filter(ee.Filter.eq('orbitProperties_pass', 'DESCENDING'))
.filterMetadata('resolution_meters','equals',10)
.filterDate(start_wet, end_wet)
.filterBounds(pa)
.reduce(ee.Reducer.mean())
.clip(pa);
print(S1_wet18)

//2019
var start_wet = '2019-06-01';
var end_wet = '2019-07-31';
```

```
82
83  var S1_wet19 = ee.ImageCollection('COPERNICUS/S1_GRD')
84  .filter(ee.Filter.listContains('transmitterReceiverPolarisation', 'VH'))
85  .filter(ee.Filter.eq('instrumentMode', 'IW'))
86  .filter(ee.Filter.eq('orbitProperties_pass', 'DESCENDING'))
87  .filterMetadata('resolution_meters','equals',10)
88  .filterDate(start_wet, end_wet)
89  .filterBounds(pa)
90  .reduce(ee.Reducer.mean())
91  .clip(pa);
92  print(S1_wet19)
93
94  //2020
95  var start_wet = '2020-06-01';
96  var end_wet = '2020-07-31';
97
98  var S1_wet20 = ee.ImageCollection('COPERNICUS/S1_GRD')
99  .filter(ee.Filter.listContains('transmitterReceiverPolarisation', 'VH'))
100 .filter(ee.Filter.eq('instrumentMode', 'IW'))
101 .filter(ee.Filter.eq('orbitProperties_pass', 'DESCENDING'))
102 .filterMetadata('resolution_meters','equals',10)
103 .filterDate(start_wet, end_wet)
104 .filterBounds(pa)
105 .reduce(ee.Reducer.mean())
106 .clip(pa);
107 print(S1_wet20)
108
109 // Set threshold to distinguish between water and non-water
110 var threshold = -20
111
112 // Filter every image collection to the defined threshold
113 var S1_wet_threshold15 = S1_wet15.select('VH_mean').lt(threshold);
114 var S1_wet_threshold16 = S1_wet16.select('VH_mean').lt(threshold);
115 var S1_wet_threshold17 = S1_wet17.select('VH_mean').lt(threshold);
116 var S1_wet_threshold18 = S1_wet18.select('VH_mean').lt(threshold);
117 var S1_wet_threshold19 = S1_wet19.select('VH_mean').lt(threshold);
118 var S1_wet_threshold20 = S1_wet20.select('VH_mean').lt(threshold);
119
120 // Combining all images to get one image with six classes
121 var final_img =
122 S1_wet_threshold15.add(S1_wet_threshold16).add(S1_wet_threshold17).add(S1_w
123 et_threshold18).add(S1_wet_threshold19).add(S1_wet_threshold20);
```

```
// Visualize the final result
Map.addLayer(final.updateMask(final_img),{palette:"0000FF"},'Water
extent',1);

// Export the image to the Drive
Export.image.toDrive({
// Definition of the image
  image: final_img,
// Description
  description: 'Satkhira_Inun_Map',
// Resolution in meter
  scale: 20,
// Study area
  region: pa,
// Format of the raster
  fileFormat: 'GeoTIFF'
});

Export.image.toDrive({
  image: S1_wet20.select("VH_mean"),
  description: 'Satkhira_2020_image',
  scale: 10,
  region: pa,
  fileFormat: 'GeoTIFF'
});

Export.image.toDrive({
  image: S1_wet_threshold20,
  description: 'Satkhira_2020_inundation',
  scale: 10,
  region: pa,
  fileFormat: 'GeoTIFF'
});
```

Annexure C: Data

Optical satellite images

Landsat naming convention

Image name: LXSS_LLLL_PPPRRR_YYYYMMDD_yyyymmdd_CC_TX

Group	**Meaning**		
LXSS	L: Landsat	X: Sensor “M” (MSS), “T” (TM)	SS: Satellite “01” (Landsat 1), “03” (Landsat 3), “05” (Landsat 5)
LLLL	Processing correction level: “L1TP”, “L1GT”, “L1GS”, “L2SP”		
PPPRRR	PPP: WRS path		RRR: WRS row
YYYYMMDD	Acquisition year, month, day		
yyyymmdd	Processing year, month, day		
CC	Collection number: “01”, “02”, …		
TX	Collection category: “RT” (Real-Time), “T1” (Tier 1), “T2” (Tier 2)		

Source: usgs.gov/faqs/how-can-i-tell-difference-between-landsat-collections-data-and-landsat-data-i-have-downloaded (Accessed on 20-07-2020).

Data (Landsat MSS, Level-1)

Year	Image name	Product
1973	LM01_L1TP_148044_19730221_20200909_02_T2	River Shifting Change Detection Analysis
1980	LM03_L1TP_148044_19800221_20200905_02_T2	River Shifting Change Detection Analysis

Data (Landsat TM, Level-2)

Year	Image name	Product
1990	LT05_L2SP_138044_19900114_20200916_02_T1	River Shifting Change Detection Analysis
2000	LT05_L2SP_138044_20000211_20200907_02_T1	River Shifting Change Detection Analysis
2010	LT05_L2SP_138044_20100206_20200825_02_T1	River Shifting Change Detection Analysis

Sentinel-2 naming convention

Image name: MMM_MSIXXX_YYYYMMDDHHMMSS_Nxxyy_ROOO_Txxxxx_<Product Discriminator>

Group	Meaning
MMM	Mission ID: “S2A”, “S2B”
MSIXXX	Product level: “Level-1C”, “Level-2A”
YYYYMMDDTHHMMSS	Sensing start time, date and time separated by character “T”
Nxxyy	PDGS processing baseline number
ROOO	Relative orbit number
Txxxxx	Tile number

Source: sentinel.esa.int/web/sentinel/user-guides/sentinel-2-msi/naming-convention (Accessed on 20-07-2020).

Data

Year	Image name	Product
2019	S2A_MSIL2A_20190214T043901_N0211_R033_T45QYF_20190214T083011	River Shifting Change Detection Analysis
	S2B_MSIL2A_20191116T044039_N0213_R033_T45QYF_20191116T083209	Land-Use Classification

RADAR satellite images

Sentinel-1 naming convention

Image name: MMM_BB_TTTR_LFPP_YYYYMMDDTHHMMSS_ YYYYMMDDTHHMMSS_OOOOOO_DDDDDD_CCCC

Group	Meaning		
MMM	Mission Identifier: “S1A”, S1B”		
BB	Mode/Beam: “S1/S2/S3/S4/S5/S6”, “IW/EW/WV”		
TTTR	TTT: Product Type “RAW”, “SLC”, “GRD”, “OCN”	R: Resolution Class “F” (Full), “H” (High), “M” (Medium)	
LFPP	L: Processing Level “0”, “1”, “2”	F: Product Class “S” (Standard), “A” (Annotation)	PP: Polarization “SH” (single HH) “SV” (single VV) “DH” (dual HH+HV) “DV” (dual VV+VH)

YYYYMMDDTHHMMSS	Product start time, separated by the character “T”
YYYYMMDDTHHMMSS	Product end time, separated by the character “T”
OOOOOO	Absolute orbit number at product start time
DDDDDD	Mission data-take identifier
CCCC	Product unique identifier

Source: sentinel.esa.int/web/sentinel/user-guides/sentinel-1-sar/naming-conventions (Accessed on 20-07-2020).

Data: Inundation Mapping

Year	Image Name
2015	S1A_IW_GRDH_1SDV_20150612T235549_20150612T235623_006347_0085AA_49D7
	S1A_IW_GRDH_1SDV_20150706T235549_20150706T235614_006697_008F55_901C
2016	S1A_IW_GRDH_1SDV_20160606T235552_20160606T235617_011597_011B95_8496
	S1A_IW_GRDH_1SDV_20160630T235553_20160630T235618_011947_0126A4_97E1
	S1A_IW_GRDH_1SDV_20160724T235554_20160724T235619_012297_013213_9D2E
2017	S1A_IW_GRDH_1SDV_20170601T235553_20170601T235618_016847_01C031_BAE9
2018	S1A_IW_GRDH_1SDV_20180608T235600_20180608T235625_022272_026907_ECE2
	S1A_IW_GRDH_1SDV_20180714T235602_20180714T235627_022797_0278AA_BFC4
	S1A_IW_GRDH_1SDV_20180726T235603_20180726T235628_022972_027E33_0CE9
2019	S1A_IW_GRDH_1SDV_20190603T235606_20190603T235631_027522_031B0C_491A
	S1A_IW_GRDH_1SDV_20190615T235606_20190615T235631_027697_032055_31BB
	S1A_IW_GRDH_1SDV_20190627T235607_20190627T235632_027872_03258C_11CB

	S1A_IW_GRDH_1SDV_20190709T235608_20190709T235633_028047_032AE1_EBE3
	S1A_IW_GRDH_1SDV_20190721T235609_20190721T235634_028222_033027_D84D
2020	S1A_IW_GRDH_1SDV_20200609T235613_20200609T235638_032947_03D0F8_3E0C
	S1A_IW_GRDH_1SDV_20200621T235614_20200621T235639_033122_03D646_E3C7
	S1A_IW_GRDH_1SDV_20200703T235614_20200703T235639_033297_03DB97_BBB1
	S1A_IW_GRDH_1SDV_20200715T235615_20200715T235640_033472_03E0EC_97C8
	S1A_IW_GRDH_1SDV_20200727T235616_20200727T235641_033647_03E64C_C629
	S1B_IW_GRDH_1SDV_20200721T235548_20200721T235605_022576_02AD94_75A1

Data: Ground Motion Map

TerraSAR-X/TanDEM-X

TDX1_SAR__SSC_____SM_S_SRA_20191130T120939_20191130T120947
TSX1_SAR__SSC_____SM_S_SRA_20191124T235800_20191124T235808
TDX1_SAR__SSC_____SM_S_SRA_20191119T120939_20191119T120947
TDX1_SAR__SSC_____SM_S_SRA_20191108T120940_20191108T120948
TSX1_SAR__SSC_____SM_S_SRA_20191102T235800_20191102T235808
TDX1_SAR__SSC_____SM_S_SRA_20191028T120939_20191028T120947
TDX1_SAR__SSC_____SM_S_SRA_20191022T235800_20191022T235808
TDX1_SAR__SSC_____SM_S_SRA_20191017T120939_20191017T120947
TSX1_SAR__SSC_____SM_S_SRA_20191011T235800_20191011T235808
TDX1_SAR__SSC_____SM_S_SRA_20191006T120939_20191006T120947
TDX1_SAR__SSC_____SM_S_SRA_20190925T120939_20190925T120947
TDX1_SAR__SSC_____SM_S_SRA_20190919T235758_20190919T235806
TDX1_SAR__SSC_____SM_S_SRA_20190914T120938_20190914T120946
TSX1_SAR__SSC_____SM_S_SRA_20190429T235751_20190429T235800
TDX1_SAR__SSC_____SM_S_SRA_20190131T235749_20190131T235758
TDX1_SAR__SSC_____SM_S_SRA_20190413T120930_20190413T120938
TSX1_SAR__SSC_____SM_S_SRA_20190211T235749_20190211T235757
TDX1_SAR__SSC_____SM_S_SRA_20190120T235749_20190120T235758
TDX1_SAR__SSC_____SM_S_SRA_20190316T235749_20190316T235757
TSX1_SAR__SSC_____SM_S_SRA_20181207T235751_20181207T235800
TSX1_SAR__SSC_____SM_S_SRA_20190521T235752_20190521T235800
TDX1_SAR__SSC_____SM_S_SRA_20190402T120929_20190402T120937
TDX1_SAR__SSC_____SM_S_SRA_20190322T120929_20190322T120937
TDX1_SAR__SSC_____SM_S_SRA_20190217T120928_20190217T120937
TSX1_SAR__SSC_____SM_S_SRA_20190601T235752_20190601T235801
TDX1_SAR__SSC_____SM_S_SRA_20181224T120929_20181224T120938
TDX1_SAR__SSC_____SM_S_SRA_20190222T235748_20190222T235757
TDX1_SAR__SSC_____SM_S_SRA_20190206T120928_20190206T120936
TSX1_SAR__SSC_____SM_S_SRA_20190510T235752_20190510T235801
TSX1_SAR__SSC_____SM_S_SRA_20181218T235751_20181218T235759
TDX1_SAR__SSC_____SM_S_SRA_20181213T120930_20181213T120939
TDX1_SAR__SSC_____SM_S_SRA_20190104T120929_20190104T120937
TDX1_SAR__SSC_____SM_S_SRA_20190305T235749_20190305T235758
TDX1_SAR__SSC_____SM_S_SRA_20190607T120933_20190607T120941
TDX1_SAR__SSC_____SM_S_SRA_20190505T120931_20190505T120939
TDX1_SAR__SSC_____SM_S_SRA_20190311T120929_20190311T120937
TDX1_SAR__SSC_____SM_S_SRA_20190527T120931_20190527T120940
TDX1_SAR__SSC_____SM_S_SRA_20190228T120928_20190228T120936
TDX1_SAR__SSC_____SM_S_SRA_20190424T120930_20190424T120938

TSX1_SAR__SSC_____SM_S_SRA_20190327T235749_20190327T235758
TSX1_SAR__SSC_____SM_S_SRA_20190418T235750_20190418T235759
TDX1_SAR__SSC_____SM_S_SRA_20181229T235750_20181229T235759
TDX1_SAR__SSC_____SM_S_SRA_20190126T120928_20190126T120937
TDX1_SAR__SSC_____SM_S_SRA_20190115T120929_20190115T120937
TDX1_SAR__SSC_____SM_S_SRA_20190407T235750_20190407T235759
TDX1_SAR__SSC_____SM_S_SRA_20190516T120931_20190516T120939
TDX1_SAR__SSC_____SM_S_SRA_20190903T120938_20190903T120946
TDX1_SAR__SSC_____SM_S_SRA_20190828T235758_20190828T235806
TDX1_SAR__SSC_____SM_S_SRA_20190823T120937_20190823T120945
TSX1_SAR__SSC_____SM_S_SRA_20190817T235758_20190817T235806
TSX1_SAR__SSC_____SM_S_SRA_20190806T235757_20190806T235805
TSX1_SAR__SSC_____SM_S_SRA_20190801T120935_20190801T120943
TSX1_SAR__SSC_____SM_S_SRA_20190726T235756_20190726T235804
TSX1_SAR__SSC_____SM_S_SRA_20190721T120935_20190721T120943
TDX1_SAR__SSC_____SM_S_SRA_20190710T120934_20190710T120942
TDX1_SAR__SSC_____SM_S_SRA_20190704T235755_20190704T235803
TDX1_SAR__SSC_____SM_S_SRA_20190629T120934_20190629T120942
TSX1_SAR__SSC_____SM_S_SRA_20190623T235754_20190623T235802
TDX1_SAR__SSC_____SM_S_SRA_20190618T120933_20190618T120941
TSX1_SAR__SSC_____SM_S_SRA_20190612T235754_20190612T235802
TDX1_SAR__SSC_____SM_S_SRA_20180625T235746_20180625T235754
TSX1_SAR__SSC_____SM_S_SRA_20180603T235745_20180603T235753
TDX1_SAR__SSC_____SM_S_SRA_20180614T235746_20180614T235754
TDX1_SAR__SSC_____SM_S_SRA_20180620T120925_20180620T120933
TDX1_SAR__SSC_____SM_S_SRA_20180609T120925_20180609T120933
TDX1_SAR__SSC_____SM_S_SRA_20181121T120931_20181121T120939
TSX1_SAR__SSC_____SM_S_SRA_20181115T235752_20181115T235800
TDX1_SAR__SSC_____SM_S_SRA_20181110T120931_20181110T120939
TSX1_SAR__SSC_____SM_S_SRA_20181104T235752_20181104T235800
TDX1_SAR__SSC_____SM_S_SRA_20181030T120932_20181030T120940
TSX1_SAR__SSC_____SM_S_SRA_20181024T235752_20181024T235800
TDX1_SAR__SSC_____SM_S_SRA_20181019T120931_20181019T120939
TDX1_SAR__SSC_____SM_S_SRA_20181008T120931_20181008T120939
TSX1_SAR__SSC_____SM_S_SRA_20181002T235751_20181002T235759
TDX1_SAR__SSC_____SM_S_SRA_20180927T120930_20180927T120938
TSX1_SAR__SSC_____SM_S_SRA_20180921T235751_20180921T235759
TDX1_SAR__SSC_____SM_S_SRA_20180916T120930_20180916T120938
TDX1_SAR__SSC_____SM_S_SRA_20180910T235750_20180910T235758
TDX1_SAR__SSC_____SM_S_SRA_20180905T120930_20180905T120938
TSX1_SAR__SSC_____SM_S_SRA_20180830T235750_20180830T235758

TDX1_SAR__SSC_____SM_S_SRA_20180825T120929_20180825T120937
TDX1_SAR__SSC_____SM_S_SRA_20180819T235749_20180819T235757
TDX1_SAR__SSC_____SM_S_SRA_20180814T120928_20180814T120936
TDX1_SAR__SSC_____SM_S_SRA_20180808T235748_20180808T235756
TDX1_SAR__SSC_____SM_S_SRA_20180803T120928_20180803T120936
TSX1_SAR__SSC_____SM_S_SRA_20180728T235748_20180728T235756
TDX1_SAR__SSC_____SM_S_SRA_20180723T120927_20180723T120935
TDX1_SAR__SSC_____SM_S_SRA_20180717T235747_20180717T235755
TDX1_SAR__SSC_____SM_S_SRA_20180712T120927_20180712T120935
TDX1_SAR__SSC_____SM_S_SRA_20180706T235747_20180706T235755
TDX1_SAR__SSC_____SM_S_SRA_20180701T120926_20180701T120934
TDX1_SAR__SSC_____SM_S_SRA_20180529T120925_20180529T120933
TSX1_SAR__SSC_____SM_S_SRA_20180523T235746_20180523T235754
TDX1_SAR__SSC_____SM_S_SRA_20180518T120925_20180518T120933
TDX1_SAR__SSC_____SM_S_SRA_20180512T235745_20180512T235753
TDX1_SAR__SSC_____SM_S_SRA_20180507T120924_20180507T120932
TDX1_SAR__SSC_____SM_S_SRA_20180426T120924_20180426T120932
TSX1_SAR__SSC_____SM_S_SRA_20180420T235744_20180420T235752
TDX1_SAR__SSC_____SM_S_SRA_20180409T235743_20180409T235751
TDX1_SAR__SSC_____SM_S_SRA_20180404T120922_20180404T120930
TDX1_SAR__SSC_____SM_S_SRA_20180329T235743_20180329T235751
TDX1_SAR__SSC_____SM_S_SRA_20180324T120922_20180324T120930
TSX1_SAR__SSC_____SM_S_SRA_20180318T235743_20180318T235751
TDX1_SAR__SSC_____SM_S_SRA_20180313T120921_20180313T120929
TSX1_SAR__SSC_____SM_S_SRA_20180307T235742_20180307T235750
TDX1_SAR__SSC_____SM_S_SRA_20180302T120921_20180302T120929
TSX1_SAR__SSC_____SM_S_SRA_20180224T235742_20180224T235750
TDX1_SAR__SSC_____SM_S_SRA_20180219T120922_20180219T120930
TDX1_SAR__SSC_____SM_S_SRA_20180213T235742_20180213T235750
TDX1_SAR__SSC_____SM_S_SRA_20180208T120921_20180208T120929
TDX1_SAR__SSC_____SM_S_SRA_20180128T120921_20180128T120929
TDX1_SAR__SSC_____SM_S_SRA_20180122T235743_20180122T235751
TDX1_SAR__SSC_____SM_S_SRA_20180117T120922_20180117T120930
TSX1_SAR__SSC_____SM_S_SRA_20180111T235743_20180111T235751
TDX1_SAR__SSC_____SM_S_SRA_20180106T120922_20180106T120930
TDX1_SAR__SSC_____SM_S_SRA_20171231T235743_20171231T235751
TDX1_SAR__SSC_____SM_S_SRA_20171226T120923_20171226T120931
TSX1_SAR__SSC_____SM_S_SRA_20171220T235744_20171220T235752
TDX1_SAR__SSC_____SM_S_SRA_20171215T120923_20171215T120931
TDX1_SAR__SSC_____SM_S_SRA_20171209T235744_20171209T235752
TDX1_SAR__SSC_____SM_S_SRA_20171204T120924_20171204T120932

TSX1_SAR__SSC_____SM_S_SRA_20171128T235745_20171128T235753

Descending Sentinel-1 scenes for InSAR analyses

S1A_IW_SLC__1SDV_20170108T235553_20170108T235620_014747_018021_AF78
S1A_IW_SLC__1SDV_20170201T235553_20170201T235620_015097_018AE8_0CF1
S1A_IW_SLC__1SDV_20170225T235556_20170225T235624_015447_0195C3_438E
S1A_IW_SLC__1SDV_20170309T235556_20170309T235624_015622_019B0F_86B1
S1A_IW_SLC__1SDV_20170321T235549_20170321T235616_015797_01A044_AD43
S1A_IW_SLC__1SDV_20170402T235549_20170402T235616_015972_01A572_992C
S1A_IW_SLC__1SDV_20170414T235550_20170414T235617_016147_01AACB_13E9
S1A_IW_SLC__1SDV_20170426T235550_20170426T235617_016322_01B021_7E02
S1A_IW_SLC__1SDV_20170508T235551_20170508T235618_016497_01B575_76BA
S1A_IW_SLC__1SDV_20170520T235552_20170520T235619_016672_01BACE_6198
S1A_IW_SLC__1SDV_20170601T235552_20170601T235619_016847_01C031_6EC0
S1A_IW_SLC__1SDV_20170731T235556_20170731T235623_017722_01DAEC_BC55
S1A_IW_SLC__1SDV_20170812T235556_20170812T235624_017897_01E03B_C961
S1A_IW_SLC__1SDV_20170824T235557_20170824T235624_018072_01E586_6B60
S1A_IW_SLC__1SDV_20170905T235557_20170905T235625_018247_01EAD9_E6E0
S1A_IW_SLC__1SDV_20170917T235558_20170917T235625_018422_01F04D_E95C
S1A_IW_SLC__1SDV_20170929T235558_20170929T235625_018597_01F5A4_7C21
S1A_IW_SLC__1SDV_20171011T235558_20171011T235626_018772_01FAF6_3ACA
S1A_IW_SLC__1SDV_20171023T235559_20171023T235626_018947_020056_346F
S1A_IW_SLC__1SDV_20171104T235558_20171104T235626_019122_0205AC_472A
S1A_IW_SLC__1SDV_20171116T235558_20171116T235625_019297_020B23_DE86
S1A_IW_SLC__1SDV_20171128T235558_20171128T235625_019472_0210AA_99B1
S1A_IW_SLC__1SDV_20171210T235557_20171210T235625_019647_021620_6CF7
S1A_IW_SLC__1SDV_20171222T235557_20171222T235624_019822_021B82_B5BC
S1A_IW_SLC__1SDV_20180103T235556_20180103T235623_019997_022104_DB50
S1A_IW_SLC__1SDV_20180115T235556_20180115T235623_020172_022695_AA91
S1A_IW_SLC__1SDV_20180127T235556_20180127T235623_020347_022C20_FB07
S1A_IW_SLC__1SDV_20180208T235556_20180208T235623_020522_0231B8_3F2E
S1A_IW_SLC__1SDV_20180220T235555_20180220T235622_020697_023749_BCAD
S1A_IW_SLC__1SDV_20180304T235555_20180304T235622_020872_023CD2_4558
S1A_IW_SLC__1SDV_20180316T235555_20180316T235622_021047_024260_8DE5
S1A_IW_SLC__1SDV_20180328T235556_20180328T235623_021222_0247EE_905E
S1A_IW_SLC__1SDV_20180409T235556_20180409T235623_021397_024D6E_EF65
S1A_IW_SLC__1SDV_20180421T235556_20180421T235624_021572_0252DF_6606
S1A_IW_SLC__1SDV_20180503T235557_20180503T235624_021747_02585F_B3B1
S1A_IW_SLC__1SDV_20180515T235558_20180515T235625_021922_025DFC_9AD2
S1A_IW_SLC__1SDV_20180527T235558_20180527T235625_022097_02638A_95F7
S1A_IW_SLC__1SDV_20180608T235559_20180608T235626_022272_026907_10A3

S1A_IW_SLC__1SDV_20180714T235601_20180714T235628_022797_0278AA_12E8
S1A_IW_SLC__1SDV_20180726T235602_20180726T235629_022972_027E33_EC23
S1A_IW_SLC__1SDV_20180807T235603_20180807T235630_023147_0283AC_F0A5
S1A_IW_SLC__1SDV_20180819T235603_20180819T235630_023322_028959_796F
S1A_IW_SLC__1SDV_20180831T235604_20180831T235631_023497_028EE7_24DD
S1A_IW_SLC__1SDV_20180912T235604_20180912T235631_023672_02947F_0912
S1A_IW_SLC__1SDV_20180924T235605_20180924T235632_023847_029A32_0C6B
S1A_IW_SLC__1SDV_20181006T235605_20181006T235632_024022_029FEB_02A9
S1A_IW_SLC__1SDV_20181018T235605_20181018T235632_024197_02A59F_2825
S1A_IW_SLC__1SDV_20181030T235605_20181030T235632_024372_02AB43_2052
S1A_IW_SLC__1SDV_20181111T235605_20181111T235632_024547_02B19F_4583
S1A_IW_SLC__1SDV_20181123T235605_20181123T235632_024722_02B811_0A84
S1A_IW_SLC__1SDV_20181217T235604_20181217T235631_025072_02C446_FE20
S1A_IW_SLC__1SDV_20181229T235603_20181229T235630_025247_02CAA0_5DE8
S1A_IW_SLC__1SDV_20190110T235603_20190110T235630_025422_02D0E9_6482
S1A_IW_SLC__1SDV_20190122T235603_20190122T235630_025597_02D74F_CB2A
S1A_IW_SLC__1SDV_20190203T235602_20190203T235629_025772_02DDAA_BF65
S1A_IW_SLC__1SDV_20190215T235602_20190215T235629_025947_02E3DD_2230
S1A_IW_SLC__1SDV_20190227T235602_20190227T235629_026122_02EA16_344C
S1A_IW_SLC__1SDV_20190311T235602_20190311T235629_026297_02F071_A7C3
S1A_IW_SLC__1SDV_20190323T235602_20190323T235629_026472_02F6E8_C7A2
S1A_IW_SLC__1SDV_20190404T235602_20190404T235629_026647_02FD61_0D75
S1A_IW_SLC__1SDV_20190416T235603_20190416T235630_026822_0303BE_FD64
S1A_IW_SLC__1SDV_20190428T235603_20190428T235630_026997_030A0E_71B0
S1A_IW_SLC__1SDV_20190510T235603_20190510T235631_027172_031023_B369
S1A_IW_SLC__1SDV_20190522T235604_20190522T235631_027347_03159F_656C
S1A_IW_SLC__1SDV_20190603T235605_20190603T235632_027522_031B0C_0E08
S1A_IW_SLC__1SDV_20190615T235605_20190615T235632_027697_032055_B4A2
S1A_IW_SLC__1SDV_20190627T235606_20190627T235633_027872_03258C_E519
S1A_IW_SLC__1SDV_20190709T235607_20190709T235634_028047_032AE1_824D
S1A_IW_SLC__1SDV_20190721T235608_20190721T235635_028222_033027_8101
S1A_IW_SLC__1SDV_20190802T235608_20190802T235636_028397_03357D_725B
S1A_IW_SLC__1SDV_20190826T235610_20190826T235637_028747_03414E_9533
S1A_IW_SLC__1SDV_20190907T235610_20190907T235638_028922_034767_D1FF
S1A_IW_SLC__1SDV_20190919T235611_20190919T235638_029097_034D72_7397
S1A_IW_SLC__1SDV_20191001T235611_20191001T235639_029272_035378_8DF3
S1A_IW_SLC__1SDV_20191013T235611_20191013T235638_029447_03597F_D86F
S1A_IW_SLC__1SDV_20191025T235611_20191025T235638_029622_035F7E_4762
S1A_IW_SLC__1SDV_20191106T235611_20191106T235639_029797_0365AF_DDB9
S1A_IW_SLC__1SDV_20191118T235611_20191118T235638_029972_036BC0_69B0
S1A_IW_SLC__1SDV_20191130T235611_20191130T235638_030147_0371D0_0EE6

S1A_IW_SLC__1SDV_20191212T235610_20191212T235637_030322_0377DC_A727
S1A_IW_SLC__1SDV_20191224T235610_20191224T235637_030497_037DE8_42E1
S1B_IW_SLC__1SDV_20190504T235513_20190504T235543_016101_01E49E_CBB0
S1B_IW_SLC__1SDV_20190504T235541_20190504T235616_016101_01E49E_9D41

Ascending Sentinel-1 scenes for InSAR analyses

S1A_IW_SLC__1SDV_20170312T121208_20170312T121235_015659_019C2A_4D27
S1A_IW_SLC__1SDV_20170324T121208_20170324T121235_015834_01A15C_04A5
S1A_IW_SLC__1SDV_20170405T121208_20170405T121235_016009_01A68C_354D
S1A_IW_SLC__1SDV_20170417T121209_20170417T121236_016184_01ABEA_7AC2
S1A_IW_SLC__1SDV_20170429T121209_20170429T121236_016359_01B13B_4D85
S1A_IW_SLC__1SDV_20170511T121210_20170511T121237_016534_01B681_0928
S1A_IW_SLC__1SDV_20170523T121211_20170523T121237_016709_01BBEA_4DF9
S1A_IW_SLC__1SDV_20170604T121211_20170604T121238_016884_01C156_AFD4
S1A_IW_SLC__1SDV_20170628T121213_20170628T121240_017234_01CC09_5021
S1A_IW_SLC__1SDV_20170710T121213_20170710T121240_017409_01D151_765E
S1A_IW_SLC__1SDV_20170722T121214_20170722T121241_017584_01D6A4_5799
S1A_IW_SLC__1SDV_20170803T121215_20170803T121242_017759_01DBFC_B1EA
S1A_IW_SLC__1SDV_20170815T121215_20170815T121242_017934_01E151_84A1
S1A_IW_SLC__1SDV_20170827T121216_20170827T121243_018109_01E69C_86A5
S1A_IW_SLC__1SDV_20170908T121216_20170908T121243_018284_01EBF3_E267
S1A_IW_SLC__1SDV_20170920T121217_20170920T121244_018459_01F155_D0B8
S1A_IW_SLC__1SDV_20171002T121217_20171002T121244_018634_01F6B9_F075
S1A_IW_SLC__1SDV_20171014T121217_20171014T121244_018809_01FC09_A95D
S1A_IW_SLC__1SDV_20171026T121217_20171026T121244_018984_020158_116A
S1A_IW_SLC__1SDV_20171107T121217_20171107T121244_019159_0206C5_CB2D
S1A_IW_SLC__1SDV_20171119T121217_20171119T121244_019334_020C41_D545
S1A_IW_SLC__1SDV_20171201T121217_20171201T121244_019509_0211BA_24E9
S1A_IW_SLC__1SDV_20171213T121216_20171213T121243_019684_021735_8787
S1A_IW_SLC__1SDV_20171225T121216_20171225T121243_019859_021C9A_9C81
S1A_IW_SLC__1SDV_20180106T121215_20180106T121242_020034_022226_A3B7
S1A_IW_SLC__1SDV_20180118T121215_20180118T121242_020209_0227B2_D7A7
S1A_IW_SLC__1SDV_20180130T121214_20180130T121241_020384_022D42_1959
S1A_IW_SLC__1SDV_20180211T121214_20180211T121241_020559_0232D9_9BAB
S1A_IW_SLC__1SDV_20180223T121214_20180223T121241_020734_02386E_B22B
S1A_IW_SLC__1SDV_20180307T121214_20180307T121241_020909_023DF8_ADC9
S1A_IW_SLC__1SDV_20180319T121214_20180319T121241_021084_02437D_E5E4
S1A_IW_SLC__1SDV_20180331T121215_20180331T121241_021259_02490D_3055
S1A_IW_SLC__1SDV_20180412T121215_20180412T121242_021434_024E7E_A47E
S1A_IW_SLC__1SDV_20180424T121215_20180424T121242_021609_0253F3_5FF7
S1A_IW_SLC__1SDV_20180506T121216_20180506T121243_021784_02597F_8D35

S1A_IW_SLC__1SDV_20180518T121217_20180518T121244_021959_025F10_06D6
S1A_IW_SLC__1SDV_20180530T121217_20180530T121244_022134_0264B1_61B0
S1A_IW_SLC__1SDV_20180611T121218_20180611T121245_022309_026A26_A41D
S1A_IW_SLC__1SDV_20180623T121219_20180623T121246_022484_026F65_CBCA
S1A_IW_SLC__1SDV_20180705T121219_20180705T121246_022659_027482_1401
S1A_IW_SLC__1SDV_20180717T121220_20180717T121247_022834_0279D2_4F05
S1A_IW_SLC__1SDV_20180729T121221_20180729T121248_023009_027F5A_9EC0
S1A_IW_SLC__1SDV_20180810T121222_20180810T121249_023184_0284D5_FB2B
S1A_IW_SLC__1SDV_20180822T121222_20180822T121249_023359_028A7D_460E
S1A_IW_SLC__1SDV_20180903T121223_20180903T121250_023534_02900C_6F6A
S1A_IW_SLC__1SDV_20180915T121223_20180915T121250_023709_0295A8_49B0
S1A_IW_SLC__1SDV_20180927T121224_20180927T121251_023884_029B53_1AD8
S1A_IW_SLC__1SDV_20181009T121224_20181009T121251_024059_02A118_59D6
S1A_IW_SLC__1SDV_20181021T121224_20181021T121251_024234_02A6C9_AFF7
S1A_IW_SLC__1SDV_20181102T121224_20181102T121251_024409_02AC8E_469F
S1A_IW_SLC__1SDV_20181114T121224_20181114T121251_024584_02B2FA_413F
S1A_IW_SLC__1SDV_20181126T121223_20181126T121250_024759_02B969_51E8
S1A_IW_SLC__1SDV_20181208T121223_20181208T121250_024934_02BF41_0B42
S1A_IW_SLC__1SDV_20181220T121222_20181220T121249_025109_02C597_257E
S1A_IW_SLC__1SDV_20190101T121222_20190101T121249_025284_02CBEB_FED6
S1A_IW_SLC__1SDV_20190113T121222_20190113T121249_025459_02D234_8C26
S1A_IW_SLC__1SDV_20190125T121221_20190125T121248_025634_02D899_CFD2
S1A_IW_SLC__1SDV_20190206T121221_20190206T121247_025809_02DEE0_63AD
S1A_IW_SLC__1SDV_20190218T121221_20190218T121248_025984_02E51F_CD73
S1A_IW_SLC__1SDV_20190302T121221_20190302T121248_026159_02EB68_F0AE
S1A_IW_SLC__1SDV_20190314T121221_20190314T121248_026334_02F1CB_A040
S1A_IW_SLC__1SDV_20190326T121221_20190326T121248_026509_02F838_26C9
S1A_IW_SLC__1SDV_20190407T121221_20190407T121248_026684_02FEAD_31D1
S1A_IW_SLC__1SDV_20190419T121222_20190419T121248_026859_030507_7457
S1A_IW_SLC__1SDV_20190501T121222_20190501T121249_027034_030B64_9F80
S1A_IW_SLC__1SDV_20190513T121223_20190513T121249_027209_031140_DFAD
S1A_IW_SLC__1SDV_20190606T121224_20190606T121251_027559_031C1F_C7AB
S1A_IW_SLC__1SDV_20190618T121224_20190618T121251_027734_032165_A947
S1A_IW_SLC__1SDV_20190630T121225_20190630T121252_027909_03269F_7503
S1A_IW_SLC__1SDV_20190712T121226_20190712T121253_028084_032BED_91DA
S1A_IW_SLC__1SDV_20190724T121227_20190724T121254_028259_033136_2EFE
S1A_IW_SLC__1SDV_20190805T121228_20190805T121254_028434_033690_415A
S1A_IW_SLC__1SDV_20190817T121228_20190817T121255_028609_033C79_629B
S1A_IW_SLC__1SDV_20190829T121229_20190829T121256_028784_03429E_E3A7
S1A_IW_SLC__1SDV_20190910T121229_20190910T121256_028959_0348B6_EC06
S1A_IW_SLC__1SDV_20190922T121230_20190922T121257_029134_034EAB_7873

S1A_IW_SLC__1SDV_20191004T121230_20191004T121257_029309_0354B0_3BF0
S1A_IW_SLC__1SDV_20191016T121230_20191016T121257_029484_035ABB_8AF7
S1A_IW_SLC__1SDV_20191028T121230_20191028T121257_029659_0360C3_75BB
S1A_IW_SLC__1SDV_20191109T121230_20191109T121257_029834_0366F3_D352
S1A_IW_SLC__1SDV_20191121T121230_20191121T121257_030009_036CFD_CD2A
S1A_IW_SLC__1SDV_20191203T121229_20191203T121256_030184_03730F_796E
S1A_IW_SLC__1SDV_20191215T121229_20191215T121256_030359_03791A_31E0
S1A_IW_SLC__1SDV_20191227T121229_20191227T121256_030534_037F23_E3CD
S1B_IW_SLC__1SDV_20190507T121145_20190507T121213_016138_01E5D1_D8ED

Annexure D: SARscape processing parameters

SBAS processing parameters from parameters.sml file generated by ENVI SARscape:

**Parameter settings used for the process **

Min Normal Baseline is 0.000000 ** Max Normal Baseline is 2.000000 ** Min Temporal Baseline is 0 ** Max Temporal Baseline is 90 ** Redundancy is low ** Criteria is min_temporal ** Min number of link per image is 10 ** Only Forward Pairs is FALSE ** Allow Disconnected Blocks is TRUE ** Delaunay 3D is FALSE

Initialization From Orbit is TRUE ** Estimate From Amplitude is TRUE ** Estimate From Coherence is TRUE ** Range Looks is 4 ** Azimuth Looks is 1 ** Range Dependency is 3 ** Azimuth Dependency is 3 ** Range Res Dependency is 2 ** Azimuth Res Dependency is 1 ** Range Window Number is 12 ** Azimuth Window Number is 3 ** Range Window Size is 256 ** Azimuth Window Size is 128 ** Cross Correlation Threshold is 0.250000 ** Fine Range Window Number is 25 ** Fine Azimuth Window Number is 8 ** Fine Range Window Size is 32 ** Fine Azimuth Window Size is 32 ** SNR Threshold is 3.200000 ** Coregistration with DEM is TRUE

Spectral Shift Filter is TRUE ** Doppler Filter is FALSE ** Range Looks is 4 ** Azimuth Looks is 1

Orbit Interpolation is 100 ** Optimal Resolution Approach is TRUE ** Window Size Mean Filter size is 5 ** Window Size Interpolation is 11 ** DEM Resampling Factor is -1.000000

Goldstein filter ** Interferogram Window Size is 64 ** Window Overlap Percentage is 80.000000 ** Low Pass Percentage is 5.000000 ** Intensity Window Size is 5 ** Alpha Min Value is 0.300000 ** Alpha Max Value is 2.500000 ** Coherence from Fint is TRUE ** Coherence Rg Window Size is 5 ** Coherence Az Window Size is 5 ** Low Frequency Removal Rg is 0 ** Low Frequency Removal Az is 0

EMPTY

Unwrapping Method is MCF_DELAUNAY ** Unwrapping Coherence Threshold is 0.300000 ** Decomposition Levels is 1 ** Range Scale Factor Decomposition is 3 ** Azimuth Scale Factor Decomposition is 3 ** Use 3D Unwrapping FALSE ** 3D Velocity Step Nr is 200 ** 3D Height Step Nr is 200 ** 3D Velocity Step Size is 5.000000 ** 3D Height Step Size is 10.000000 ** 3D Interferogram Valid Percentage is 60.000000 ** Tile Size in Range is 800 ** Tile Size in Azimuth is 800 ** Range Overlap is 300 ** Azimuth Overlap is 200 ** Minimum Cost Coherence is -1.000000

Refinement Method is RemoveResidualPhase ** Residual Phase Poly Degree is 3

Estimate residual height is OK ** Displacement model type is linear ** Weighted Solution is TRUE ** Inversion SVD type is jacobi ** Min Valid Interf Percentage is 50.000000% ** Interpolate Disconnected Blocks is allow ** Reject outliars H [m] is -1.000000 ** Reject outliars D [mm] is -1.000000 ** Coherence Threshold is 0.300000 ** Wavelet LP size is 1200.000000

Unwrapping Method is MCF_DELAUNAY ** Unwrapping Coherence Threshold is 0.300000 ** Decomposition Levels is 1 ** Range Scale Factor Decomposition is 3 ** Azimuth Scale Factor Decomposition is 3 ** Use 3D Unwrapping FALSE ** 3D Velocity Step Nr is 200 ** 3D Height Step Nr is 200 ** 3D Velocity Step Size is 5.000000 ** 3D Height Step Size is 10.000000 ** 3D Interferogram Valid Percentage is 60.000000 ** Tile Size in Range is 800 ** Tile Size in Azimuth is 800 ** Range Overlap is 300 ** Azimuth Overlap is 200 ** Minimum Cost Coherence is -1.000000

Refinement Method is RemoveResidualPhase ** Residual Phase Poly Degree is 3

Refinement poly degree is 3 ** Estimate residual height first is OK ** Displacement model type first is linear ** Displacement model type second is same_as_first ** Weighted Solution is TRUE ** Inversion SVD type is jacobi ** Min Valid Interf Percentage is 50.000000% ** Interpolate Disconnected Blocks is interpol_using_model ** Min Valid Image Percentage is 70.000000% ** Reject outliars H [m] is -1.000000 ** Reject outliars D [mm] is -1.000000 ** Reject min number of interf per image is 3 ** Redundancy min number of interf per image is 5 ** Coherence Threshold is 0.300000

Refinement poly degree is 3 ** Skip Atmosphere estimation is FALSE ** Atmosphere Low Pass Size is 1600.000000 ** Atmosphere High Pass Size is 365.000000

X Dimension is 15.000000 ** Y Dimension is 15.000000 ** Precision Height threshold is 10.000000 ** Precision Velocity threshold is 8.000000 ** Temporal coherence threshold is 0.100000 ** Water body mask threshold [dB] is 0.000000 ** Generate results in raster format is TRUE ** Generate results in shape format is TRUE ** Add time series in shape is TRUE ** Max number of points in shape is 200000 ** Interpolation Window Size is 3 ** Mean Window Size is 3 ** Generate Vertical Direction Results is FALSE ** Generate Max Slope Direction Results is FALSE ** Max Slope Direction Files is NotOK ** Generate User Direction Results is FALSE ** Azimuth Angle is 0.000000 ** Inclination Angle is 0.000000

Sentinel-1 PSI processing parameters from parameters.sml file generated by ENVI SARscape:

**This Tool Implemet the PS Module ** First Version 10.02.2011 AC ** Copyright by Sarmap SA ** Based on F.Rocca, A.Ferretti ** A New Algorithm for Surface Deformation Monitoring Based on persistent scatterers **

Initialization From Orbit is TRUE ** Orbit Accuracy is TRUE ** Estimate From Amplitude is TRUE ** Estimate From Coherence is TRUE ** Range Dependency is 3 ** Azimuth Dependency is 3 ** Range Window Number is 12 ** Azimuth Window Number is 3 ** Range Window Size is 256 ** Azimuth Window Size is 128 ** Cross Correlation Threshold is 0.250000 ** Fine Range Window Number is 25 ** Fine Azimuth Window Number is 8 ** Fine Range Window Size is 32 ** Fine Azimuth Window Size is 32 ** SNR Threshold is 3.200000

Range Looks is -2 ** Azimuth Looks is 1 ** pectral Shift Filter is FALSE ** Doppler Filter is FALSE

Sub-Area size(sqkm) is 25.000000 ** Overlap(%) is 30 ** Coherence used for Merging all Sub-Areas is 0.660000 ** min velocity[mm/year] is -100.000000 ** max velocity[mm/year] is 100.000000 ** sampling rate velocity[mm/year] is 1.000000 ** min height[m] is -70.000000 ** max height[m] is 70.000000 ** sampling rate height[m] is 2.000000

Low Pass Filter Size[m] is 1200.000000 ** High Pass Filter Size[days] is 365.000000 ** min velocity[mm/year] is -100.000000 ** max velocity[mm/year] is 100.000000 ** sampling rate velocity[mm/year] is 1.000000 ** min height[m] is -70.000000 ** max height[m] is 70.000000 ** sampling rate height[m] is 2.000000

Coherence Threshold is 0.700000 ** Geocode using Mu/Sigma Threshold is FALSE ** Mu/Sigma Threshold is 0.000000 ** Water Body Mask Threshold Is 0.000000 ** Refinement GCP File Is NotOK ** Geocoded Shape Products is TRUE ** Geocoded Raster Products is TRUE ** X Dimension is 15.000000 ** Y Dimension is 15.000000

TerraSAR-X PSI processing parameters from parameters.sml file generated by ENVI SARscape:

**This Tool Implemet the PS Module ** First Version 10.02.2011 AC ** Copyright by Sarmap SA ** Based on F.Rocca, A.Ferretti ** A New Algorithm for Surface Deformation Monitoring Based on persistent scatterers **

Initialization From Orbit is TRUE ** Orbit Accuracy is TRUE ** Estimate From Amplitude is TRUE ** Estimate From Coherence is TRUE ** Range Dependency is 3 ** Azimuth Dependency is 3 ** Range Window Number is 10 ** Azimuth Window Number is 10 ** Range Window Size is 256 ** Azimuth Window Size is

256 ** Cross Correlation Threshold is 0.250000 ** Fine Range Window Number is 50 ** Fine Azimuth Window Number is 50 ** Fine Range Window Size is 32 ** Fine Azimuth Window Size is 32 ** SNR Threshold is 3.200000

Range Looks is -4 ** Azimuth Looks is 1 ** pectral Shift Filter is FALSE ** Doppler Filter is FALSE

Sub-Area size(sqkm) is 25.000000 ** Overlap(%) is 30 ** Coherence used for Merging all Sub-Areas is 0.660000 ** min velocity[mm/year] is -25.000000 ** max velocity[mm/year] is 25.000000 ** sampling rate velocity[mm/year] is 1.000000 ** min height[m] is -70.000000 ** max height[m] is 70.000000 ** sampling rate height[m] is 2.000000

Low Pass Filter Size[m] is 1200.000000 ** High Pass Filter Size[days] is 365.000000 ** min velocity[mm/year] is -25.000000 ** max velocity[mm/year] is 25.000000 ** sampling rate velocity[mm/year] is 1.000000 ** min height[m] is -70.000000 ** max height[m] is 70.000000 ** sampling rate height[m] is 2.000000

Coherence Threshold is 0.600000 ** Geocode using Mu/Sigma Threshold is FALSE ** Mu/Sigma Threshold is 0.000000 ** Water Body Mask is 0.000000 ** Refinement GCP File Is NotOK ** Geocoded Shape Products is TRUE ** Geocoded Raster Products is TRUE ** X Dimension is 1.500000 ** Y Dimension is 1.500000